On the thermophysical and structural properties of the $Au_{49}Cu_{26.9}Si_{16.3}Ag_{5.5}Pd_{2.3}$ bulk metallic glass-forming alloy and their connection to the liquid-liquid transition in the deeply supercooled liquid

Dissertation

zur Erlangung des Grades
des Doktors der Ingenieurswissenschaften
der Naturwissenschaftlich-Technischen Fakultät
der Universität des Saarlandes

von
Simon Hechler

Saarbrücken
2018

Tag des Kolloquiums: 14.11.2018

Dekan: Prof. Dr. rer. nat. Guido Kickelbick

Berichterstatter: Prof. Dr. rer. nat. Ralf Busch

Prof. Dr. mont. Christian Motz

Vorsitz: Prof. Dr. rer. nat. Wulff Possart

Akad. Mitarbeiter: Dr. Ing. Dr. rer. nat. Anne Jung

Danksagung

Zu aller erst möchte ich meinem Betreuer Prof. Dr. Ralf Busch danken. Sein Vertrauen und seine Unterstützung haben diese Promotion überhaupt erst möglich gemacht. Seine Aufgeschlossenheit lässt jedem die Möglichkeit Neues auszuprobieren. Ich möchte Dr. Isabella Gallino für ihre Unterstützung, ihren Rat und die vielen Diskussionen während meiner Doktorandenzeit danken. Außerdem dem gilt mein Dank Dr. Beatrice Ruta für Ihre Unterstützung während meines Forschungsaufenthaltes an der European Synchrotron Radiation Facility (ESRF) in Grenoble. Ich möchte dem gesamten Team der ID10 der ESRF für die spannende Zeit und die Unterstützung danken: Oleg, Bea, Federico, Yurij, Giovanni, Karim and Jens. Jaco, vielen Dank für das Savoire-vivre. Unsere gemeinsamen Aktivitäten haben die vier Monate in Grenoble zu einem besonderen Erlebnis gemacht. Ralf, Isabella, Moritz, Sigrid, Herr Dr. Aubertin, Zach, Sanja, Will, Shuai, Nico, Max, Hermann, Jörg, Martina, Lisa und alle Hiwis, vielen Dank für die tolle Zeit am Lehrstuhl für Metallische Werkstoffe. Aus dieser Gruppe möchte ich das Dreamteam Alex, Bob und Oli hervorheben. Ohne eure Unterstützung und die Atmosphäre, die ihr am LMW geschaffen habt, wäre ich sicherlich mit mehr grauen Haaren am Ende der Promotion angekommen.

Es gibt viele Menschen aus meinem privaten Umfeld, denen ich gerne danken möchte. Im Besonderen möchte ich mich bei meinen Eltern und meinen Geschwistern bedanken. Ohne eure Liebe und eure Unterstützung wäre mein Weg zur Promotion nicht möglich gewesen. Ich möchte meinen Freunden danken, die immer ein offenes Ohr für mich haben und an so manchem Abend für die notwendige Zerstreuung gesorgt haben.

Ich möchte meiner Familie danken. Anke, ich danke dir für dein Verständnis und deine Unterstützung besonders in den Momenten, in denen ich dich am meisten gebraucht habe. Ich danke dir für unseren Johann, der uns gezeigt hat worauf es im Leben ankommt. Ich liebe euch.

Acknowledgements

First of all, I would like to thank my supervisor Prof. Dr. Ralf Busch. His guidance and support during my time as Phd student made this thesis possible in the first place. His openness gives everbody the possibility to pursue new ideas. I would like to thank Dr. Isabella Gallino for her support and the many, many discussions we had during my Phd life. I would particularly like to thank Dr. Beatrice Ruta, who supervised me during my time at the European Synchrotron Radiation Facility (ESRF) and afterwards. I would like to thank the entire team of ID10 (Oleg, Bea, Federico, Yurij, Giovanni, Karim and Jens) for the great time at the ESRF and the support. Jaco, thanks for the great time. Our activities made the time in Grenoble an unique experience.

Ralf, Isabella, Moritz, Sigrid, Herr Dr. Aubertin, Zach, Sanja, Will, Shuai, Nico, Max, Hermann, Jörg, Martina, Lisa and all Hiwis, thank you for the great time at the Lehrstuhl für Metallische Werkstoffe (LMW). From the LMW crew, I would like to thank particularly the dream team Alex, Bob and Oli. Thanks to your support and the working atmosphere that you created at the LMW, I reached the end of my Phd with only a few grey hairs.

Apart from my professional companions, I would like to thank some people from my social environment. At first, I would like to thank my parents and siblings. Without your love and support I would not have been able to go the long way to the doctoral thesis. I would like to thank my friend for their time when I need somebody to talk about what bothers me.

Last but not least, I would like to thank my family. Anke, I thank you for your love and support throughout the last years, especially in the moments when I needed it the most. I would like to thank you for our Johann, who showed us what is important in life. I love you.

Abstract

Liquid-liquid transitions (LLTs) between two liquid phases with different structures but identical compositions have been found in all types of liquids. In this work a liquid-liquid transition in the $Au_{49}Cu_{26.9}Si_{16.3}Ag_{5.5}Pd_{2.3}$ bulk metallic glass-forming alloy is revealed using a quasi-static cooling protocol in the ultra-viscous state. The slow cooling lowers the glass transition of the liquid which at standard cooling rates obscures the LLT. The LLT shows a structural, dynamical and thermodynamic signature. The structure is investigated in situ using high energy synchrotron x-ray diffraction (XRD). The dynamical cross-over from a highly temperature dependent liquid to a liquid which is less affected by temperature is observed in situ by x-ray photon correlation spectroscopy (XPCS) and ex situ through laboratory-based techniques like dynamical mechanical analysis (DMA), thermomechanical analysis (TMA) and differential scanning calorimetry (DSC). The thermodynamic signature is measured ex situ using DSC.

Zusammenfassung

Phasenübergänge in der Flüssigkeit zwischen zwei flüssigen Phasen mit unterschiedlicher Struktur aber identischer chemischer Zusammensetzung wurden in vielen verschiedenen Flüssigkeiten nachgewiesen. In dieser wissenschaftlichen Arbeit wurde ein Flüssig-Flüssig-Phasenübergang in der hochviskosen unterkühlten Schmelze der metallisches massivglasformenden Legierung $Au_{49}Cu_{26.9}Si_{16.3}Ag_{5.5}Pd_{2.3}$ mit Hilfe eines quasistatischen Kühlprotokolls entdeckt. Das quasistatische Kühlen verschiebt den Glasübergang, der den Flüssig-Flüssig-Phasenübergang bei höheren Raten verdeckt, zu niedrigeren Temperaturen und ermöglicht so die Beobachtung des Phasenüberganges. Der Übergang zeigt Signaturen in der Struktur, der Dynamik und der Thermodynamik. Die Struktur wurde durch Röntgenbeugungsexperimente mit Hilfe hochenergetischer Synchrotronröntgenstrahlung untersucht. Die dynamische Signatur des Übergangs wurde in situ mittels synchrotronbasierter Röntgenkorrelationsspektroskopie und ex situ mittels verschiedener laborbasierter Techniken wie dynamisch mechanischer Analyse (DMA), thermo-mechanischer Analyse (TMA) und Kalorimetrie (DSC) nachgewiesen. Die thermodynamische Signatur wurde mittels DSC untersucht.

Oral presentations and posters

- 13.07.15-17.07.2015 22nd International Symposium on Metastable, Amorphous and Nanostructured Materials (ISMANAM), Paris, France, **poster contribution**: “Comparative thermodynamic and kinetics study between bulk metallic and flint glasses”
- 13.07.15-17.07.2015 22nd International Symposium on Metastable, Amorphous and Nanostructured Materials, Paris, France, **poster contribution**: “Distinct Dynamical Regimes in a Gold-Based Metallic Glass revealed by X-ray photon correlation spectroscopy (XPCS)”
- 08.-10.02.2016 ESRF Usermeeting 2016, Grenoble, France, **oral presentation**: “Distinct Dynamical Regimes in a Gold-based Metallic Glass”
- 06.-11.03.2016 DPG Tagung 2016, Regensburg, Germany, **oral presentation**: “Distinct Dynamical Regimes in a Gold-based Metallic Glass”
- 04.09.2017-09.09.2017 16th International Conference on Liquid and Amorphous Metals (LAM), Bad Godesberg, Germany, **oral presentation**: “Signature of a Liquid-Liquid Transition in a Gold-Based Metallic Glass”
- 19.-24.03.2017 DPG Tagung 2017, Dresden, Germany, **oral presentation**: “Signature of the atomic structure in the thermophysical properties of flint and metallic glasses”.
- 27.08.-01.09.2017 16th International Conference on Rapidly Quenched and Metastable Materials (RQ16), Leoben, Austria, **oral presentation**: “Microscopic evidence of a liquid-liquid transition below the conventional glass transition temperature”
- 27.08.-01.09.2017 16th International Conference on Rapidly Quenched and Metastable Materials (RQ16), Leoben, Austria, **poster contribution**: “Relation between structure, thermodynamics and kinetics in bulk metallic and flint glasses”

Publications

First Author:

- **S. Hechler**, B. Ruta, M. Stolpe, E. Pineda, Z. Evenson, O. Gross, W. Hembree, Liquid-liquid transition revealed by quasi-static cooling of an ultra-viscous metallic liquid, ArXiv. 1704.06703 (2017) 1704.06703.

or

- **S. Hechler**, B. Ruta, M. Stolpe, E. Pineda, Z. Evenson, O. Gross, A. Bernasconi, R. Busch, I. Gallino, Microscopic evidence of the connection between liquid-liquid transition and dynamical crossover in an ultra-viscous metallic glass former, submitted to Phys. Rev. Lett. (2018).
- **S. Hechler**, B. Ruta, M. Stolpe, D. Orsi, L. Cristofolini, Z. Evenson, R. Busch, I. Gallino, Influence of the structure and dynamical heterogeneities on the relaxation dynamics in an ultra-viscous glass-former, submitted to Phys. Rev. Lett. (2018)
- **S. Hechler**, I. Gallino, M. Stolpe, F.-T. Lentes, R. Busch, Analysis of thermophysical properties of lead silicates in comparison to bulk metallic glasses, J. Non. Cryst. Solids. 485 (2018) 66–73. doi:10.1016/j.jnoncrysol.2018.01.041.

Co-Author:

- Z. Evenson, B. Ruta, **S. Hechler**, M. Stolpe, E. Pineda, I. Gallino, R. Busch, X-Ray Photon Correlation Spectroscopy Reveals Intermittent Aging Dynamics in a Metallic Glass, Phys. Rev. Lett. 115 (2015) 175701. doi:10.1103/PhysRevLett.115.175701.

- S. Wei, M. Stolpe, O. Gross, W. Hembree, **S. Hechler**, J. Bednarcik, R. Busch, P. Lucas, Structural evolution on medium-range-order during the fragile-strong transition in $Ge_{15}Te_{85}$, Acta Mater. 129 (2017) 259–267. doi:10.1016/j.actamat.2017.02.055.

- O. Gross, B. Bochtler, M. Stolpe, **S. Hechler**, W. Hembree, R. Busch, I. Gallino, The kinetic fragility of Pt-P- and Ni-P-based bulk glass forming liquids and its thermodynamic and structural signature, Acta Mater. 132 (2017) 118–127. doi:10.1016/j.actamat.2017.04.030.

- O. Gross, S.S. Riegler, M. Stolpe, B. Bochtler, A. Kuball, **S. Hechler**, R. Busch, I. Gallino, On the high glass-forming ability of Pt-Cu-Ni/Co-P-based liquids, Acta Mater. 141 (2017) 109–119. doi:10.1016/j.actamat.2017.09.013.

- Gallino, D. Cangialosi, Z. Evenson, L. Schmitt, **S. Hechler**, M. Stolpe, B. Ruta, Hierarchical aging pathways and reversible fragile-to-strong transition upon annealing of a metallic glass former, Acta Mater. 144 (2018) 400–410. doi:10.1016/j.actamat.2017.10.060.

Contents

1 Introduction

The investigation of glasses concerning thermodynamics, kinetics and structure is indivisibly connected to the properties of the corresponding liquid as the glass possesses the structure of the liquid at the temperature where it was frozen-in [1]. Therefore, the liquid is the key to understand the thermodynamic and kinetic behavior and as well as the structure of a glass. Unfortunately, the investigation of the liquid state is challenging as no long-range order exists, which facilitate the investigation of crystalline materials. But the atomic interaction is still decisive for a correct description of the liquid in contrast to gases. For this reason, the structure and its relation to thermodynamic and kinetic properties in liquids is still an unsolved problem [1].

To shed light upon thermodynamics, kinetics and structure of liquids, sophisticated experimental techniques, like the experimental setups installed at 3rd generation synchrotrons, are necessary. The high intensity X-ray diffraction (XRD) setups which are available e.g. at the European Synchrotron Radiation Facility (ESRF) and the Deutsches Elektronensynchrotron (DESY) allow the observation of tiny changes in the still unknown structure of liquids. For the investigation of the atomic dynamics of glasses and liquids a new technique has been developed within the last two decades. X-ray photon correlation spectroscopy (XPCS) is a synchrotron-based technique and allows the measurements of the dynamics of glasses and liquids in the vicinity of the glass transition with partially coherent x-rays.

A liquid can exist in different configurations as a function of temperature or pressure without changes in the composition. This phenomenon is called polyamorphism. The transition from one configuration to another one is called liquid-liquid transition (LLT). LLTs have been found in a broad spectrum of liquids [2–6] suggesting it to be a general phenomenon.

XPCS, XRD and further laboratory-based methods have been used to investigate the structure, kinetics and thermodynamics of the $Au_{49}Cu_{26.9}Si_{16.3}Ag_{5.5}Pd_{2.3}$ (at%)

gold based metallic glass and its liquid. The investigated alloy shows a LLT below the conventional glass transition, which has never been observed before in a metallic glass but is suggested based on general considerations [7].

2 State of the Art

2.1 Bulk Metallic Glasses

2.1.1 History and perspective

Metallic glasses, which are also called amorphous metals, were discovered in 1960 [8]. Duwez et al. cast a thin film of an Au-Si alloy, which did not crystallize during the processing and exhibited an amorphous structure. Before, only vapor deposited amorphous layers have been built [9]. After this initial ignition, researchers started to develop new metallic glass-forming alloys. Due to the better understanding of the glass formation in metallic systems, the critical casting thickness has continuously been improved. The early binary alloys like the Au-Si system required critical cooling rate of 10^6 K s^{-1} resulting in critical casting thicknesses in the range of micrometers [10], whereas the multicomponent alloys reach thicknesses in the range of centimeters, which requires cooling rates of only 1 K s^{-1} [11]. Since 1990, metallic glasses with critical casting thicknesses of more than 1 mm, so called bulk metallic glasses (BMG), can be produced. The best glass formers are beryllium containing alloys. But due to the toxicity of beryllium, especially during the processing, they are not usable for industrial and medical applications. Since the last decade the alloy development has been focused on beryllium-free alloys containing cheap industrial grade raw elements. Among these beryllium-free alloys is an alloy with a critical casting thickness of more than 1 cm that has been developed by the chair of metallic materials at Saarland University in 2012. This alloy could become a trailblazer for metallic glasses as structural material as it has been licensed for industrial usage [Patent: 1. *Bulk metallic glass forming alloy* J. Heinrich, R. Busch, EP 2 597 166 B1, accepted: 15.10.2014].

The development of new alloys is just one step to get metallic glasses into application using their unique mechanical properties (see section 2.1.2). Another step is the development of new processing techniques allowing the production of large numbers of parts to be competitive in comparison to conventional materials. Besides casting techniques, additive manufacturing like selective laser melting has emerged in the last years, which is ideal for the processing of metallic glasses. The selective laser melting process possesses intrinsically high cooling rates of 10^3-10^5 K s^{-1}, which allow the fabrication of metallic glasses from powder wrought material.

The combination of cheap alloys and new processing techniques could be the decisive factor to get amorphous metals into industrial application, what has early been impeded by too high raw material costs and expensive manufacturing.

2.1.2 Properties and Applications

Bulk metallic glasses (BMG) have a very unique combination of properties due to the missing crystalline structure. They exhibit an elastic limit of about 2% like polymers in combination with a yield strength of more than 3 GPa, e.g. [11–13], which is 3 times higher than the yield strength of steels (see Figure 2-1).

They reach almost their theoretical strength which is the stress needed to overcome the atomic bonding force (see Figure 2-2), due to the different deformation mechanism in BMGs in comparison to crystalline metals. In crystalline metals plastic deformation is performed by dislocations, which are generated and move at stresses which are significantly smaller than the theoretical strength of the material. This deformation mechanism is missing in BMGs. The high yield strength together with the high elastic limit makes BMGs interesting candidates as structural material. The high hardness of BMGs is advantageous for applications where wear resistance is needed. Due to the mechanical properties and the size restrictions BMGs are an ideal material for small high strength parts in aviation industry, medical engineering and mechanical engineering. Beside the unique mechanical properties, magnetic Fe-, Ni-, Co-based BMGs exhibit very good soft magnetic properties as no grain boundaries exist where magnetic domains can be pinned at. For this reason, magnetic BMGs can follow changes in the magnetization direction easily which is the key property defining a good soft magnet. Typical applications for soft magnetic BMGs are transformer cores, magnetic strips in theft protection systems and current metering sensors.

Looking at the casting process, BMGs have another very advantageous property. Due to the missing crystallization, the volume shrinkage of 2-5% during crystallization does not occur, what makes near net-shape production possible. Finest contours in a die casting mold are filled and no holding pressure is needed during the casting process.

The $Au_{49}Cu_{26.9}Si_{16.3}Ag_{5.5}Pd_{2.3}$ alloy, which is investigated in this thesis is promising for jewelry application due to its interesting color and high hardness in comparison to conventional crystalline gold-based alloys. The properties are described more detailed in section 3.1.1.

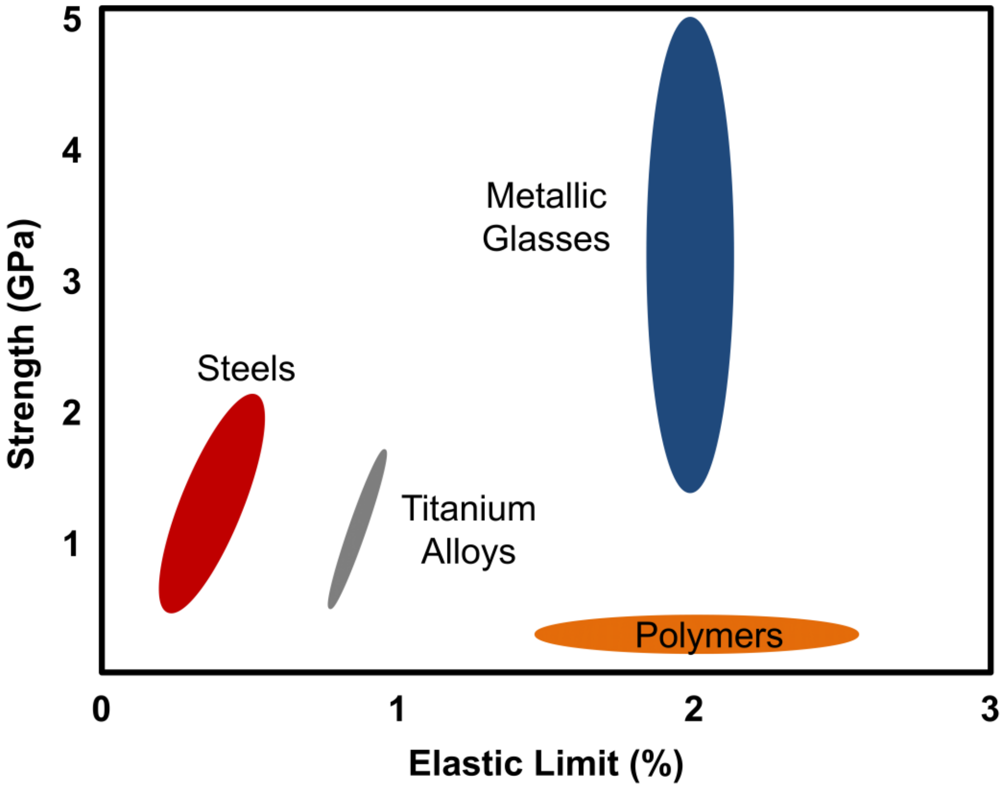

Figure 2-1: Comparison of strength and elastic limit for several classes of materials after Telford [11]. Metallic glasses (blue) exhibit the highest strength in combination with an elastic limit comparable to polymers.

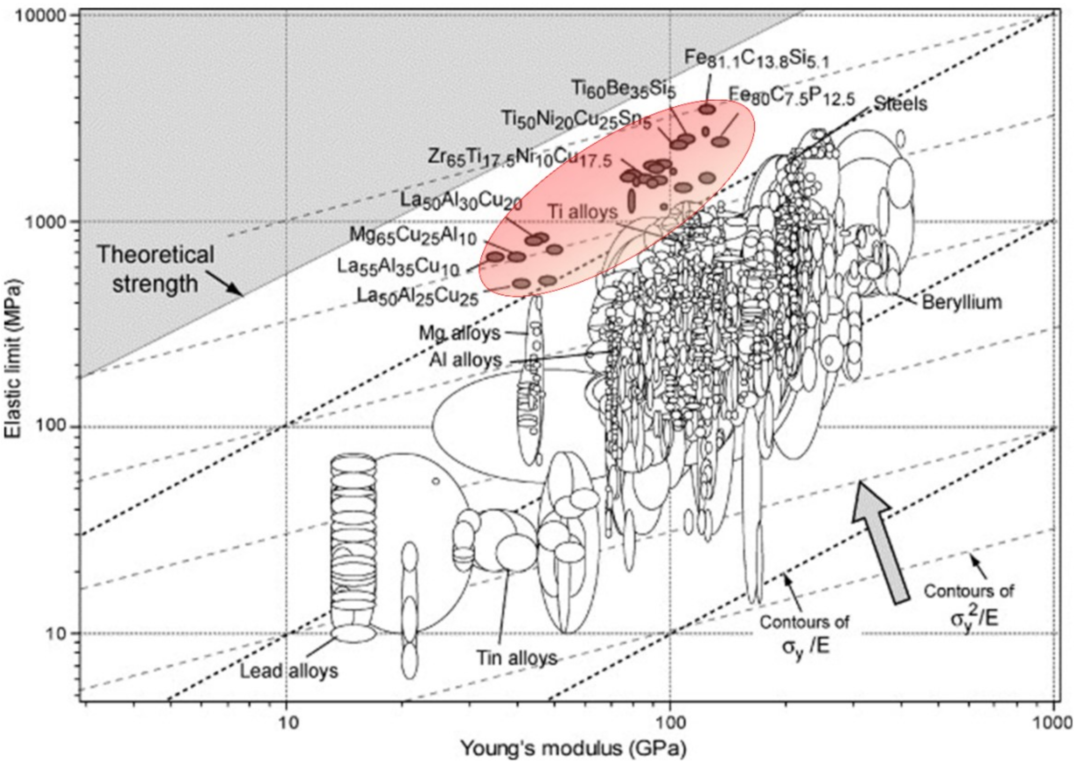

Figure 2-2: Elastic limit in MPa over the Young's modulus (GPA) for different classes of materials. The elastic limit of metallic glasses (red oval) reaches almost the theoretical strength. Crystalline materials like Mg alloys, Al alloys and steels exhibit lower elastic limits. The Figure is reproduced from [14].

2.1.3 Structure

BMGs obtain their unique mechanical properties, which are described in the previous section 2.1.2, from their amorphous structure. For this reason, the structure of BMGs is shortly described in this section.

The structure of solids can be crystalline or amorphous. Crystals show long-range order through the periodic arrangement of the atoms. Amorphous solids (glasses) are frozen liquids, which possess the amorphous structure of the liquid, which possesses no long-range order. The structure of crystalline material is in comparison to glasses relatively easy to investigate by diffraction methods as the atoms arrange periodically in a lattice. This fact does not diminish the effort made in the field of crystallography. Already the existence of a scientific field like crystallography proofs the complexity of the structure of crystalline materials. The fact rather shows that structure determination in liquids and glasses is even more difficult.

The structure of a glass is not distinguishable from the structure of the supercooled liquid at the temperature where it was frozen-in [1]. Therefore, the structure of the liquid state is the key to understand the glassy structure as well. Very little is known about the structure of glasses and liquids in general, but especially for atomic glass-formers like BMGs. In polymeric and oxidic glass-formers, at least the bricks from which the structure is built are known. In polymeric glasses the bricks are the polymer chains, in oxidic glass-formers like GeO_2 and SiO_2 there are GeO_4 and SiO_4 tetrahedra which are linked over the oxygen as bridging element with each other. In those glasses, the spatial arrangement of the chains and tetrahedra is the still debated part. In oxide glasses the long-range order seems to be destroyed by internal strains that cause a large scatter in the bond angle making a periodic arrangement impossible [15]. But as already said, the short-range order of the atoms is known. This is a big advance in comparison to BMGs.

In metallic liquids and glasses the short-range order is unknown. There is short-range order and even medium-range order over a few atomic distances, but the exact atomic arrangement is still not clear. Although the first pioneering work on atomic structure in metallic glasses and melts suggested a rather randomly packed structure [16–18], there is good evidence that the atoms arrange in icosahedra [17] and similar clusters [19]. An icosahedron is a regular polygon with 12 corners and 20 planes, where it is named after. It consists of 13 atoms, from which 12 are placed in corners and one is in the center of the polygon. An icosahedron is a highly symmetric polygon with a five-fold symmetry. Looking at the single icosahedron, it has a lower energy state with respect to structures found in crystals like face-centered cubic (fcc) and hexagonal (hcp) [20]. Using the Lennard-Jones potential, the binding energy of an atom in one of the corners to its neighbors is in a first approximation about 10% higher than in a fcc structure. This makes single icosahedra in liquids more stable than a fcc-structure. But the phase space cannot be filled with icosahedra as they possess a five-fold symmetry. Therefore, they are energetically less favourable than fcc- and hcp- structures on a global scale. The fact that they are locally favored but not globally could explain some phenomena as eutectics in multicomponent melts [21], the large undercooling of glass-forming liquids and phenomena like liquid-liquid phase transitions [22], which is the main topic of this work. Thanks to sophisticated techniques like neutron scattering in combination with levitation and angstrom-beam electron diffraction (ABED), the existence of icosahedra could be proved in monatomic liquid melts [23] and in a metallic glass [24]. With ABED it was possible for the first time to see icosahedral cluster not only in a diffraction pattern, but in a two-dimensional projection. Figure 2-3 shows the results of the ABED measurements and the expected appearance from simulations. Beside the experimental progress the development of structure models enlarged the scientific knowledge of structure determination in liquids and glasses. In the last decade, the efficient cluster packing model suggested by Miracle [25–28] has been successful in describing the structure of metallic glasses as well as predicting new glass-forming compositions only based on topological aspects and dense packing.

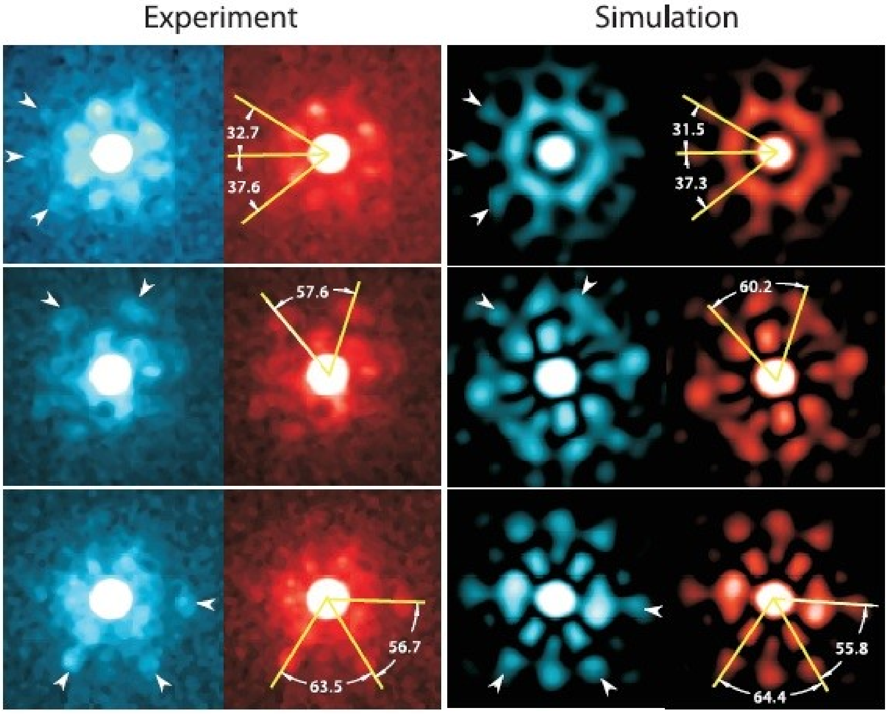

Figure 2-3: Icosahedral clusters observed in metallic glass-former $Zr_{80}Pt_{20}$ by angstrom-beam electron diffraction and the corresponding clusters expected from simulation. The figure has been has been reproduced from [24].

Miracle Model

The model is based on several assumptions: (a) there is a maximum of four topologically different species in metallic glasses. The solvent atom species Ω, which is the atom species with the highest portion in the alloy, and three different solute species with decreasing atomic radii from α over β to γ. (b) The atoms form clusters. The primary clusters are α-centered Ω clusters. The coordination number of the cluster, which is the number of next neighbors of the α species, depends on the size ratio between α and Ω species. (c) The clusters are arranged in face-centered cubic or hexagonal structures to fill the phase space efficiently. (d) The clusters can be vertex-, edge- and face-sharing leading to different sizes of inter-cluster octahedral and tetrahedral interstices within this structure, which the β, γ species occupy. Figure 2-4 illustrates the structural arrangement proposed by the model two-dimensionally (Figure 2-4a) and three-dimensionally (Figure 2-4b). The two-dimensional schematic picture shows the primary α-centered and secondary β-centered clusters in the <100> plane of a fcc cluster structure. In the three-dimensional visualization the α sites are surrounded by Ω icosahedral clusters (not visible) and the β species (purple) occupies the octahedral interstices and the γ species (red) the tetrahedral interstices. The model concentrates on the topological aspects of glass formation and is quite successful in describing the structure of glass-forming alloys. To further improve the predictive capability for new glass-forming alloys the model was modified [29] to account for the chemical interaction of different species. The α species is selected not only by the ratio of the atomic radii with respect to the solvent species but also by the heat of mixing of the different species.

Despite the fundamental approach using topology and chemistry, the model oversimplifies the reality limiting the model to some specific alloy systems where it can be helpful to find new glass-forming alloys. The structure of metallic glass-formers remains a puzzle [1], which has to be solved using advanced experimental techniques and simulations.

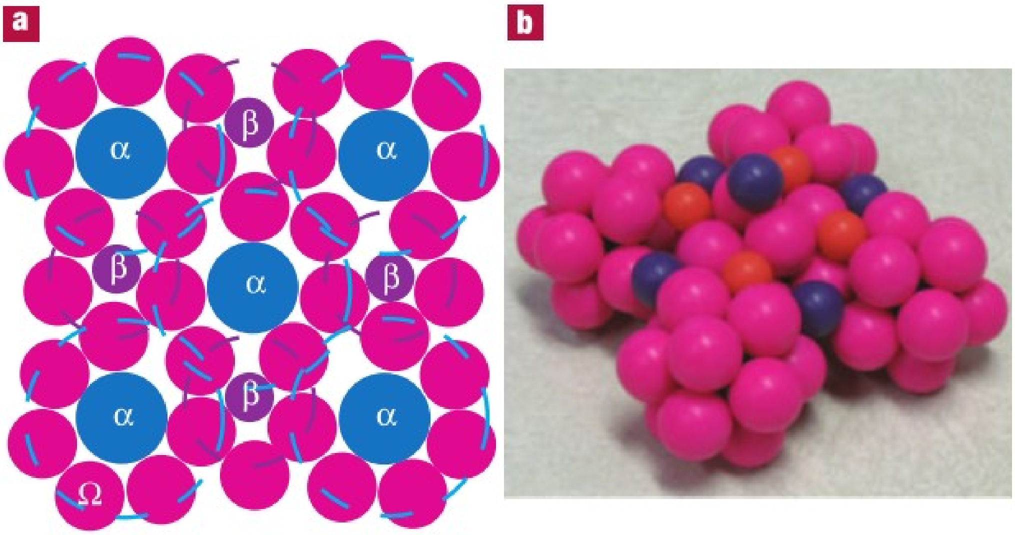

Figure 2-4: a) Schematic two-dimensional illustration of the clusters suggested by the Miracle. b) Three-dimensional model of the efficiently solute centered atomic clusters proposed by Miracle. The figure is taken from [27].

2.1.4 Glass formation and prevention of crystallization

A glass, no matter if it is a polymeric, oxidic or metallic glass is formed when the viscosity of a liquid has increased upon cooling to a value of about 10^{12} Pa s and crystallization has been avoided. The most descriptive way to explain crystallization or rather the way to circumvent it, is a time-temperature-transition (TTT) diagram. Figure 2-5 shows a schematic TTT diagram of a glass-forming liquid. As can be seen, the crystallization range of the liquid in the diagram looks like a nose. The nose is a result of the interplay between the kinetics and the thermodynamics of the undercooled liquid.

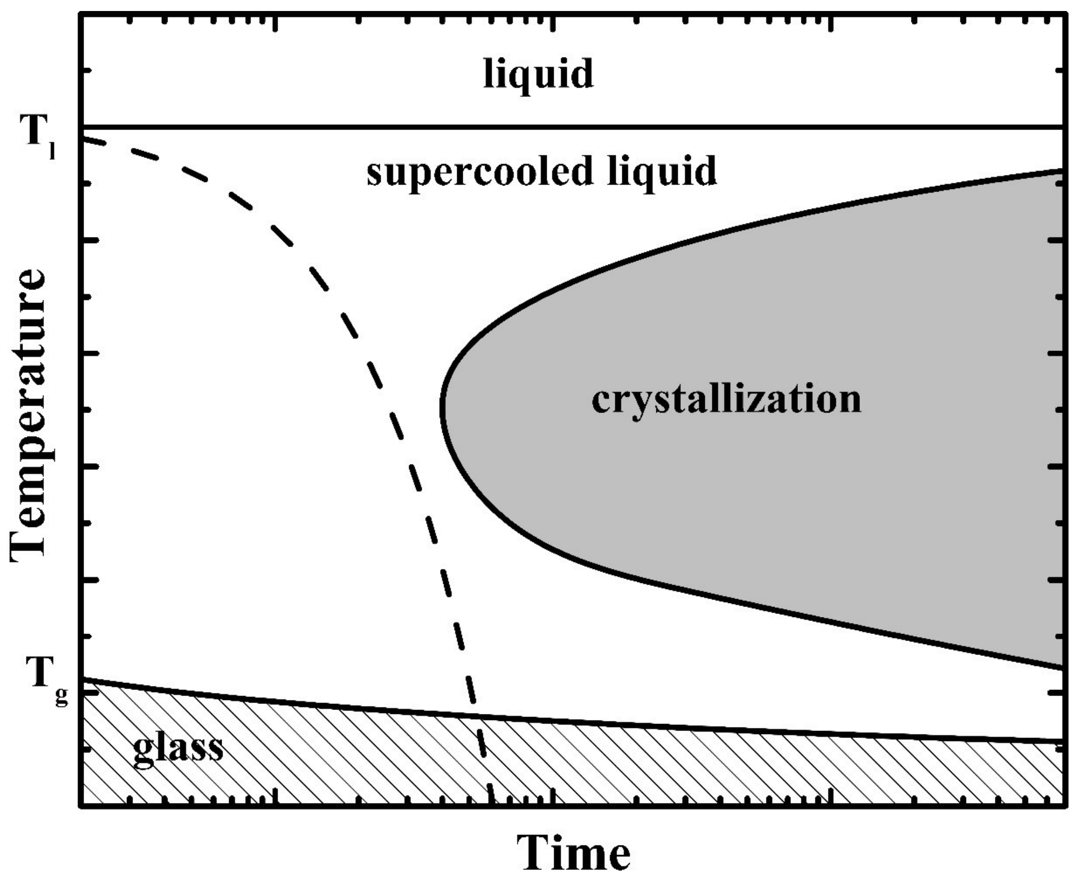

Figure 2-5: Schematic time- temperature-transition diagram of a glass-forming alloy. The cooling rate (dashed line) must be fast enough to avoid the crystallization (grey area) of the supercooled liquid below the liquidus temperature T_l to form a glass at the glass transition temperature T_g.

Crystallization is a first order phase transition for which a thermodynamic driving force is needed. The Gibbs free energy of the crystal G^x must be smaller than the Gibbs free energy of the liquid G^l:

$$G^l - G^x = \Delta G^{l-x} < 0.$$

This is the case below the liquidus temperature of the material as illustrated in Figure 2-6. But crystallization does not occur immediately. There is an energy barrier which must be overcome to crystallize the liquid. This barrier is the interfacial energy between the forming nuclei of the crystal and the remaining liquid. Therefore, ΔG^{l-x} is given by:

$$\Delta G^{l-x} = -\Delta G_V + \Delta G_S,$$

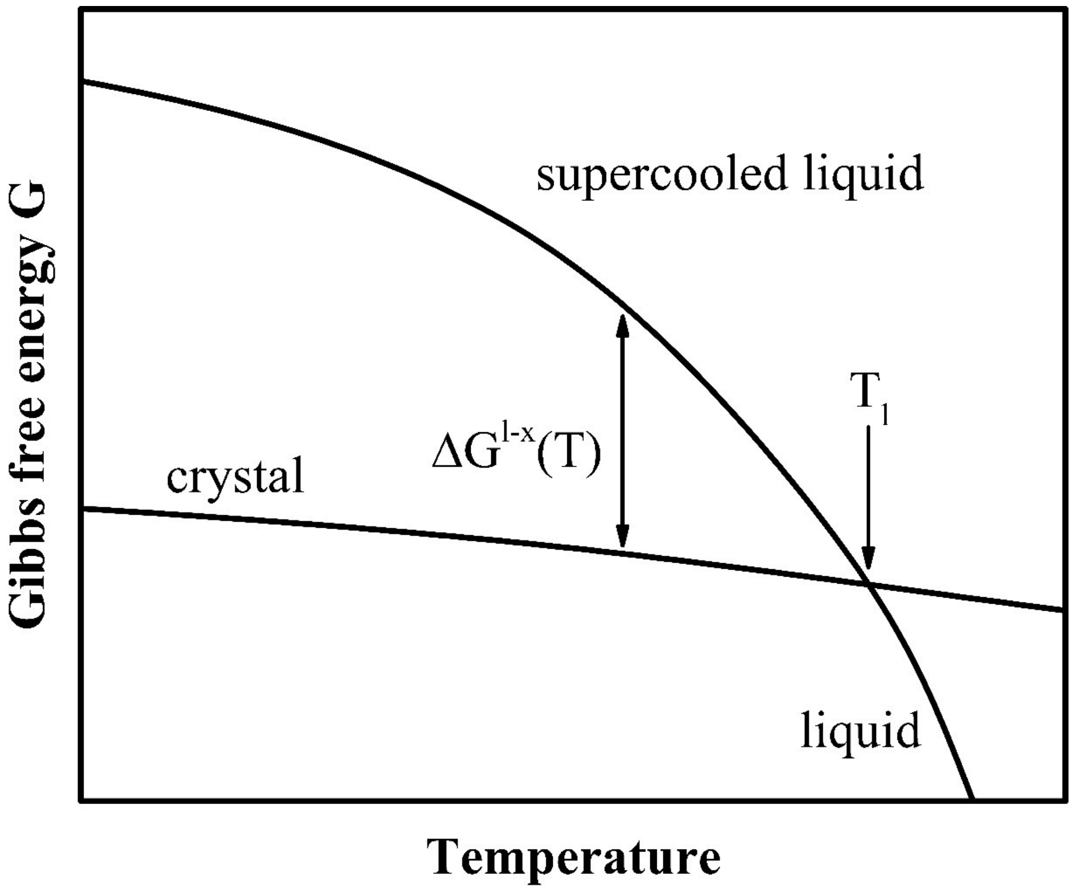

Figure 2-6: Gibbs free energy curves of liquid and crystal. Below the liquidus temperature T$_l$ of the material, there is a driving force (ΔG^{l-x}) for crystallization of the supercooled liquid.

where ΔG_V is the energy gain by crystallization of the volume V, which is negative, and ΔG_S is the energy required to form the liquid solid interface. When spherical nuclei are considered

$$\Delta G^{l-x} = -\frac{4}{3}\pi r^3 \Delta g_v + 4\pi r^2 \sigma,$$

where r is the radius of the nucleus, Δg_v is the energy gain per volume unit and σ is the interfacial energy per area unit. The critical radius r^* is given as

$$r^* = \frac{2\sigma}{\Delta g_v},$$

where ΔG^{l-x} exhibits its maximum. When this critical size is reached by a nucleus, the system lowers its energy by growing the nucleus and the material begins to crystallize. The height of the energy barrier ΔG^* is then

$$\Delta G^* = \frac{16\pi}{3} \frac{\sigma^3}{\Delta g_v{}^2}.$$

As $\Delta g_v \propto \Delta T$, where ΔT is the undercooling, r^* and ΔG^* decrease with the undercooling [30]. But the kinetics and diffusivity slow down rapidly with temperature.

As already mentioned, these two factors determine the TTT diagram. At high temperatures above the nose, the driving force for crystallization is small and therefore the critical radius of a stable nucleus is large, which leads to long crystallization times. At very low temperature below the nose close to the glass transition the kinetics are very sluggish and the low diffusivity impedes the formation and growth of stable nuclei. At the temperature where the crystallization nose is, the combination of relatively fast kinetics and large driving forces is advantageous for crystallization resulting in the shortest time before the crystallization occurs.

From nucleation and growth, some rules to stabilize the liquid against crystallization in the supercooled liquid state can be identified. Thermodynamically, two ways of stabilizing a liquid are possible. At first, the driving force for crystallization $\Delta G^{l\text{-}x}$ should be small, which means that the energy gain by crystallizing a liquid should be a small as possible even for large undercoolings. Secondly, the interfacial energy ΔG_S between liquid and solid should be high. It determines the height of the energy barrier and the critical size of the nucleus. The higher the interfacial energy, the more stable is the liquid against crystallization [31]. From the kinetics, it is clear, that the liquid should exhibit sluggish dynamics already at the melting point to slow down the atomic diffusivity to impede the formation and growth of crystals. The more stable the liquid is against crystallization, the further the crystallization nose is shifted to longer times in the TTT diagram. Figure 2-7 compares a good (red) and a bad (black) glass-forming liquid. For the good glass-former the crystallization is shifted to longer times and the critical cooling rate needed to form a glass is significantly smaller resulting in a larger critical casting thickness.

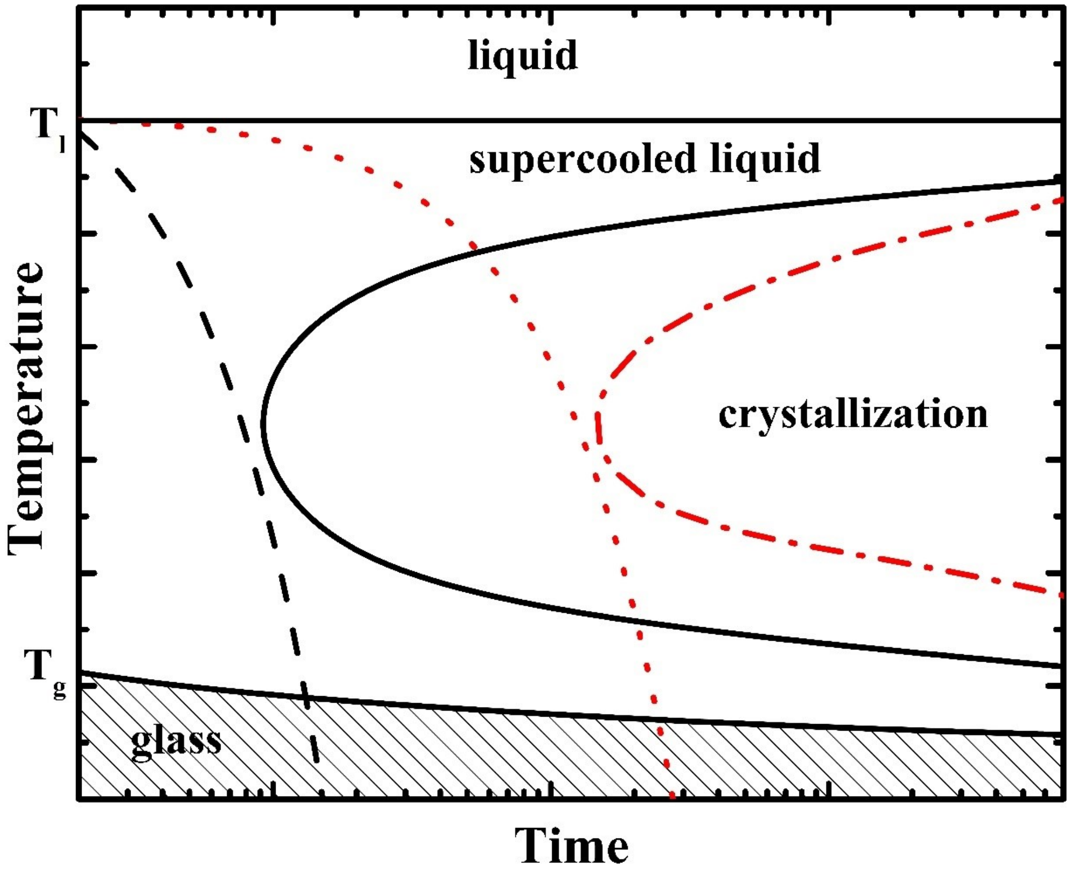

Figure 2-7: Schematic TTT diagram of a good (red, dotted line) and a bad (black) glass-forming liquid. The crystallization nose of the good glass-former is shifted to longer times.

2.2 Glass transition

The glass transition is a kinetic phenomenon. When crystallization is avoided upon cooling a liquid, it ultimately freezes into a glass. The cooling rate which is needed to avoid crystallization is an intrinsic property of each alloy, which has been discussed in section 2.1.4. The glass transition occurs when the liquid is not able to arrange its structure to the temperature changes that are made. It freezes and behaves as a solid on the observation time scale.

Figure 2-8 illustrates the temperature dependence of the structural relaxation time in the liquid. In good metallic glass-formers, like $Zr_{46.75}Ti_{8.25}Cu_{7.5}Ni_{10}Be_{27.5}$, the structural relaxation time increases more than ten orders of magnitude from the liquidus temperature T_l to the glass transition temperature T_g in just a few hundred degrees. The structural relaxation time is the time which is required to reach a

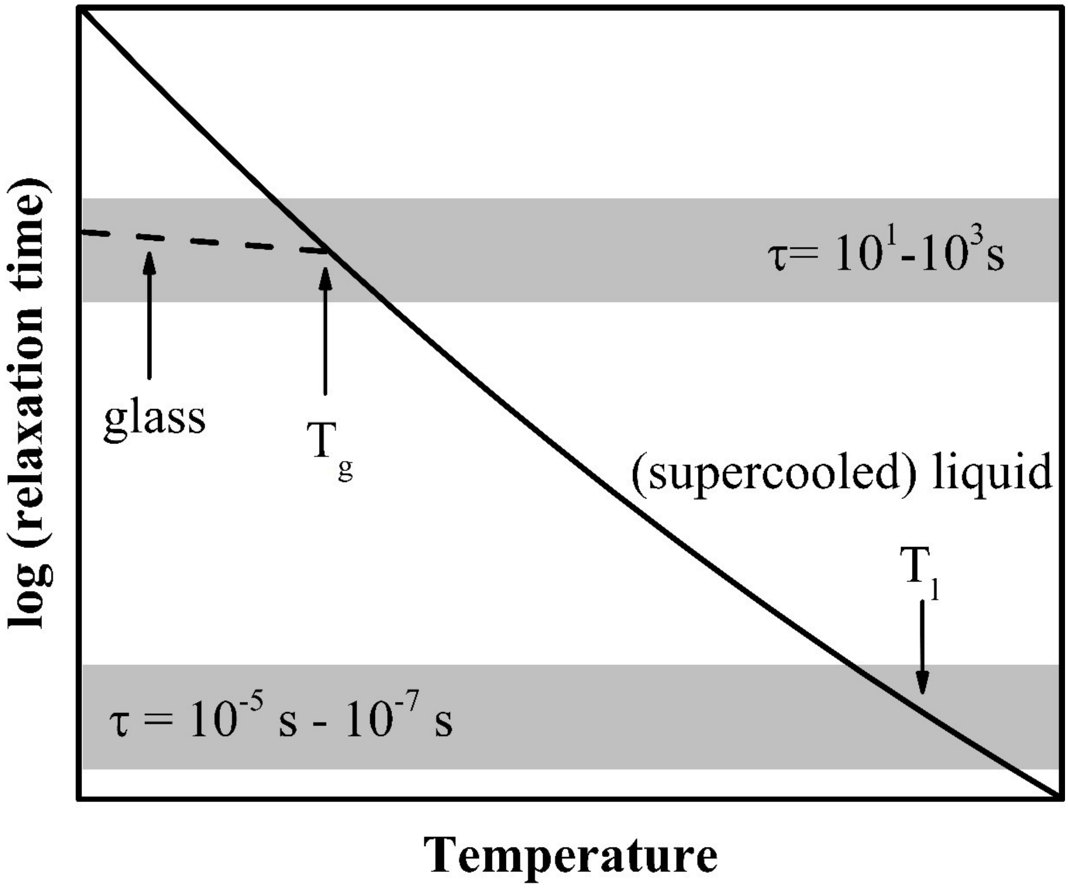

Figure 2-8: Temperature dependence of the structural relaxation time in liquid and glass shown schematically. The glass transition occurs in the range of 10-1,000 s for normal cooling rates. The relaxation time at the liquidus temperature T_l is about ten orders of magnitude lower. The relaxation time at the liquidus temperature does not dependent on the cooling rate but deviates considerably among liquids.

complete rearrangement of the configuration in the liquid. Upon cooling this is the minimum time required for the atomic arrangement to adapt to the new temperature. As soon as the observation time scale -which is inversely proportional to the cooling rate- becomes smaller than the structural relaxation time, the liquid is unable to arrange its structure within the timeframe of observation to the temperature changes and the liquid freezes to a glass. This crossover is the glass transition. It occurs at relaxation times τ between 10 s-1000 s for standard cooling rates around 1 K s^{-1}. The glass transition is observable in relaxation time and viscosity as a clear change in the slope of the temperature dependence of both properties. The glass exhibits a shallower dependence than the glass as illustrated in Figure 2-8. It is also visible in properties like volume and enthalpy. Figure 2-9 shows the influence of the glass transition on properties like volume and enthalpy. As can be seen T_g depends on the cooling rate. The higher the rate the higher T_g. The liquid exhibits a steep temperature

dependence from which the glass clearly deviates to a shallower dependence. At the transition the current configuration of the liquid is frozen into a glass as it cannot adapt to temperature changes in the way the liquid was able due to the missing time which would be necessary.

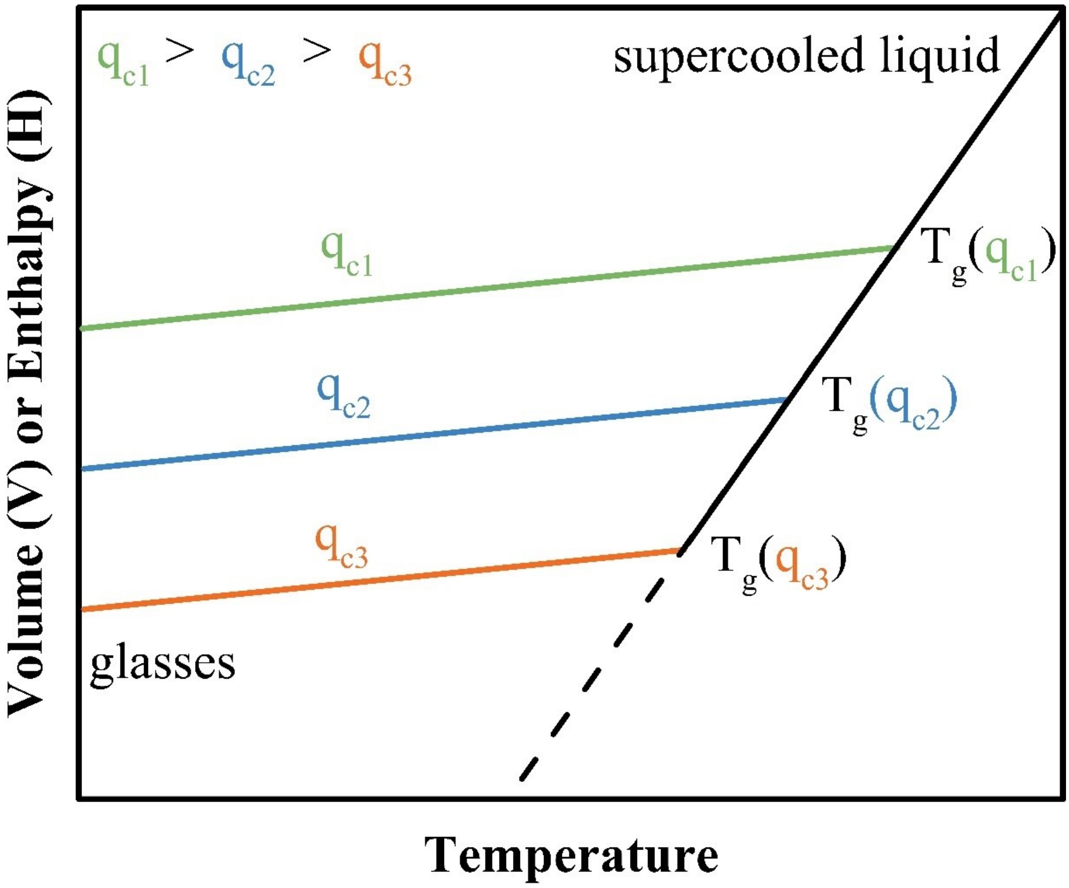

Figure 2-9: Temperature dependence of volume and enthalpy in the supercooled liquid and the glasses. Cooling rate dependence of T_g. The higher the cooling rate, the higher T_g.

The glass transition leads to a decrease of the heat capacity of the material as illustrated in Figure 2-10. The molar heat capacity of the lead oxide glass F2 is shown. As can be seen, the heat capacity decreases about 20% in the glass transition region. This decrease is very different for different glass-formers and is used to rank glass-formers in terms of thermodynamic fragility. The term fragility is described in section 2.4. The heat capacity is considered to consist of two contributions, the vibrational part and the configurational part. As the liquid freezes, the configurational part of the heat capacity is frozen and the heat capacity of the glass reflects only the vibrational part of the heat capacity of the liquid [32].

Due to the decreasing free volume upon cooling, the atoms need to perform cooperative motion to change the configuration. The further the material is cooled, the larger the number of atoms is, which are needed for a cooperative rearrangement. With the increasing number of atoms, which are needed for the rearrangement, the correlation length or the volume, which is needed to take part in the rearrangement, increases. This increasing correlation length is the reason for the increasing relaxation time in vicinity of the glass transition. Additionally, the dynamics of supercooled liquids is considered to become more heterogeneous with increasing correlation length upon cooling in the ultra-viscous liquid close to the glass transition [33,34,43,35–42]. The observation of increasing heterogeneity and cooperativity upon cooling was further developed through establishing multipoint dynamical susceptibilities to quantify the increase of the heterogeneities arising in the ultra-viscous state and the sizes of the cooperatively rearranging regions [44–50] in supercooled liquids. This statistic method is described in section 3.2.1.

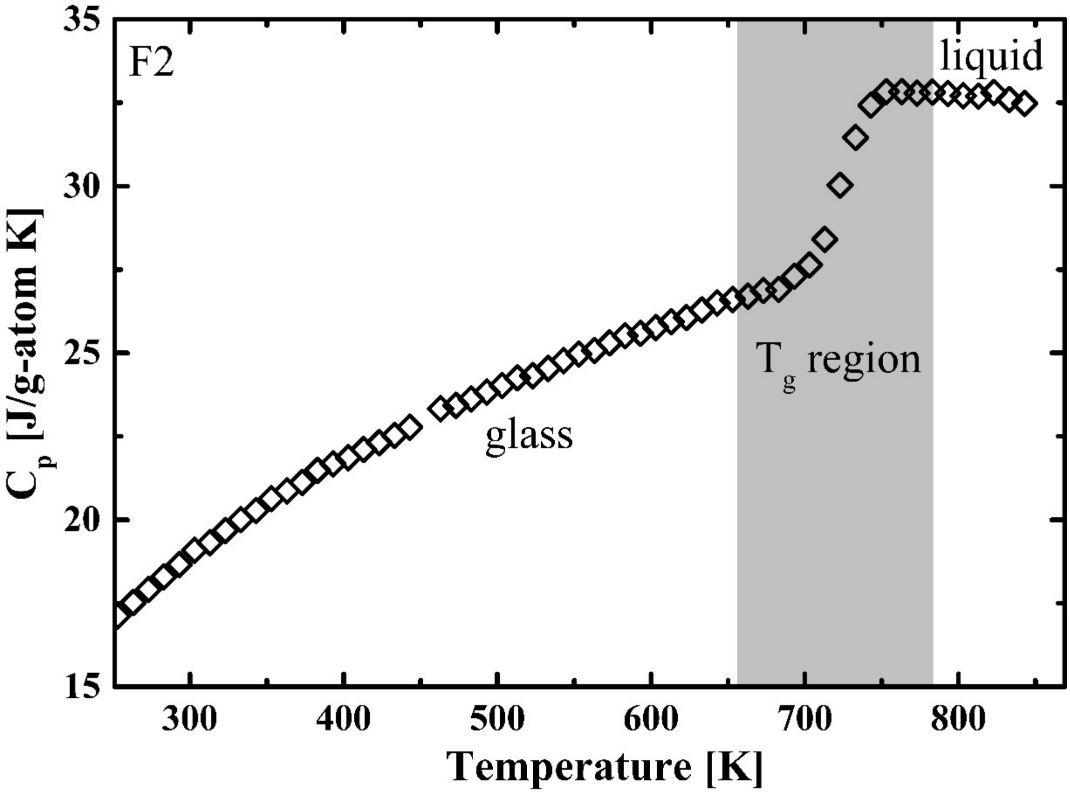

Figure 2-10: C_p data of the lead oxide glass F2 around the glass transition. The material exhibits a steep decrease in heat capacity upon cooling at the glass transition. The figure is reproduced from [51].

2.3 Aging

Once a glass is formed, the material is trapped in a high energy state, which is no condition it is going to stay in. The glass starts to evolve towards the metastable supercooled liquid, which is the easiest achievable low energy configuration. The glass locally rearranges its structure releasing enthalpy and free volume. This evolution is called aging. It occurs at any temperature, but it becomes considerable in the glass transition region ($T_g > T > T_g$-100 K) due to the elevated dynamics in that temperature range. Aging in the glassy state leads to a lower energy state of the material and a densification as mentioned above. It can last significantly longer than the relaxation time of the corresponding liquid suggests especially when the temperature is reached in heating from the glass [52]. Figure 2-11 shows this asymmetry of approach.

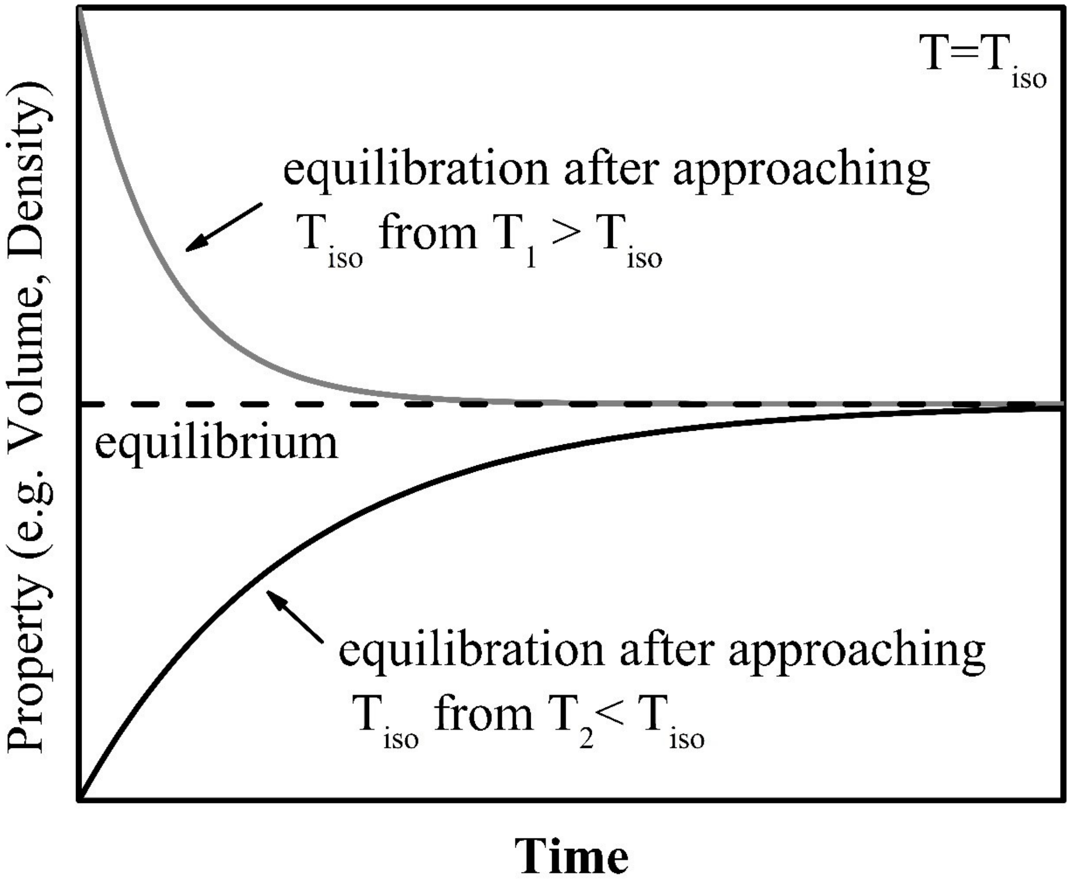

Figure 2-11: Asymmetry of approach. The equilibration of a system at a temperature T_{iso} is significantly faster when approaching the temperature from the (metastable) equilibrium upon cooling (red line) in comparison to approaching the temperature from the glassy state upon heating (blue line).

When a temperature is reached upon cooling from the (metastable) equilibrium liquid, the material equilibrates relatively fast, whereas when the temperature is reached upon heating from the glass, the equilibration can last several orders of magnitude longer [53,54]. This is a very important fact that is crucial to better understand the aging behavior of glasses and the associated structural changes.

Aging appears to be very different on the microscopic and macroscopic length scale. Looking at macroscopic viscosity and volume relaxation experiments below the glass transition, metallic glasses seem to evolve continuously towards the metastable equilibrium liquid (see e.g. [55]). The picture is much more complex when looking at the aging on the microscopic scale. There, the aging process appears to be discontinuous where the aging is interrupted by long time intervals where the equilibration seems to be stuck (see e.g. [52]). This topic is discussed based on the results of this work in chapter 4.

2.4 Fragility

2.4.1 Kinetic Fragility

The term fragility was introduced by Angell (see e.g. [56–59]**)**. He used the existing concept of temperature scaled plots of kinetic properties like viscosity and relaxation time [60,61] to compare the kinetics of glass forming liquids. Therefore, plots of the kind shown in Figure 2-12 **Fehler! Verweisquelle konnte nicht gefunden werden.**are often referred to as “Angell plot”. The glass transition temperature T_g^*, which is defined as the temperature where the viscosity is 10^{12} Pa s or the relaxation time is 100s, is the scaling temperature. With it the glass-forming liquids can be compared in terms of relaxation time and viscosity. Angell introduced the term fragility as a measure for the temperature dependence of these kinetic properties. Liquids, which exhibit an Arrhenius-like temperature dependence are considered as strong. Examples for strong liquids are oxidic glass-formers like SiO_2 and GeO_2 [62,63]. Liquids, which exhibit a steep, super-Arrhenius temperature dependence of viscosity and relaxation time at T_g, like O-terphenyl [63], are considered as fragile. To quantify the fragility of a liquid, the slope m of the viscosity or relaxation time curve at T_g^* is given as

$$\mathrm{m} = \left|\frac{\mathrm{dlog}(\Phi)}{\mathrm{d}(^{T_g}/_{T})}\right|_{T=T_g} \quad .$$

Φ is viscosity or relaxation time. The steeper the slope, the more fragile the glass-forming liquid. The D* parameter of the Vogel-Fulcher-Tamann (VFT) equation [64–66]

$$\Phi(\mathrm{T}) = \Phi_0 \exp(\frac{\mathrm{D}^*\mathrm{T}_0}{\mathrm{T}-\mathrm{T}_0}) \quad ,$$

where Φ_0 is the high temperature limit of viscosity or relaxation time, T is the temperature and T_0 is the temperature, at which the property diverges, is a measure of the fragility as well [30]. Large values of D* correspond to strong liquids, small values to fragile ones. In the broad variety of glass-forming liquids, metallic glass-forming liquids are intermediate glass formers with D* = 9-25 [67,68] in comparison to D*= 150 for GeO_2 and D*= 3 for O-terphenyl (see Figure 2-12**Fehler! Verweisquelle konnte nicht gefunden werden.**).

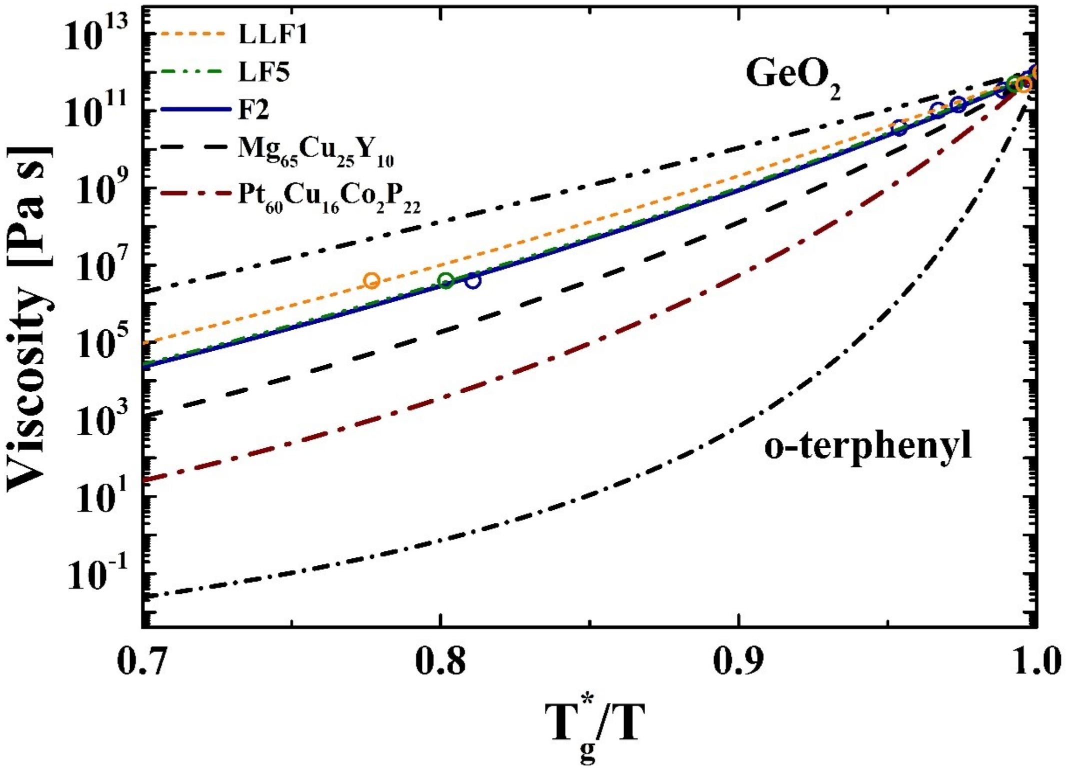

Figure 2-12: T_g^* scaled plot of the temperature dependence of viscosity for several glass-forming liquids [51]. GeO_2 [63] is a strong liquid with an Arrhenius-like behavior. O-terphenyl [63] represents fragile glass-formers with a super- Arrhenius temperature dependence of viscosity. The flint glass-formers F2, LF5 and LLF1 [51,69] and the bulk metallic glass-forming liquids $Mg_{65}Cu_{25}Y_{10}$[70] and $Pt_{60}Cu_{16}Co_2P_{22}$ [68] intermediate glass-formers with fragility parameters D^*=37.1 for F2, D^*=38.0 for LF5,D^*=50.7 for LLF1, D^*=22.1 for $Mg_{65}Cu_{25}Y_{10}$ and D^*=11.8 for $Pt_{60}Cu_{16}Co_2P_{22}$.

2.4.2 Thermodynamic Fragility

Theories and experimental results suggest a connection between kinetic and thermodynamic behavior of glass forming liquids, e.g. [71–74]. For this reason, the term thermodynamic fragility has been defined. Here, the thermodynamic properties of glass-forming liquids are compared to rank them analog to what has been introduced by Angell in terms of kinetic fragility. The way the thermodynamic fragility is determined is not uniform. In the following section three existing concepts are described.

The decrease in the molar heat capacity (ΔC_p) upon cooling at the glass transition is the easiest way to compare glass-forming liquids in terms of their thermodynamic fragility. Figure 2-13 compares different glass-forming liquids. The kinetically strongest glass-forming liquid, which is shown, GeO_2, exhibits the smallest $\Delta C_p(T_g)$, whereas the most fragile glass-former $Pt_{60}Cu_{16}Co_2P_{22}$ shows the largest. Therefore, strong liquids exhibit small decreases whereas fragile liquids exhibit rather large $\Delta C_p(T_g)$ [32,51,75] as strong liquids are considered to be more ordered and possess less accessible configurations at T_g. At the glass transition only the configurational part of the heat capacity, which reflects the entropy of the system, is frozen-in, whereas the vibrational part remains untouched [32]. The fewer accessible configurations in strong liquids lead to a smaller amount

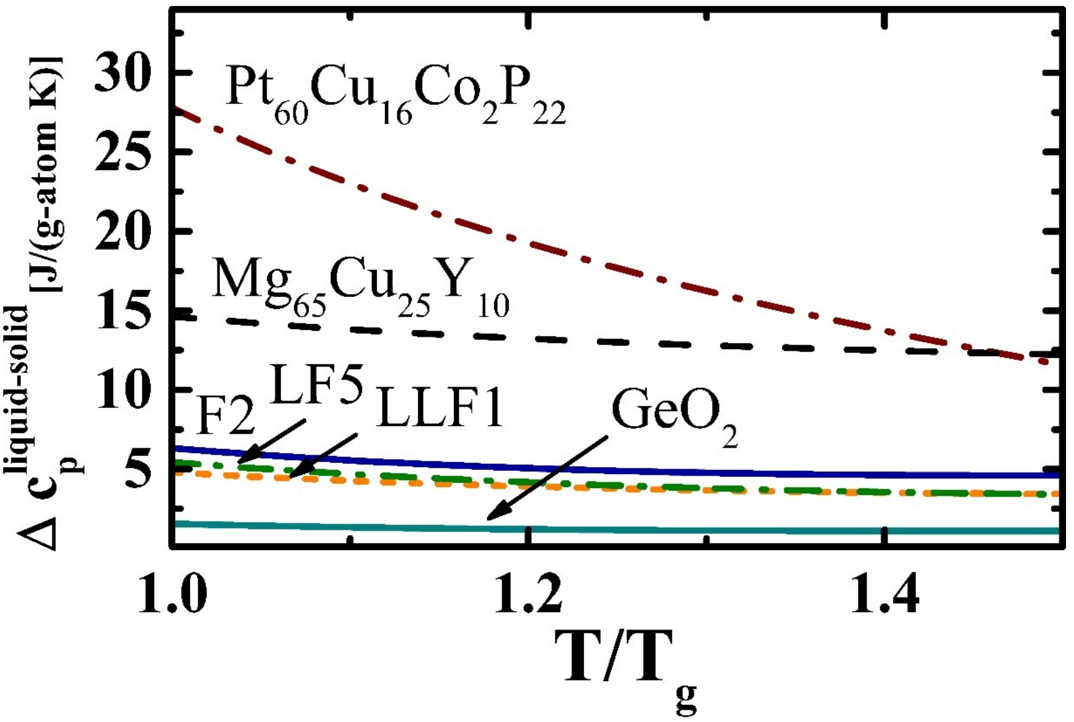

Figure 2-13: Difference between the heat capacity of the liquid and the glass at the glass transition. The figure is reprinted from [51].

of configurational heat capacity and entropy, which is frozen-in and hence to a smaller heat capacity decrease. In this first concept, the thermodynamic fragility increases with increasing $\Delta C_p(T_g)$ and can be correlated with the kinetic fragility [51,74,76,77].

A second approach to determine the thermodynamic fragility is to look at the slope of heat capacity curve in during the glass transition [78]. Strong liquids like GeO_2 exhibit a very shallow slope during the glass transition, whereas fragile materials like BMGs exhibit steeper slope.

Another method is to look at the slope of the heat capacity upon cooling towards the glass transition. Strong liquids exhibit constant or even decreasing heat capacities, whereas fragile liquid show increasing heat capacities in the liquid regime upon cooling, when the glass transition is approached [51]. It has been postulated that the kinetic behavior is associated to the relative position of T_g to an underlying order-disorder transition [79]. In strong liquids, this transition occurs at temperatures far above the melting point leading to decreasing heat capacity upon approaching T_g on the low temperature flank of the transition. In glass-formers that appear kinetically fragile the transition is found in the deeply undercooled liquid [77,80–83] or might be even disguised by the glass transition, but it causes an increase in heat capacity upon cooling as the transition is approached. For further information on this topic please see section 2.4.4.

The loss of configurational entropy upon cooling a liquid towards T_g is a third way of defining the thermodynamic fragility. It seems to be proportional to the kinetic changes measured in transport properties like viscosity and relaxation time [63]. The excess entropy, which is the difference in entropy between liquid and crystal, can be determined as a function of temperature. The temperature dependence of the excess entropy is then used as a measure of the thermodynamic fragility [63,67,84]. But there are several drawbacks to this approach. The excess entropy consists of two contributions, the configurational and the vibrational entropy. It was suggested that the excess entropy is proportional to the configurational entropy change. But there are exceptions, e.g. silicate glasses, as their vibrational distribution to the excess entropy is larger than in other glass formers [63,85,86].

All three definitions seem to work for most substances, but for all exist exceptions. There is no definition that gives a perfect correlation of kinetic and thermodynamic fragility.

2.4.3 Structural Fragility

The connection between the structure of a liquid and its kinetic and thermodynamic fragility keeps scientists interested for decades [75,87–92]. There is broad consensus that the structure of a liquid is strongly correlated to its kinetic and thermodynamic properties [75]. Considering metallic glass-forming liquids, the structure seems to develop from an only short-range ordered liquid at high temperatures to a medium range ordered liquid when approaching T_g, e.g. [3,27].

Recently, an empirical correlation, that connects the kinetic fragility of a liquid with structural changes upon cooling has been established [81]. It was found, that structural changes in the medium-range order between the 3rd and 4th coordination shell, which is on the length scale of ~1nm, reflect the kinetic changes when cooling a liquid. Strong liquids exhibit small changes, whereas fragile liquids show more pronounced changes on this length scale.

In addition to that, the static structure factor at the peak position of the first sharp diffraction peak $S(Q_1)$ changes differently upon cooling towards T_g for fragile and strong glass-forming liquids. Fragile liquids exhibit more pronounced changes in this quantity especially when approaching T_g in comparison to strong liquids [75,93,94].

2.4.4 Fragile-to-strong transition

For many glass-forming systems, the viscosity and relaxation times seem to be describable with a single VFT equation from T_g up to very high temperatures, which are still accessible through experiment.

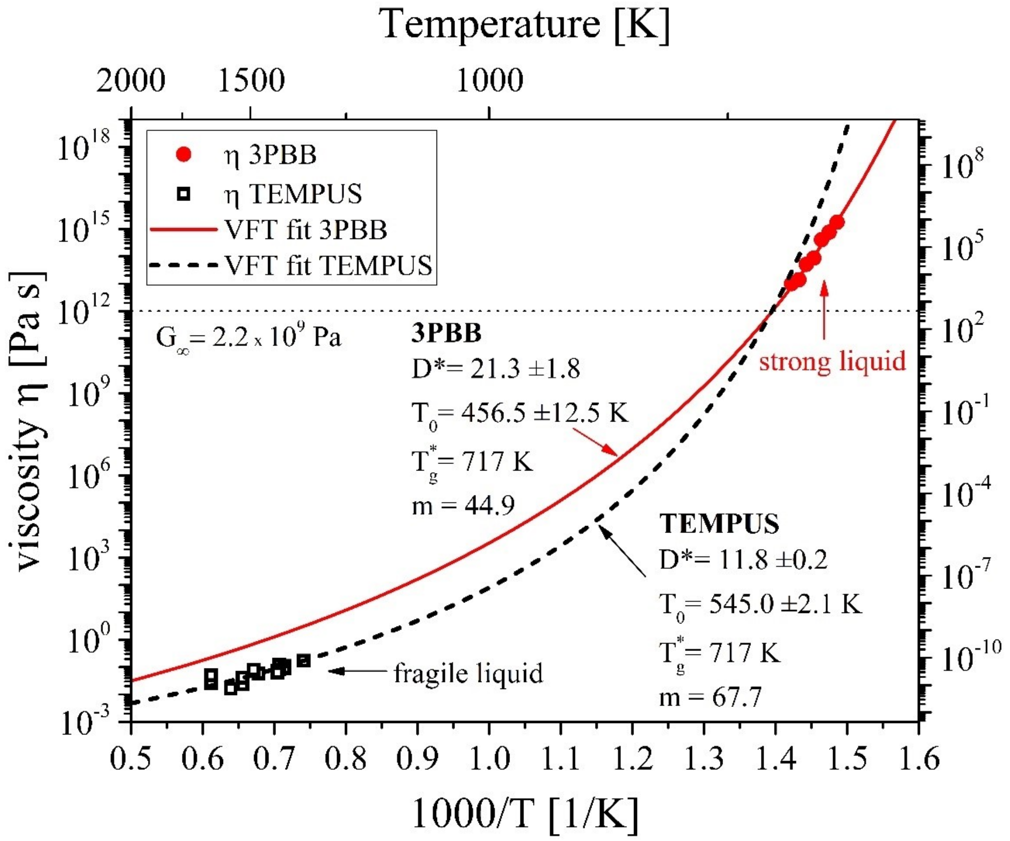

Figure 2-14: Fragile-to-strong transition in the $Fe_{67}Mo_6Ni_{3.5}Cr_{3.5}P_{12}C_{5.5}B_{2.5}$ bulk metallic glass-forming liquid. The viscosity data measured around T_g appear significantly stronger

(D^*= 21.3±1.8) than the viscosity measured at high temperatures (D^*= 11.8±0.2). The plot is reproduced from [95].

But for some other systems, measurements of viscosity show a significant difference between fragilities determined from high and low temperature measurements. At low temperatures the measurements suggest stronger behavior than at high temperatures. Figure 2-14 illustrates this observation for a Fe-based bulk metallic glass-former.

The fragility parameter D* from the VFT fitting is significantly larger for the low temperature viscosity indicating stronger behavior than at high temperatures. Therefore, a fragile-to-strong transition from a fragile liquid at high temperatures to a strong liquid at low temperatures was suggested. According to Angell's 'Big Picture' [7], the relative position of the fragile-to-strong transition to the melting point T_m and T_g determines the fragility which is observed experimentally (see Figure 2-15). For strong liquids like silica [96], it is assumed to occur at very high

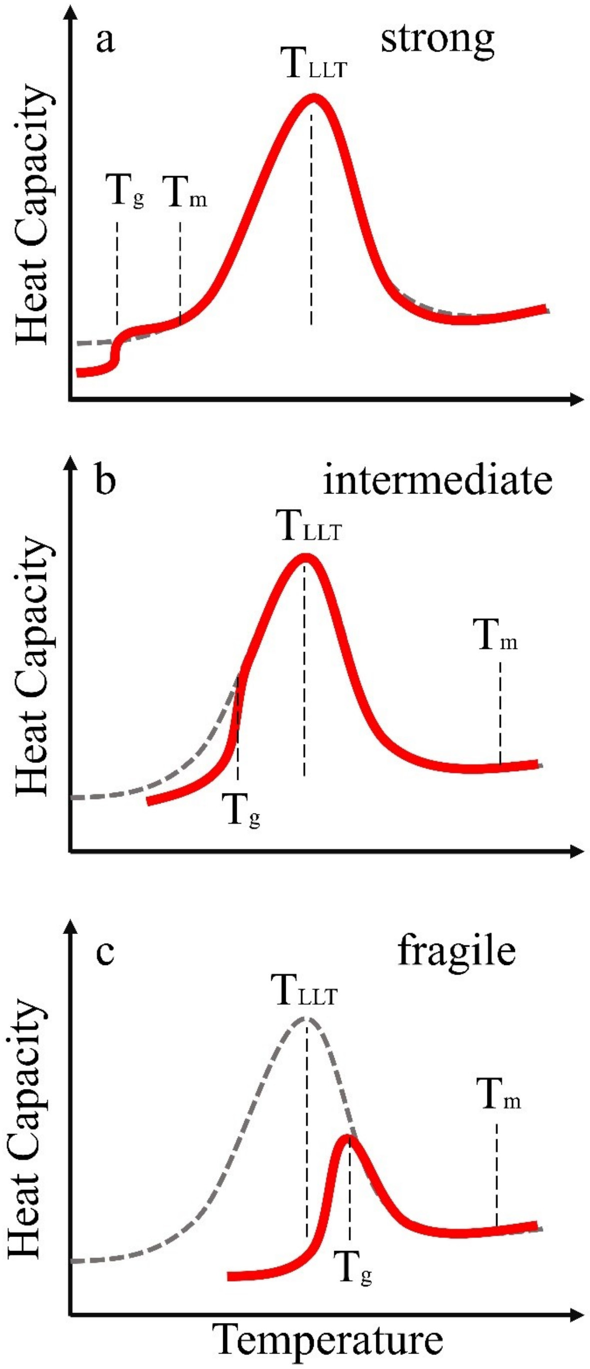

Figure 2-15: Reproduced from Angell's „Big Picture" [7]. (a) Strong glass-formers show a LLT above T_m. (b) In the intermediate case, the LLT occurs between T_g and T_m visible by the heat capacity maximum. (c) Fragile glass-formers exhibit no heat capacity maximum (no LLT) above T_g.

temperatures above T_m. For this reason, silica exhibits strong liquid behavior over the entire observable temperature range. For intermediate strong glass-formers, the fragile-to-strong transition can be observed in the super-cooled liquid region between T_m and T_g [3,75,80,93,95,97–99]. Therefore, these systems exhibit the transition in the temperature range which is accessible in experiment, when crystallization can be avoided. For fragile glass formers like noble metal based MG [67,68] or molecular glass formers like triphenyl phosphite [6], the transition is expected to happen at such low temperatures that T_g hinders the transition and the liquid freezes into a glass beforehand. The fragile-to-strong transition seems to be the kinetic signature of a liquid-liquid phase transition between two distinct liquids with the same composition but different structures, as structural changes accompanying the fragile-to-strong transition have been observed [82,92]. Liquid-liquid transitions are discussed in the following section.

2.5 The liquid-liquid transition

Polymorphic phase transitions, which depend on temperature and pressure, but not on compositional changes, are a common phenomenon. The polymorphic transitions in iron for example are well-known and the reason for the diverse sorts of steel and their tunable properties. Iron shows three polymorphic transitions as a function of temperature. Upon heating the body-centered cubic (bcc) α phase changes from a magnetic to a paramagnetic phase, which is a 2nd order phase transition. At 911 °C, the α phase changes from its bcc structure to the face-centered cubic (fcc) γ phase, which transforms into the bcc δ phase at 1392°C before melting at 1536°C. These transitions are first order phase transitions.

Ehrenfest classified phase transitions. A first order phase transition occurs when the enthalpy H and the volume V, which are first derivatives of the Gibbs free energy G, are discontinuous like it is the case for melting and sublimation processes. 2nd order transitions show continuous changes in H and V, but discontinuities in the 2nd derivatives of G like in heat capacity and compressibility.

A liquid-liquid transition (LLT) is the equivalent to polymorphic transitions of crystalline solids and called polyamorphic phase transitions. It is the phenomenon that a liquid can exist in two or more distinct phases with the same composition but different structure due to changes in pressure and temperature. It is observed in many different kinds of glass-forming liquids, like monoatomic liquids [5,100–102], molecular liquids like water [103] and triphenyl phosphite (TPP) [6,104], oxides [2,96], semiconducting transition metals [4] and metallic glass formers [3,82,105]. The nature of these transitions is still a matter of debate within the scientific community, whether it is (weak) first order or second order and if the transition occurs at a distinct phase boundary or through a two-phase region. There is good evidence for first order transitions especially at high temperatures [101,106,107]. At lower temperatures the LLT has much similarities with order-disorder transitions in crystalline materials like Fe-Co [77], which are in most cases (weak) first order transitions. But as the dynamics of the liquid is very sluggish at low temperatures, the transitions smear out and the distinction between first and second order becomes difficult. Associated to this problem is the question where in the P-T diagram the transition from one liquid to the other occurs. The easiest system to explain the problem is the liquid- gas transition. Such a phase diagram is shown in Figure 2-16. There is the equilibrium phase boundary between liquid and gas on which both phases coexist. When crossing this coexistence line, the material exhibits a first order phase transition. The coexistence line ends in the liquid-gas critical point. Beyond this point, the two phases gas and liquid are not distinguishable anymore and no clear first order transition can be observed. But still on the extension of the coexistence line, which is called the Widom line, the response functions such as heat capacity, compressibility and thermal expansion coefficient still show maxima [108], but smear out when moving away from the LLCP [103]. This situation can also occur between two different liquids resulting in an equilibrium phase boundary between two liquids extended through the Widom line over the liquid-liquid critical point (LLCP). If for a given material the P-T phase diagram is not known, the relative position to the LLCP during the experiment is unknown. Therefore, it could be that the LLT occurs by crossing the coexistence line or by crossing the Widom line beyond the LLCP.

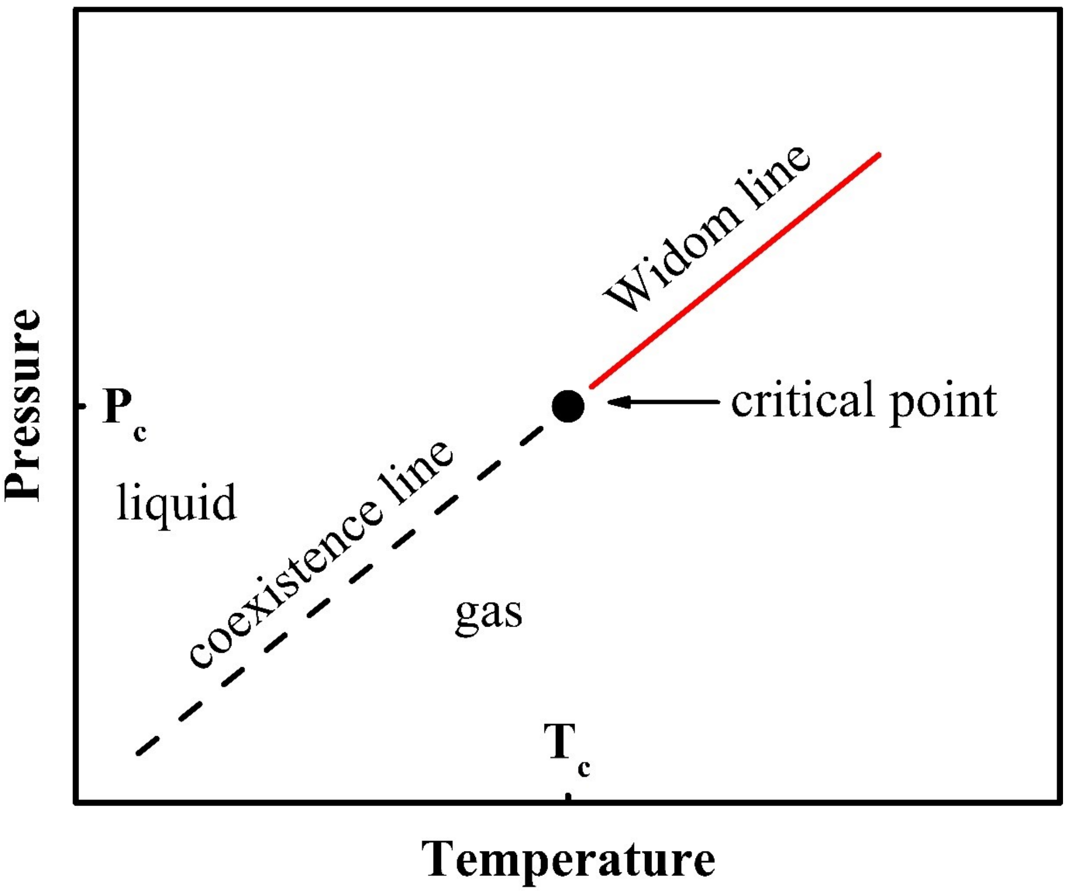

Figure 2-16: Schematic phase diagram. The equilibrium phase boundary between liquid and gas, the coexistence line is shown as dashed line. The extension of the line beyond the critical point, where the two phases cannot be distinguished anymore, is the Widom line (red line).

This fact complicates the situation and has been discussed for example in simulations using the Jagla model [109] and on water [110]. Pressure-induced and temperature-induced LLT have been found. Pressure-induced LLTs seem to be volume driven [111,112]. For temperature-induced LLTs the decisive parameter is the entropy. Some of them seem to be density driven, e.g. [5], but most of them occur to be entropically-driven [2,3,6,82,102,104]. Cooling is associated with a decrease in entropy. This can but does not have to be accompanied by a decrease in volume. Even a volume increase is thinkable, when the entropy loss upon ordering the structure overcompensates the volume increase energetically.

Tanaka developed a model of locally ordered structures to explain LLTs in general [88]. The ideas of this model are explained in following section 2.5.1.

2.5.1 Two-state model based on locally ordered structures

There are numerous two state models, which try to explain fragility, the glass transition and LLTs, e.g. [113–117]. In the following section the model of locally ordered structures proposed by Tanaka [22,88,118–123] will be described. It gives a qualitative idea of the origin of first-order LLTs and a simple explanation for the occurrence in different temperature ranges above T_l, between T_l and T_g and below T_g, for different liquids.

Liquids exhibit icosahedral clusters [24,124–126]. These structures are locally preferred, but they cannot be arranged periodically to fill the phase space. This fact leads to a "frustration" of the liquid, as locally this structure is preferred, but it is not possible to arrange all atoms in this way [127,128]. This observation is the basis for the idea of the two parameter model from Tanaka [22,118–123]. Figure 2-17 illustrates the idea of locally ordered structures (red) in the normal liquid (green).

Normally, only one order parameter, the density, is used to describe a liquid. But for the explanation of phenomena like LLTs one order parameter is not sufficient. Therefore, Tanaka applied a two-parameter model to account for the observation of locally ordered structures that can't be arranged periodically to fill the phase space. In the model, locally ordered structures are embedded in a normal liquid matrix. The order parameter, which controls the normal liquid is density ρ, whereas for the locally ordered liquid clusters a new order parameter L is introduced.

The locally ordered structure exhibits a lower energy level ($E_L<E_\rho$) and a lower specific volume ($\tilde{v}_L<\tilde{v}_\rho$) than the normal liquid. Additionally, the locally ordered liquid shows the lower degeneracy of states ($g_L<<g_\rho$), which leads to a significant loss of entropy when a locally ordered structure is built from the normal liquid structure, $\Delta S = k_B\left(\frac{g_\rho}{g_L}\right) > 0$.

The entropy S of the system is given by:

$$S(L) = -k_B(L\,ln\left(\frac{L}{g_L}\right) + (1-L)\ln\left(\frac{1-L}{g_\rho}\right)),$$

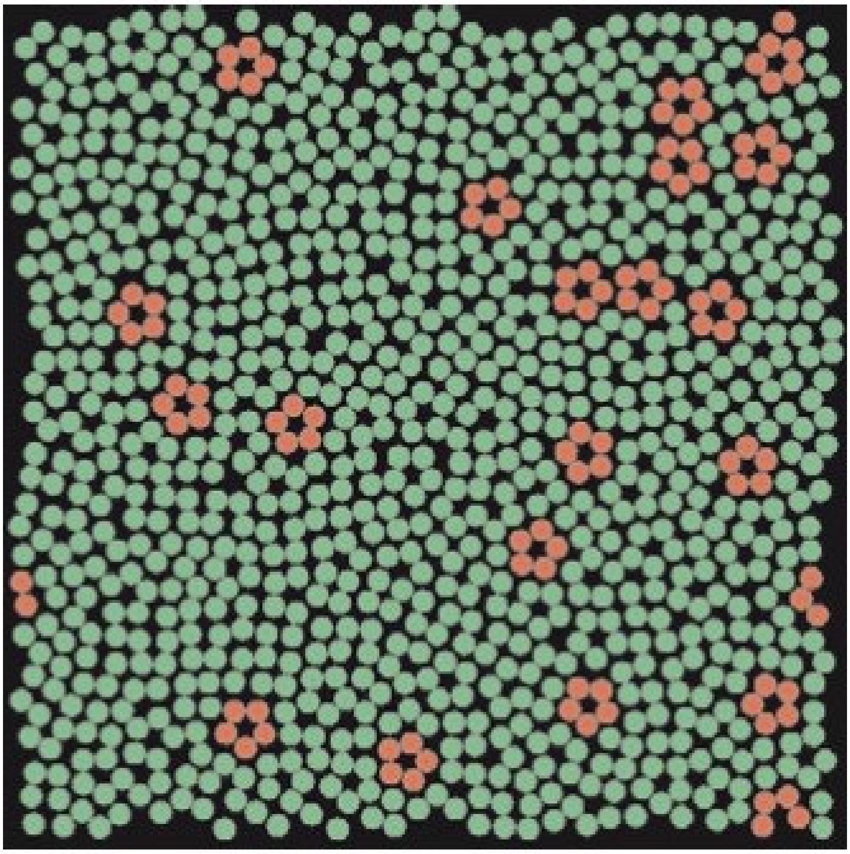

Figure 2-17: Locally ordered structures (red) which are enthalpically stabilized and embedded in the normal liquid structure (green). The figure has been reprinted from [88].

where k_B is the Boltzmann constant, L is the fraction of the system which is locally ordered. The internal energy of the system, if cooperative excitation is considered, is then:

$$U = L\,E_L + (1-L)E_\rho + J\,L(1-L),$$

Where J >0 as the two different types of liquid structure are frustrated with each other. Therefore, it is more probable to have the same kind of structure around a structural unit. For the Gibbs free energy $G = U - TS + pV$ of the mixing of normal and locally ordered liquid one gets:

$$G(L) = L\,E_L + (1-L)E_\rho + J\,L(1-L) + k_B T\left(L\,ln\left(\frac{L}{g_L}\right) + (1-L)\ln\left(\frac{1-L}{g_\rho}\right)\right) + p(L\,\tilde{\mathrm{v}}_L + (1-L)\tilde{\mathrm{v}}_\rho)\,.$$

The energy minimum, which is the equilibrium concentration of L, is found where $\frac{\delta G}{\delta L} = 0$:

$$\frac{\delta G}{\delta L} = \Delta E + J(1-2L) + p\Delta\tilde{v} + k_B T\left(\ln\left(\frac{Lg_\rho}{g_L(1-L)}\right)\right) = 0$$

Here, ΔE is the difference in the energy of the two liquid states E_ρ-E_L and $\Delta\tilde{v}$ is the difference in volume between the two states $\tilde{v}_L$-$\tilde{v}_\rho$. The critical amount of the locally ordered phase L_c is reached when L =0.5. For different models, the temperature at which this happens is the temperature at which the heat capacity shows its maximum and the LLT occurs [109,110,129,130]. This critical temperature can be determined from $\frac{\delta^2 G}{\delta L^2}(L = 0.5) = 0$ as $T_c = \frac{J}{2k_B}$. The temperature at which the transition occurs is given by $\frac{\delta G}{\delta L}(L = 0.5) = 0$ as $T_{LLT} = \frac{\Delta E - p\Delta\tilde{v}}{\Delta S}$. The first order phase transition can only occur when $T_{LLT} < T_c$. The cooperativity of creation of the locally ordered structure represented by J gives the necessary condition for a LLT as it determines T_c. ΔE, $\Delta\tilde{v}$ and Δg determine whether there is a LLT below T_c or not. The interplay of all parameters determines the position of a LLT when the necessary condition is fulfilled. Materials which exhibit a large J and ΔE show a LLT in the stable liquid above the melting point. With decreasing J and ΔE, the possible LLT is shifted to lower temperatures and would occur maybe in the glassy state.

In the following sections, some examples of LLTs are described.

2.5.2 Phosphor

Phosphor possesses four crystalline modifications. The molten white phosphor is a monatomic liquid, which exhibits P_4 molecules under normal pressure at 50°C. When increasing the pressure, the liquid seems to polymerize forming chains with a significantly smaller volume [111,112]. This observation is supported by simulations [131]. This pressure-induced LLT is reversible and appears to be a first order transition from an open molecular structure to a polymeric dense liquid as during the transition both liquids coexist.

2.5.3 Al_2O_3-Y_2O_3

A LLT was found in the Al_2O_3-Y_2O_3 system over a wide compositional range. Through quenching from different temperatures, it was possible to quench-in different liquid phases with different density but with the same composition. The phase, which nucleated and grew at low temperature in the high temperature phase was found to have a lower density than the high temperature liquid phase. Therefore, the first order phase transition was suggested to be entropy-driven which automatically led to the idea of a higher ordered low density low temperature liquid in this oxide system [2]. In terms of the locally ordered structure model, this LLT cannot be explained by the single order parameter density. Apparently, the lower density in the low temperature phase must be due to the local ordering which lead to a lower energetic state.

2.5.4 Germanium and Tellurium

The existence of a LLT in Ge was already predicted in 1979 [132]. After the fabrication of partially amorphous Ge [133], it was possible to prove the existence of a LLT in Ge by the aid of electromagnetic undercooling experiments [134] and x-ray diffraction [135]. After producing completely amorphous Ge in a high-pressure diamond anvil cell (DAC) [106], the LLT could be proven as under high pressure a high density glassy phase is formed which transforms to a low density glassy phase during decompression. Te also exhibits a density anomaly in the supercooled liquid state (see Figure 2-18), which was associated to a LLT [136,137]. In different Te-Ge systems, this LLT could be shifted to different temperatures with respect to their T_l [138,139] and it was nicely shown, that the LLT, which exhibits changes in the medium-range, is associated to a fragile to strong transition upon cooling [4,83].

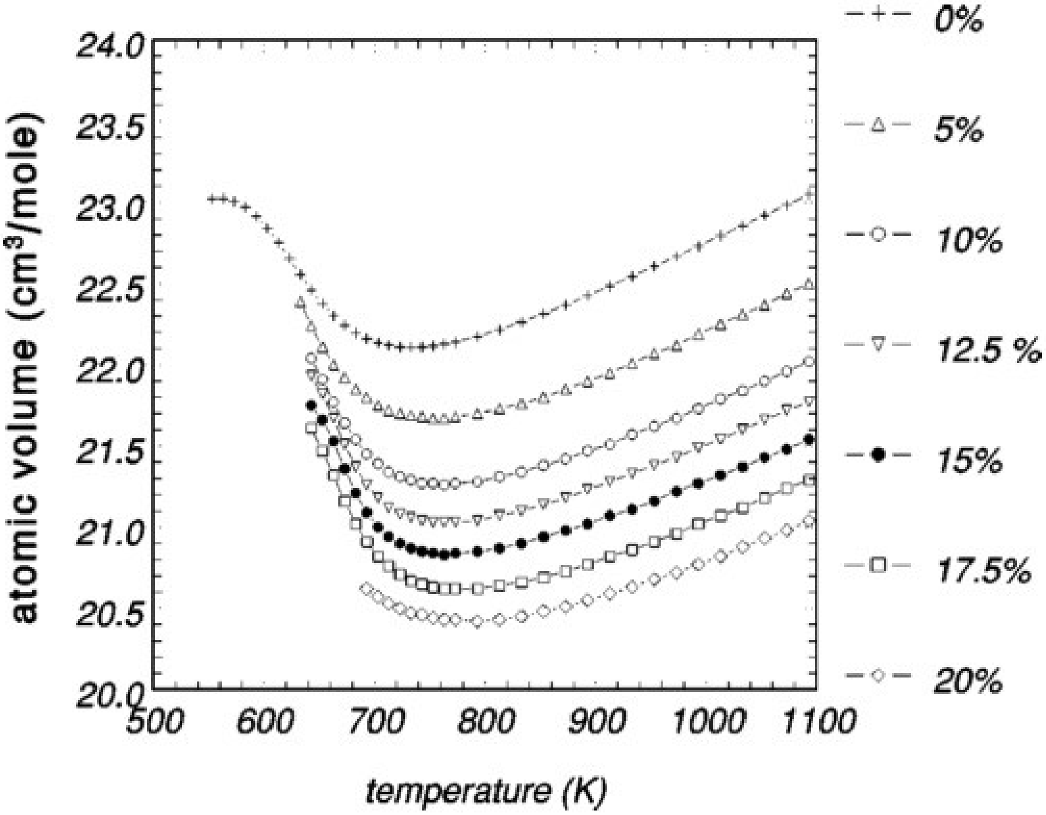

Figure 2-18: Volume minima (density maxima) measured in different $Ge_xTe_{(1-x)}$ alloys (Ge content is shown on the right). The Figure is reprinted from [138].

2.5.5 Water

Water is a liquid whose thermodynamics and structure are not yet understood. There are numberless publications based on experimental results and simulation, which try to explain the anomalies in the properties and structure of water, which have been reviewed recently by Gallo et al. [103]. Water seems to possess different kinds of structures in the supercooled liquid and glassy state depending on temperature and pressure (see Figure 2-19). At low temperatures and pressures a low-density, entropy stabilized liquid seems to be formed, whereas at high pressures a high-density liquid is stable. The experimental results fit very well to the phenomenological two state model of Tanaka.

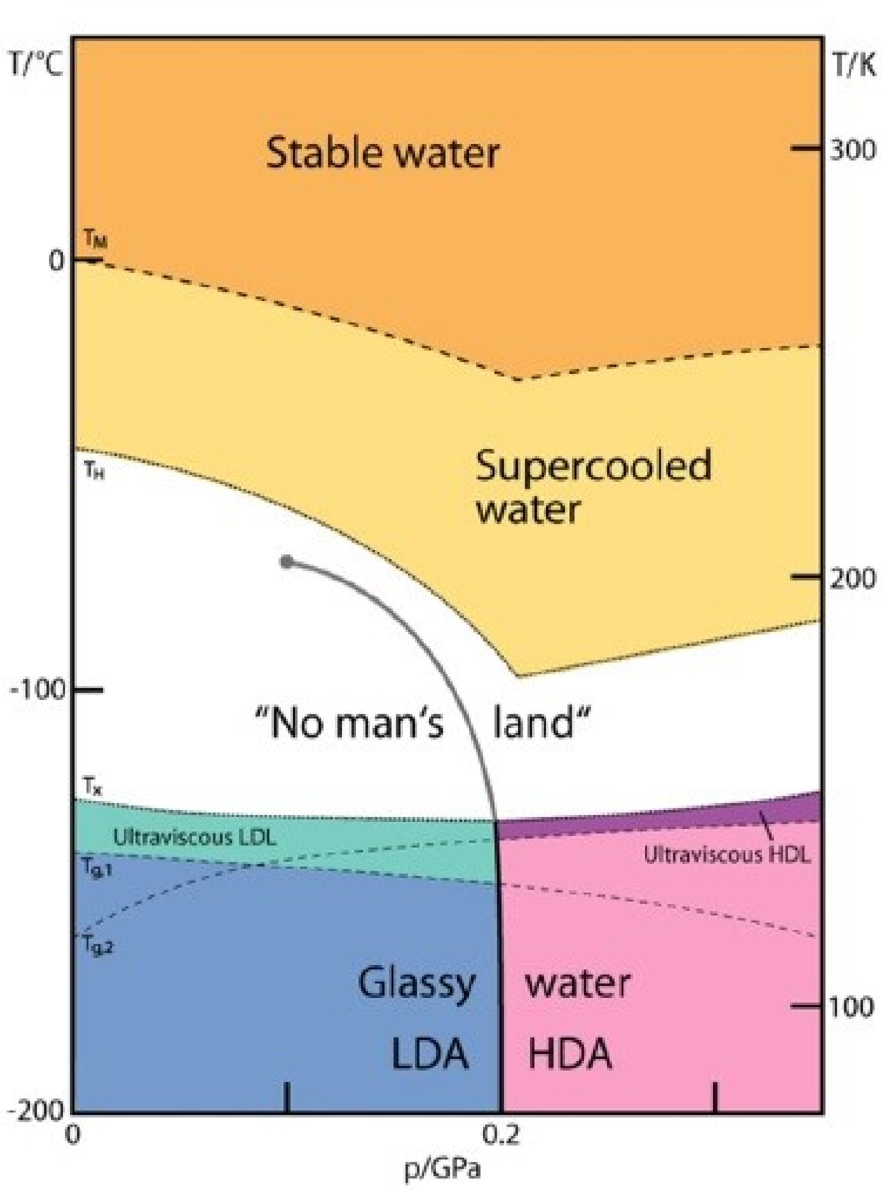

Figure 2-19: Phase diagram of water reprinted from [103]. Below the “No man’s land, where crystallization hinders the observation of the supercooled liquid, water appears to possess high- and low-density liquids (HDL/LDL) and glassy states (HDA/LDA).

2.5.6 Triphenyl Phosphite

In triphenyl phosphite (TPP) a glacial phase was found which did neither fit to the glassy phase of the liquid nor to a crystalline phase [140]. Later this glacial phase was identified as the glassy phase of a second liquid with the exact same composition [6,104,141]. In this case the LLT occurred in the glassy phase from a low density high temperature liquid to a high density low temperature liquid.

Although the density decreases upon cooling it was suggested that the low temperature liquid is more ordered and that the transition is entropically driven.

2.5.7 Bulk Metallic Glasses

There is a large variety of metallic glass-forming liquids. Metallic glasses appear to be very advantageous for the investigation of LLTs as they occur in different BMGs at very different temperatures. There are metallic glass-forming liquids, where the LLT occurs in the stable melt above T_l, some systems exhibit the LLT between T_g and T_l and there are systems in which it occurs around T_g or even below. There seems to be very similar behavior in terms of fragility above and below the LLT. Above, the liquids exhibit rather fragile behavior (see section 2.4.4) with D* around 10-12, below the liquids behave strongly with D* of around 20-25 [3,55,80,82,95,97]. Examples for LLT in different BMGs are described below.

The $La_{50}Al_{35}Ni_{15}$ metallic-glass-forming liquid exhibits a first-order phase transition in the stable liquid above the liquids temperature [142]. It was found that the nearest neighbor arrangement in the liquid change at T_{LLT}. Although the density seems unaffected, the order parameter L, which was introduced before, seems to become dominant over the density as the decisive order parameter. Consistently, the fragility of the system below the LLT is determined to be rather strong with a D* of about 21 (calculated from [143]). Due to the high T_{LLT} above T_l the energy gain of the local ordering and the cooperativity seems to be high in the La- based metallic glass-forming liquid.

In Vitreloy 1 ($Zr_{41.2}Ti_{13.8}Cu_{12.5}Ni_{10}Be_{22.5}$), a fragile-to-strong transition was found around the liquidus temperature T_l of the alloy [97]. Wei et al. [3] have shown that the fragile-to-strong transition is accompanied by structural changes in the liquid as a result of a first order LLT, which does not result in macroscopic density changes, but in the local structure of the liquid. Figure 2-20 shows the structural changes during the LLT upon cooling in the peak position of the first sharp diffraction peak (FSDP) of the S(Q). In Vitreloy 106a ($Zr_{58.5}Cu_{15.6}Ni_{12.8}Al_{10.3}Nb_{2.8}$), a LLT occurs

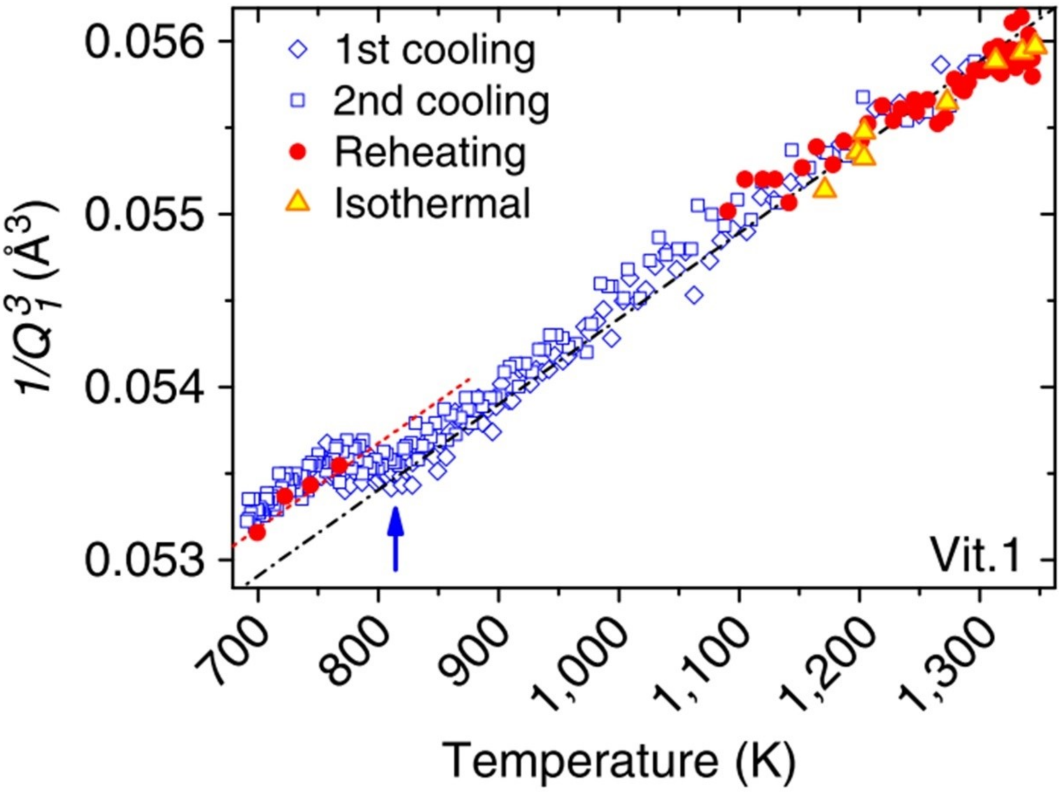

Figure 2-20: Position of the first sharp diffraction peak (FSDP) of the S(Q) as $(1/Q_1)^3$ as a function of temperature. Upon cooling (blue squares and diamonds) the LLT occurs at about 830 K, where a clear discontinuity is visible. The figure is reprinted from [3].

between T_l and T_g [82]. The authors show evidence for the transition from a high temperature less ordered liquid to an on the medium range more ordered low temperature liquid by using high resolution x-ray diffraction. Both Vitreloy alloys exhibit strong kinetic behavior at the glass transition and a LLT far above T_g.

The Pd-Ni-P system is one of the best metallic glass-forming systems with a high critical casting thickness [144–146]. The system exhibits an exothermic heat release above T_g, which was found in 1976 for the first time [147], but which could not be associated to decomposition or crystallization through different techniques [148–150]. In the $Pd_{41.25}Ni_{41.25}P_{17}$ system, the exothermic heat release above T_g is clearly visible and has been connected to the change in the local ordering of the liquid [151]. Above the critical temperature, the liquid is more disordered than below. The disordered liquid forms the glass below the T_{LLT}, which indicates a necessary undercooling for the transition indication a first order transition. The exothermic heat release is the result of the transition from the disordered to the ordered liquid. The low T_{LLT} implies a low energy gain through the local ordering and a small cooperative creation of the locally ordered clusters.

The $Au_{49}Cu_{26.9}Si_{16.3}Ag_{5.5}Pd_{2.3}$ alloy, which is investigated in this work is expected to behave similarly to the $Pd_{41.25}Ni_{41.25}P_{17}$ system. The thermodynamic anomalies are described in section 3.1 and the results of the investigation are shown in chapter 5. The alloy seems to undergo a LLT below T_g, with $T_{LLT} < T_g$ (1.5 K min^{-1}). It can only be revealed by quasi-static cooling of the liquid shifting T_g to lower temperatures to reach a condition in which $T_{LLT} > T_g$.

3 Material and Methods

3.1 The alloy

In 1960, the first metallic glass was produced in the binary Au-Si system [8]. This alloy required a cooling rate of 10^6 K s^{-1} and allowed the production of amorphous samples with a thickness of about 50 µm [10]. Except for some experiments in the Au-Ge-Si ternary system, which did not improve the glass-forming ability significantly [152,153], the Au-based alloys have not been under further investigation for 30 years. In that period, new glass forming alloys have been found in Pd-based [154–156], Pt-based [157], Zr-based [158,159] and other systems. In 2005, the casting thickness of alloys based on the Au-Si system was tremendously increased to 5mm through the development of the $Au_{49}Cu_{26.9}Si_{16.3}Ag_{5.5}Pd_{2.3}$ metallic glass forming alloy [10]. This alloy is investigated here.

3.1.1 Application and relevant properties

The $Au_{49}Cu_{26.9}Si_{16.3}Ag_{5.5}Pd_{2.3}$ alloy has several advantageous properties, which make an application especially in the field of jewelry possible. At first, the alloy is a 18- carat gold alloy containing more than 75 wt% gold. Furthermore, the alloy exhibits a very good processability due to the low glass transition (T_g ~ 400 K) and liquidus temperature (T ~ 644 K) [10,160,161]. It can easily be melted inductively and cast into copper molds to produce amorphous specimens. A further shaping using thermoplastic forming is possible due to the large supercooled liquid region of 58 K at temperatures which are accessible in a standard kitchen oven [10,162]. When polished after processing, the alloy exhibits a premium white color, which is the best white gold color on the jewelry market [163–166]. The amorphous structure of the Au-based alloy results in a hardness of about 360 HV1, which is almost twice as high as the hardness of crystalline Au-based alloys [10].

3.1.2 Tarnishing behavior

The $Au_{49}Cu_{26.9}Si_{16.3}Ag_{5.5}Pd_{2.3}$ at% alloy exhibits very interesting properties as explained in the previous sections. The main drawback is the tarnishing behavior of the alloy. Parts made of this alloy start to change their color starting from one of the best white gold colors after polishing the as-cast samples to yellow and brown colors within a short period of time depending on the environment. This tarnishing hinders an application in jewelry despite its good castability, processability, high hardness, high gold content and white gold premium color after polishing. The polishing removes the SiO_2 casting skin from the surface of the sample. New SiO_2 is built on the surface together with elemental Cu, which starts to diffuse through the SiO_2 layer and forms Cu_2O and Cu_2S. The SiO_2 formation is favored by the presence of Cu in the alloy. From the surface, SiO_2 dendrites grow into the bulk material and cause further corrosion. The main reason for the fast tarnishing behavior is the presence of Si and Cu in the alloy. The corrosion mechanism is shown in Figure 3-1.

(a) As cast (b) Polished surface (c) Cu triggered formation of SiO_2

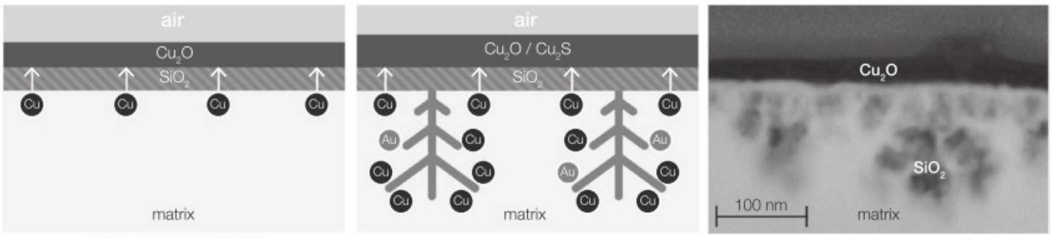

(d) Out diffusion of Cu formation of Cu_2O (e) Growth of SiO_2 and Cu_2O (f) STEM image of the tarnishing layer in cross section

Figure 3-1: Oxidation mechanism of the $Au_{49}Cu_{26.9}Si_{16.3}Ag_{5.5}Pd_{2.3}$ alloy. The removal of the SiO_2 cast skin leads to fast formation of SiO_2, Cu_2O and Cu_2S at the surface, which causes the fast change in color. The figure is reprinted from [164].

The tarnishing behavior, its reasons and possible solutions have been investigated by Miriam Eisenbart [164–166]. Further development has been done to reduce the copper and silicon content of the alloy in order to slow down the tarnishing. The substitution of copper with gallium improved the tarnishing behavior as it forms a grey oxide instead of the brownish and reddish corrosion products of copper [161,167]. Although the modification with gallium improved the tarnishing behavior, the alloy is still not stable enough for applications.

3.1.3 Motivation of the work

Apart from the relevant properties for application described in section 3.1.1, the alloy exhibits unusual kinetic and thermodynamic behavior, which is described in this section. The explanation of this behavior is the main motivation of this work.

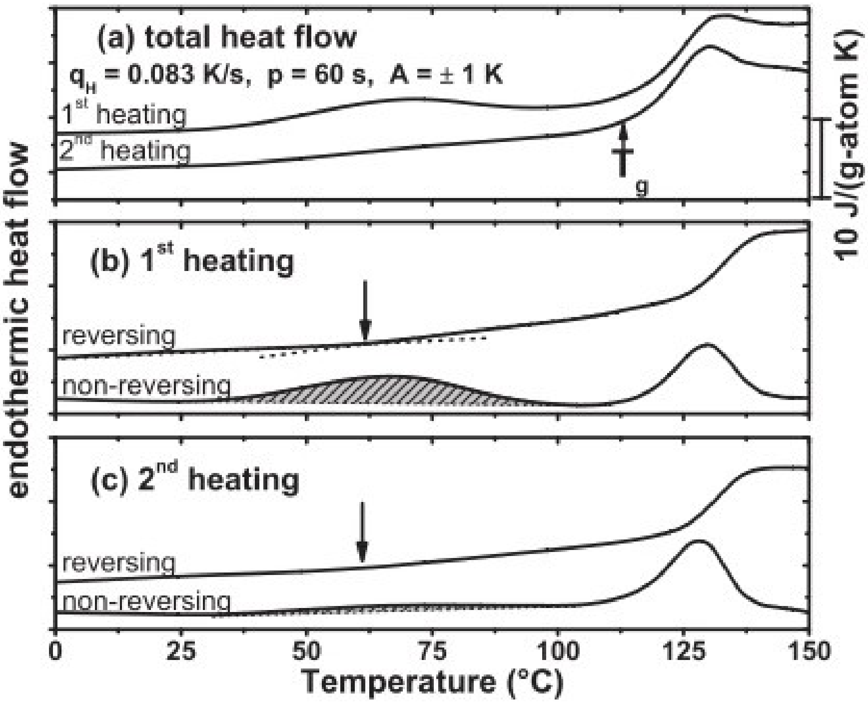

Figure 3-2: Endothermic heat flow of the $Au_{49}Cu_{26.9}Si_{16.3}Ag_{5.5}Pd_{2.3}$ alloy measured in DSC. The material exhibits a pronounced pre-peak which is non-reversing upon heating the as-cast material. The figure is reprinted from [168].

Evenson et al. [168] measured pronounced recovery of the β relaxation at about 330 K and associated this to low temperature aging far below the glass transition (see Figure 3-2). This aging does not seem to change the free volume content of the alloy but changes the chemical order on length scales of about 3 Å [169].

Louzguine-Luzgin et al. [170] found a double step-like, reversible glass transition phenomenon (see Figure 3-3), which starts at the same temperature at which the β relaxation was found during the MDSC and DMA measurements from Evenson et al. [168]. The step-like behavior observed during the glass transition of the $Au_{49}Cu_{26.9}Si_{16.3}Ag_{5.5}Pd_{2.3}$ alloy is qualitatively comparable to a combined glass transition and crossing the Widom line as seen in Jagla model simulation [130].

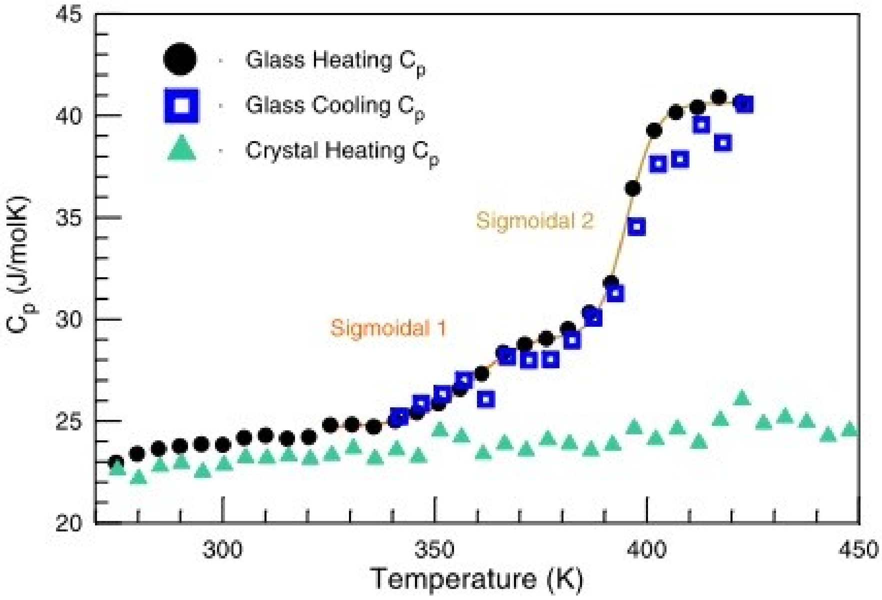

Figure 3-3: Heat capacity measurement of the $Au_{49}Cu_{26.9}Si_{16.3}Ag_{5.5}Pd_{2.3}$ alloy. In this measurement a distinct step in the glass transition upon heating and cooling is visible. The figure is reprinted from [170].

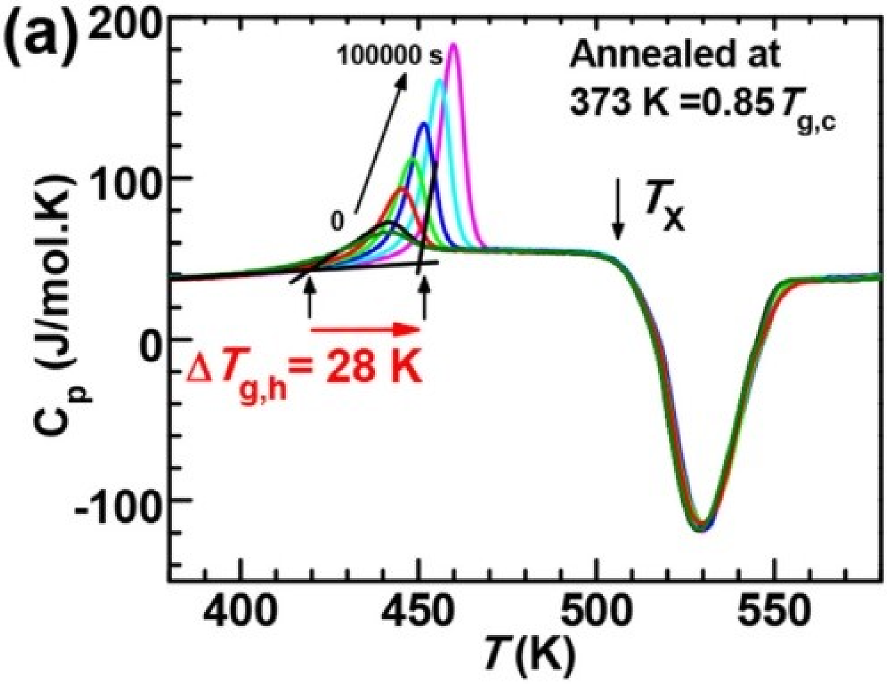

Figure 3-4: Glass transition and endothermic overshoot due to enthalpy recovery after different annealing times at 373 K. The $Au_{49}Cu_{26.9}Si_{16.3}Ag_{5.5}Pd_{2.3}$ alloy shows an marked increase in the glass transition temperature of 28 K. The figure is reprinted from [171].

Wang et al. performed an extensive flash calorimetry study [171]. They determined the critical cooling rate of the alloy to be approximately 1000 K s^{-1}. Interestingly, they were able to increase the glass transition temperature by 28 K through annealing the alloy at 373 K, below its glass transition temperature, which is an anomalously high change of T_g (see Figure 3-4).

To unveil the origin of these different observations, an extensive study of the thermodynamic, kinetic and structural properties of the $Au_{49}Cu_{26.9}Si_{16.3}Ag_{5.5}Pd_{2.3}$ alloy has been performed, which is the heart of this scientific work.

3.1.4 Sample preparation

The bulk samples were produced starting from the raw elements with purities higher than 99.995%. The correct composition was inductively melted and homogenized at approximately 1400 K in an alumina crucible in the Indutherm MC15 tilt caster under argon protective atmosphere. The elements were stacked in the crucible in the order Pd, Ag, Au, Cu, Si to avoid the formation of Pd-silicide during the melting process. After the homogenization, the samples were cast into watercooled copper moulds to achieve the required high cooling rates to avoid the crystallization of the samples.

To produce metallic ribbons the alloy was heated inductively in a silica glass tube and cast under argon atmosphere on a melt spinning copper wheel. Ribbons with thicknesses between 5 and 70µm were produced. All samples were analyzed using XRD to confirm their amorphous structure. The ribbons were then used for the investigation of the dynamics and the structure during the synchrotron measurements.

3.2 Synchrotron Radiation

Electrons, which travel with a speed close to the speed of light emit synchrotron radiation when they a forced on curved trajectories [172]. After the observation of radiation emitted by electrons from the first electron synchrotron in 1947, the radiation was at first seen as a problem of energy loss in high energy particle accelerators [172]. But today it is used for the investigation of matter and physical phenomena in about 60 synchrotron radiation facilities all over the world [173].

Synchrotron radiation facilities like the European Synchrotron Radiation Facility (ESRF) in Grenoble, France, and the Deutsches Elektronensynchrotron (DESY) in Hamburg, Germany, consist of a linear accelerator (linac), a booster ring and storage ring, at which the beam lines are attached and the radiation for their experiment is provided. Figure 3-5 schematically shows the setup of a synchrotron. In linac and booster, the electrons are accelerated to reach energies in the order of MeV or even GeV to be “stored” in the storage ring where they cycle to provide the radiation for the beam lines.

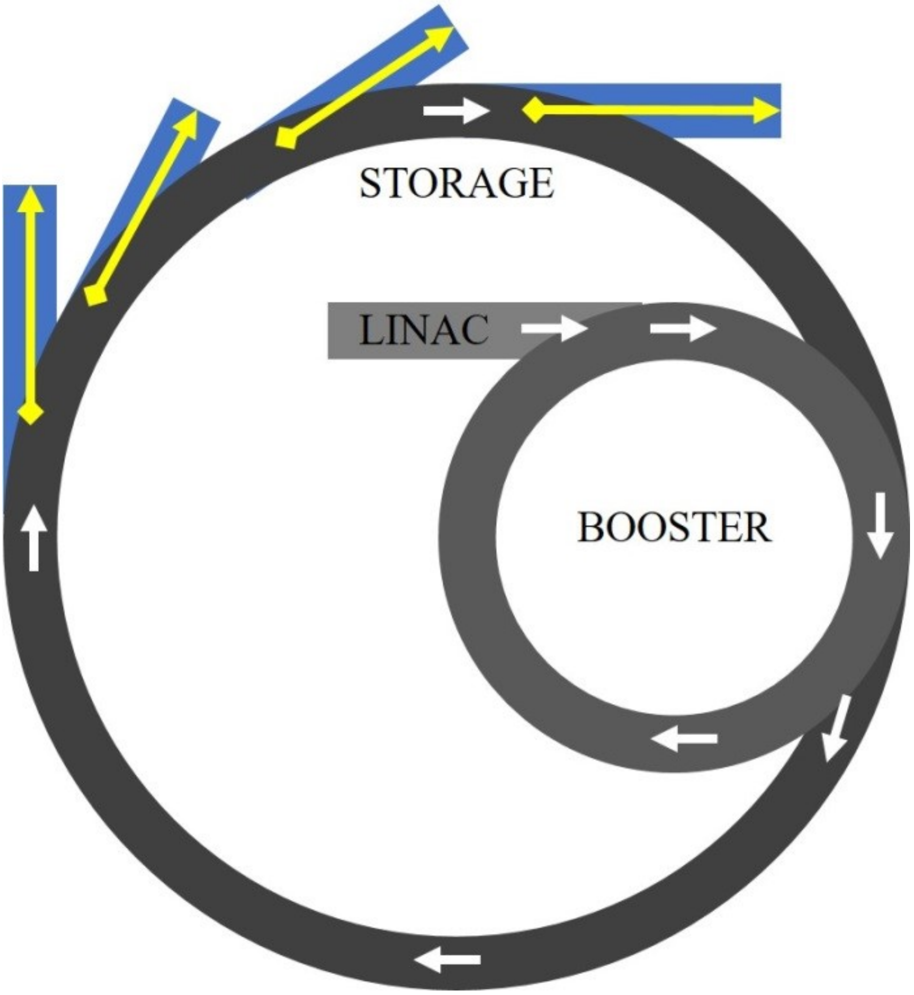

Figure 3-5: Schematic setup of a synchrotron. The electrons (white arrows) are accelerated in linac and booster and then injected into the storage ring to provide the beamlines (blue) with radiation (yellow arrow).

The properties of synchrotron radiation are very different compared to standard laboratory X-ray tubes. For example, the photon flux is about 10^6 to 10^{10} times higher than in conventional X-ray tubes [173], which makes it possible to perform a X-ray diffraction experiment with the same data quality in one second at a synchrotron facility, which would take between a day and a year in a laboratory diffractometer. The most important properties of a synchrotron are high intensity, broad spectral range from infrared to hard X-rays, natural narrow angular collimation, high degree of polarization, high brightness and high beam stability [172]. Very important are the emittance of the electron beam and the brilliance of the resulting X-rays. Those two properties limit the quality of the X-rays and therefor the resolution of the different experimental setups, which use the radiation.

3.2.1 X-ray Photon Correlation Spectroscopy (XPCS)

X-ray photon correlation spectroscopy (XPCS) is a synchrotron-based technique for the investigation of translational atomic dynamics. The function principle is the same as for dynamic light scattering (DLS), where highly coherent monochromatic laser light is used to investigate the dynamics of e.g. colloidal gels [174–176]. In 1991, Sutton et al. [177] showed that very brilliant X-ray sources provide the possibility of X-ray photon correlation spectroscopy, and defined very precisely the requirements for such a technique. The difference to DLS is the probing radiation. In DLS highly spatial (transversal) and temporal (longitudinal) coherent laser light is used with wavelength in the range of visible light (~400-700nm). For XPCS partially coherent monochromatic X-rays with an energy of 8 keV (~0.155nm) are used. As the wavelength of the X-rays is in the order of the atomic diameter, it is possible to investigate atomic motion in ordered and amorphous materials on the atomic scale [178–182], whereas DLS can be used to investigate the dynamics in colloidal suspensions, e.g. [174,183]. Today, XPCS is available at third generation synchrotron sources like the European Synchrotron Radiation Facility (ESRF) in Grenoble, where the challenge is to create a partially coherent x-ray beam from the chaotic synchrotron light source.

Basics

When matter is illuminated by radiation, the radiation, which should exhibit wavelength in the size of the interatomic distances, interacts with the atoms/particles in the material, which can be dealt with as secondary sources of radiation. The atomic arrangement and interaction of the atoms in the material determine the angular distribution of the scattered radiation [184]. This is the reason why we can learn a lot from diffraction experiments at synchrotron facilities as the wavelength of the radiation is comparable to the interatomic distances in matter.

Using a chaotic source such as a synchrotron, scattering waves are averaged and give general information about the average interatomic distances and arrangements, which is already a very valuable information and crucial for the understanding of the structure of materials. For the measurement of translational atomic motion in matter, a chaotic source is not suitable. To probe temporal changes, knowledge of the exact spatial arrangement in the illuminated volume is necessary, which can only be achieved by use of coherent radiation [177]. When coherent radiation is used a grainy diffraction pattern, which changes with time, can be detected. This grainy pattern appears, when randomly distributed regions introduce phase shifts into the scattering of coherent radiation [177]. Such a grainy pattern has first been seen in diffraction experiments with laser light.

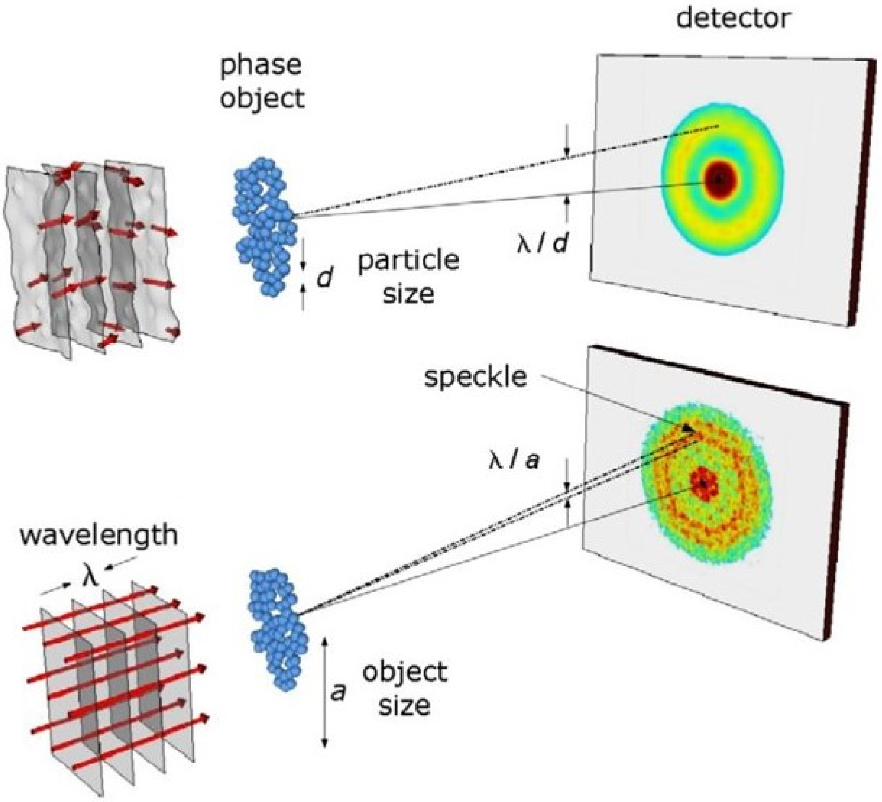

Figure 3-6: Difference of the diffraction pattern of an amorphous sample between incoherent (above) and coherent (below) light. Incoherent light leads to the "normal" diffraction pattern of an amorphous sample. Coherent light leads to a grainy speckle pattern on top of the diffraction pattern that changes with time due to the changing arrangement of different areas in the sample [185,186].

Figure 3-6 shows the differences in the diffraction pattern using coherent and incoherent light. The intensity fluctuation in the grainy pattern are called speckles. The speckles are a result of the exact spatial distribution of the atoms in the material. As the spatial distribution changes over time due to atomic motion, the speckle pattern changes. These temporal changes can be used to determine the atomic dynamics.

The generation of coherent radiation from a chaotic synchrotron source and the determination of the dynamics from speckles pattern are explained in the following sections.

Coherent light from a chaotic source

To get partially coherent X-rays which create a speckle pattern when irradiating an inhomogeneous material some requirements must be fulfilled.

At first, the beam must be monochromatic with a small spectral bandwidth. The wavelength λ of the radiation and the spectral bandwidth of the wavelength Δλ/λ determine the longitudinal/temporal coherence length $c_l = \frac{\lambda}{2\cdot(^{\Delta\lambda}/_{\lambda})}$. c_l is the length, at which a wave with wavelength λ and a wave with wave length λ+Δλ, which propagate from the same source show complete negative interference. The spectral bandwidth describes the deviation from the average wavelength. For XPCS at the ESRF a wavelength of approximately 0.155nm (8 keV) is used. To reach a small spectral bandwidth a silicon single crystal is used as monochromator. The beam is reflected from the (111) plane of the single crystal which gives a spectral bandwidth of $\Delta\lambda/\lambda = 1.4\text{x}10^{-4}$ [177,187].

In addition to the longitudinal coherence length, the spatial/transversal coherence length is important. A perfect point source would have a perfect transversal coherence. In the case of a synchrotron source this means, that the source size determines the transversal coherence length. The larger the source the smaller is the transversal coherence length. The transversal coherence length can differ in horizontal and vertical direction with $c_{h,v} = \frac{\lambda\cdot D}{h\cdot v}$, where λ is the wavelength, D is the distance from the source and h and v are the horizontal and vertical source size.

The three coherence lengths span the coherence volume, which should be in the same size as the investigated sample size [185,187–189]. If the sample volume is as large as the coherence volume, the coherent flux is $I_c \approx B \cdot \lambda^2 \cdot \frac{\Delta\lambda}{\lambda}$, where B is the brilliance of the source, λ is the wavelength and Δλ/λ is the spectral bandwidth [185]. This is the reason why an extremely brilliant source is required to be able to perform coherence experiments when the source is chaotic [187]. The brilliance is defined as "the photons per second emitted in a given solid angle in a given bandwidth per source area"[187].

Beamline setup

The beamline setup of ID 10 at the ESRF is shown schematically in Figure 3-7. The main hardware components are undulators, slits, monochromators and beam shutters. The undulators deliver radiation of 8 keV. The slits are used to create transversal coherence and the monochromator generates a beam with sufficient longitudinal coherence. To block the beam when persons work in the experimental hutch beam shutters are installed at several positions in the setup.

"The XPCS experiments have been performed using a partially coherent X-ray beam at 8 keV impinging on a 10 µm thick as-spun ribbon in transmission geometry. The incoming beam, 10x8 µm (HxV), had a flux of ~10^{11} ph s^{-1} at the working energy. Series of speckle patterns were recorded by an Andor Ikon M detector (13 µm pixel size) placed ~70 cm downstream the sample with an exposure time of 3 s per image. The detector dead time was 1.7 s." [PRL]

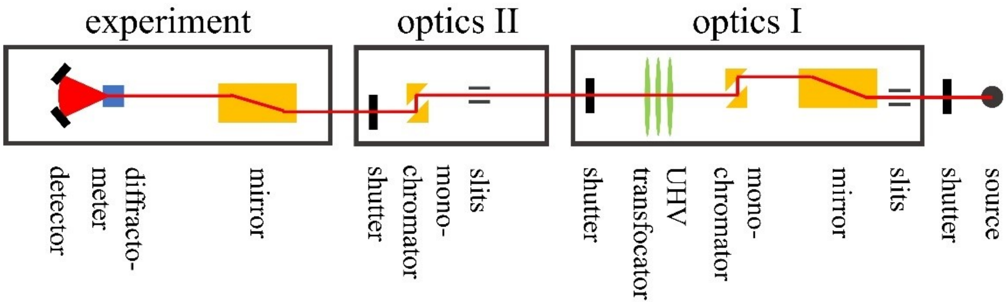

Figure 3-7: Schematic of the ID 10 beamline at the ESRF. The properties of the beam are adjusted using slits, mirrors, monochromators and transfocators. The shutters are installed to be able to cut the beam at several positions. The scheme has been adapted from [190].

Data Collection and Analysis

The detector is placed on the first sharp diffraction peak (FSDP) as it reflects the average next neighbor distance and the scattered intensity is the highest at this scattering angle. At this position, series of speckle patterns are recorded with a CCD camera with an acquisition time of 3 s per image in isothermal conditions. The detector dead time and readout time are 1.7 s. Figure 3-8 shows such a series of patterns. The collected speckle patterns are then correlated. At first, the two-times correlation function (TTCF) $G(Q, t_1, t_2) = \frac{<I(Q,t_1) \cdot I(Q,t_2)>_p}{<I(Q,t_1)>_p \cdot <I(Q,t_2)>_p}$, where I is the intensity, $<\ldots>_p$ the ensemble average over all detector pixels, Q the wave vector and t_1 and t_2 two points in time can be determined [187]. The result of such a correlation of all patterns is the TTCF, which is a correlation map on which all patterns are correlated with each other.

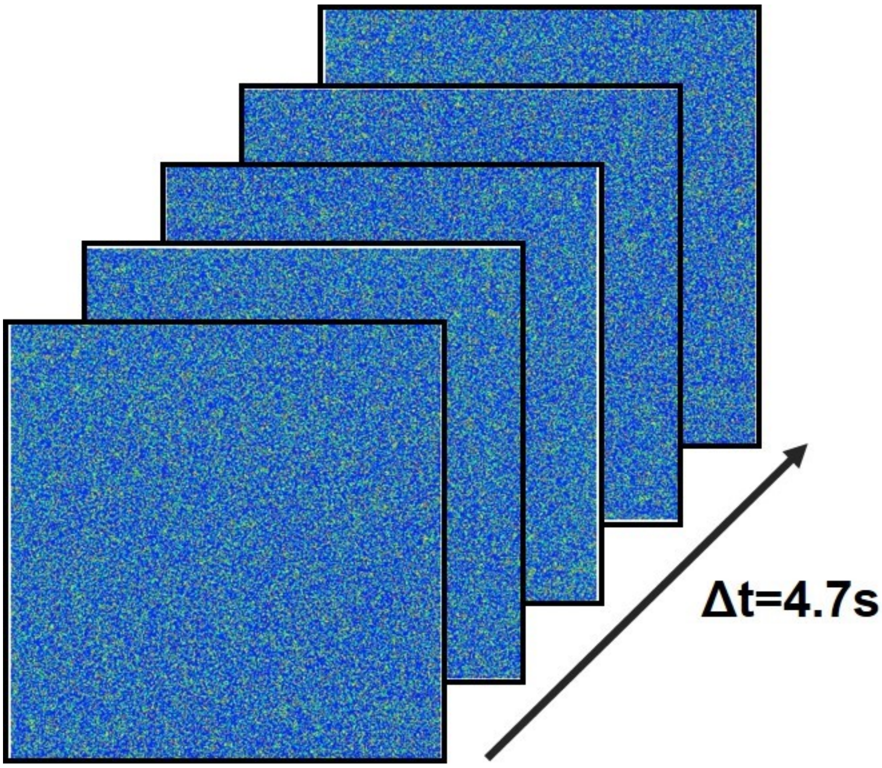

Figure 3-8: Series of speckle patterns which are recorded during a XPCS measurement. The lack time between the images is 4.7 s, which includes acquisition time, detector dead time and read out time.

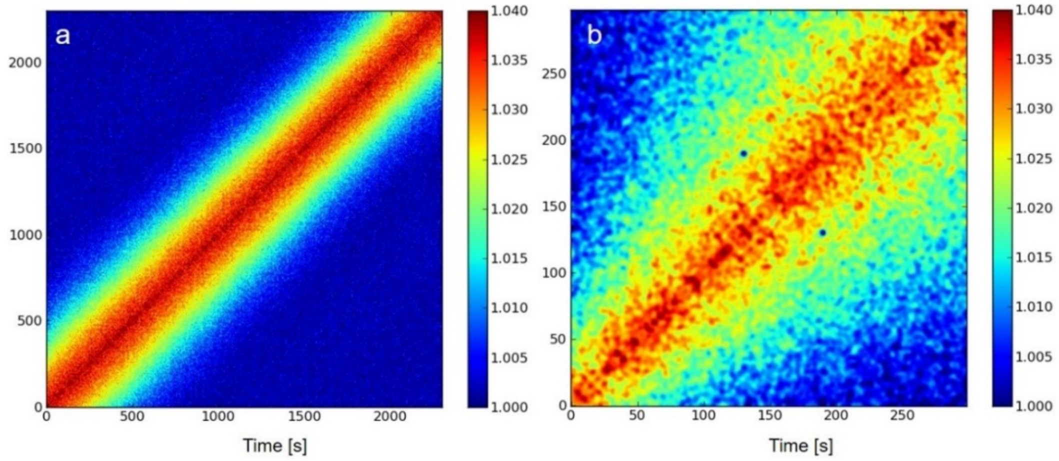

Figure 3-9: (a) TTCF with constant width indicating stationary dynamical behavior. (b) TTCF with broadening of the diagonal indicating aging.

Figure 3-9 shows 2 different TTCFs. In those images, the elapsed time is represented by the diagonal, where each pattern is correlated with itself. The correlation is the highest there. Leaving the diagonal, every pattern is correlated with the following and the correlation decreases until it is completely gone. The width of the reddish line in the TTCF contains two important information. Firstly, it contains information about the nature of the dynamics in the system. If the width of the line does not broaden with experimental time, the dynamics is stationary as shown in Figure 3-9a. If the line broadens, the dynamics slows down with time, and the sample ages (see Figure 3-9b). Secondly, the width of the line is proportional to the structural relaxation time of the system. The broader it is the slower the dynamics is in the system. To quantify the structural relaxation time, the temporal average of G (Q, t_1, t_2) is taken. Figure 3-10 shows a TTCF and the corresponding intensity autocorrelation function $g_2(Q,t) = \frac{<<I_p(Q,t_1)\cdot I_p(Q,t_1+t)>_p>}{\ll I(Q,t_1)>_p>\cdot \ll I(Q,t_1)>_p>}$, where Q, t_1, t_2, $<\ldots>_p$ are as defined above and <….> is the temporal average. It can be correlated to the intermediate scattering function F(Q,t) via the Siegert relation $g_2(Q,t) = 1 + C(Q)\cdot|F(Q,t)|^2$, where C(Q) is a setup specific value. The F(Q,t) can be fitted with a Kohlrausch-Williams-Watts (KWW) stretched exponential function: $\mathrm{F}(Q,\mathrm{t}) = \mathrm{F_Q}\cdot\exp(-\frac{\mathrm{t}}{\tau_\mathrm{Q}})^{\beta_\mathrm{Q}}$, where F_Q is a constant, τ_Q is the structural relaxation time at given Q and β_Q.

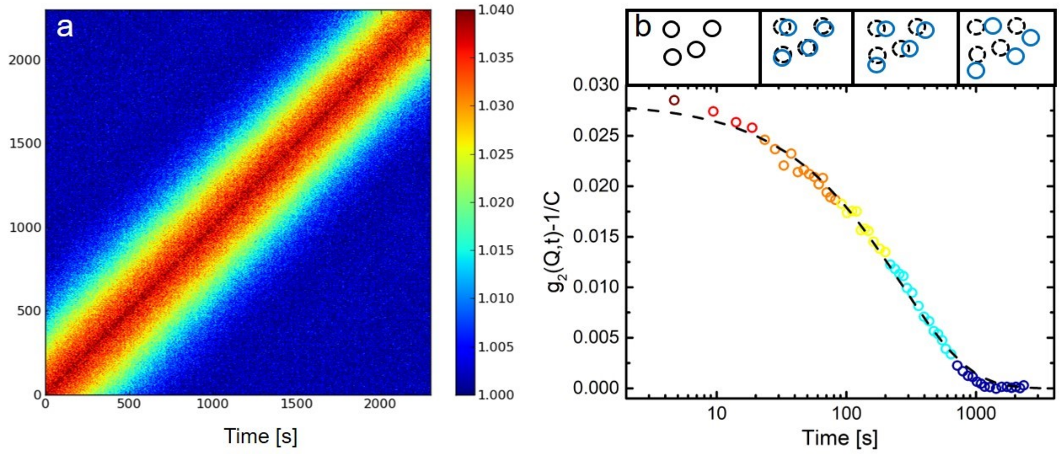

Figure 3-10: TTCF (a) and the corresponding $g_2(Q,t)$ (b). The correlation is completely lost, when the atoms have moved one atomic diameter.

By using an area detector the Siegert relation can be extended to non-ergodic systems [183,191,192]. Therefore, XPCS is usable in glassy systems, where the ergodicity breaks down.

Figure 3-11 shows two different g_2 functions. The structural relaxation time τ_Q and the shape parameter β_Q are determined from fitting the KWW equation to the experimental data. τ_Q is the time where the decay has reached 13.5% of the start value which is $\tau = C \times e^{-2}$, where C is the contrast and e is Euler's number. β_Q describes the shape of the decay. Compressed values larger than one are found in glasses and lead to the steep decay of g_2, whereas stretched values smaller than 1 are characteristic for liquids and lead to a smooth decay. Figure 3-11 illustrates this difference in β_Q for glasses (a) and liquids (b).

The TTCF and the intensity autocorrelation function are used to characterize the dynamics in a system. From the TTCF, the nature of the dynamics (stationary behavior or aging) is identified and from the fit the KWW stretched exponential function to the decay of g_2, the structural relaxation time τ_Q as well as the shape parameter β_Q are determined.

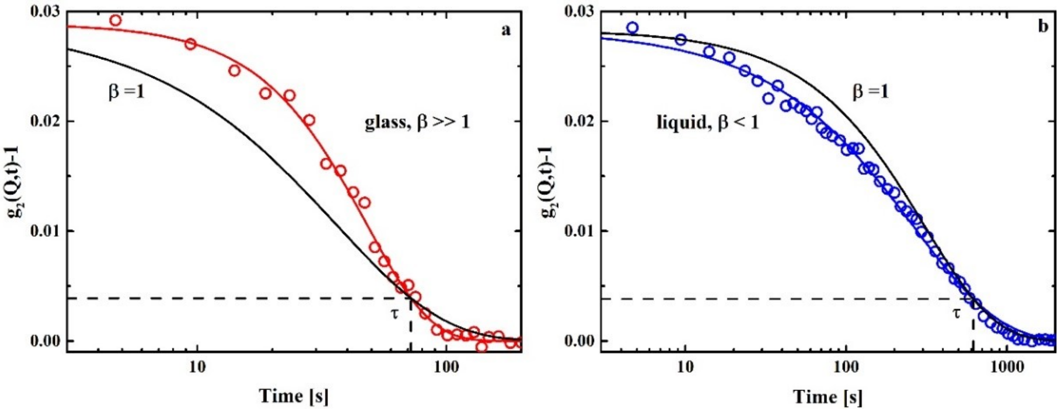

Figure 3-11: $g_2(Q,t)$ for a glass (a) and a liquid (b). τ is reached when the contrast has dropped to 13.5% of the start value. β describes the shape of the curve. It is compressed (β >> 1) in glasses (a) and stretched (β < 1) in liquids (b).

The accessible relaxation time range is limited by the beam properties and the quality of the detector. To reach a sufficient signal-to-noise ratio the data acquiring time is about 3 s. The detector deadtime and readout time are also in the order of seconds. Therefore, relaxation times of about 10 s are the lower limit for XPCS for the existing setup. The upper limit is restricted by the measurement time. Therefore, the accessible relaxation time range is about 10s -10,000 s.

Dynamic susceptibility

XPCS is capable to measure dynamical heterogeneities by calculating the dynamic susceptibility χ_T (Q,t), which corresponds to the normalized variance of the TTCFs calculated along lines parallel to the main diagonal [37,38]. This quantity gives information on temporal heterogeneities in the system and can be related to the spatial heterogeneities described by the four point dynamic susceptibility χ_4 [39–43]. Due to the strong scattering signal necessary for calculating χ_T (Q,t), dynamical heterogeneities are usually studied by dynamic light scattering (DLS) only for complex systems whose relevant dynamics occurs at the nanometric scale, i.e. where the signal in photon correlation experiments is intense [38,193–197]. In the present system the signal-to-noise ratio at the maximum of the *S(Q)* allows to study the dynamical heterogeneities at the atomic level in the deeply supercooled liquid state at 385.5 K [198].

Q-dependence of relaxation time

As described before, the detector is normally placed on the maximum of the FSDP to determine the relaxation time of the average atomic next neighbor distance. But it is known from coherent neutron scattering experiments and simulations that the investigation of the Q- range around the FSDP contains information about the collective atomic motion, e.g. [199–203]. De Gennes [199] described the fact that the measured average relaxation time at the first sharp diffraction peak (FSDP) of the static structure factor S(Q) exhibits a maximum, and the relaxation time spectrum shows a sharpening from a broader Gaussian distribution to a sharper one, which even changes its shape towards a Lorentzian distribution. He reasoned this from general considerations and first results from neutron scattering experiments. This "De Gennes narrowing" has been observed in liquid metals above their melting point, e.g. in references [201,204–206], in molecular liquids, e.g. in references [207–209], oxidic liquids, e.g. in references [180,210–212] and polymers, e.g. in references [213–215].

To investigate the Q dependence of the relaxation time and the shape parameter β in the supercooled liquid, the detector has been moved to eight different Q values around the FSDP at 385.5 K and the TTCF as well as the intensity auto-correlation function have been recorded.

3.2.2 X ray diffraction (XRD)

X-ray diffraction is a technique to resolve the atomic structure of a material. The scattered intensity of the incident beam from the sample is measured as a function of the wave vector, which is $Q = \frac{4\times\pi\times\sin(\theta)}{\lambda}$. Here, θ is the scattering angle between incoming and scattered beam. The intensity distribution over the Q-range contains the information about the structure of the material. Therefore, a 2D detector is placed downstream of the sample, perpendicular to the incident beam to collect the scattered intensity on a wide Q-range. In order to receive the total scattering structure function S(Q), the scattered intensity must be corrected for absorption, multiple scattering, Compton scattering, and polarization [216]. When the S(Q) is determined it contains all structural information of the sample. It is the Fourier transform of all the pair distribution functions of the constituent elements. But as the $Au_{49}Cu_{26.9}Si_{16.3}Ag_{5.5}Pd_{2.3}$ alloy consists of five elements, the large amount of pair distribution functions makes a transformation into real space questionable as no quantitative structural information can be extracted. But already from the S(Q) structural changes can be observed qualitatively, when looking at the first sharp diffraction peak (FSDP) and the change of its position in Q, e.g. [3,4,82].

Beamline Setup

The beamline setup of P02.1 at DESY is shown schematically in Figure 3-12. The setup of beamline ID11 at the ESRF is similar. The detector at both beamlines is a 2D detector, which is placed perpendicular to the incident beam close to the sample to record the entire diffraction pattern over a broad Q- range.

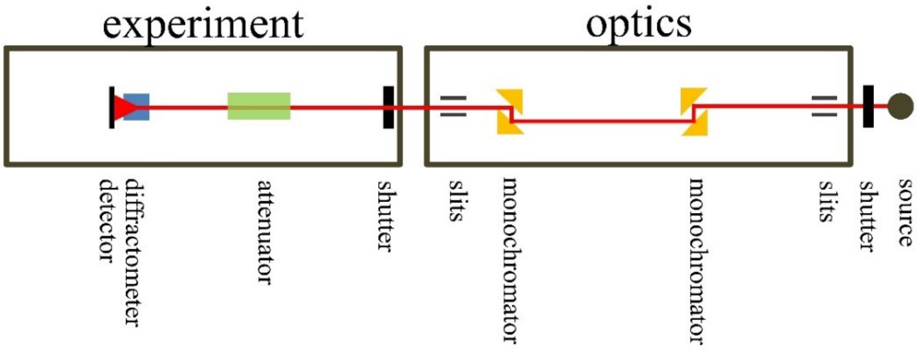

Figure 3-12: Schematic of the beamline setup of P02.1 at DESY. The incoming beam is focused using slits and the beam energy of 60 keV is adjusted using two monochromators. To regulate the flux of the beam, attenuators of different absorption can be moved into the beam path before illuminating the sample whose diffraction pattern is detected using a 2D detector.

Data collection and Analysis

XRD data were collected at ESRF as well as at DESY. At the ESRF, XRD data were collected at the beamline ID11 by using an incident monochromatic beam of 80 keV. The spectra were measured with the FReLoN 2D CCD camera at ~11.5 cm distance from the sample, which was kept in the same furnace used for the XPCS measurements. The samples investigated at DESY close to the glass transition were measured under a constant flux of high-purity argon in a Linkham THMS 600 furnace at the beamline P02.1 at DESY with a 60 keV beam. The data were acquired using a Perkin Elmer (XRD1621) CsI bonded amorphous silicon area detector (2048 pixels × 2048 pixels) at ~30.3 cm from the sample with a diameter of 5 mm and a thickness of approximately 200 µm. The high temperature measurements were performed at P02.1 at DESY under the same conditions using samples with a diameter of about 700 µm placed in a silica tube with a diameter of 1 mm and a wall thickness of 0.01 mm. The samples were heated above the liquidus temperature using a lamp furnace.

The intensity distribution I(Q) was integrated from the dark subtracted detector pattern and was corrected by background, sample absorption, fluorescence and inelastic (Compton) scattering and using the PDFgetX versions 2 and 3 [REF] to determine the static structure factor S(Q). The first sharp diffraction peak in the S(Q) was fitted with a k-spline fit. Figure 3-13 shows the way the fit was done. The data around the FSDP above a value of 1 were considered. From the fit, the peak position (Q_1^{max}) as well as the full width at half maximum (FWHM, Γ) were determined.

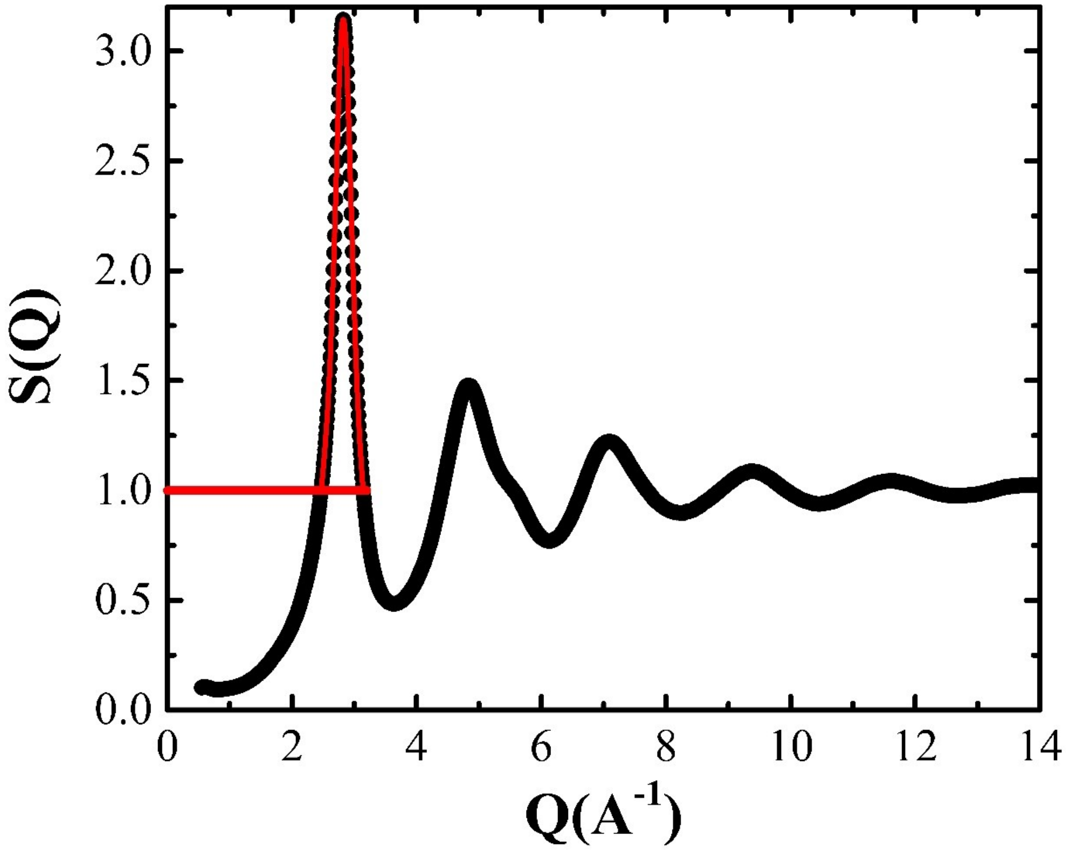

Figure 3-13: The FSDP of S(Q) is fitted with a k-spline function above a value of 1 (red line). From the k-spline function the peak position as well as FWHM are determined.

3.3 Differential Scanning Calorimetry (DSC)

Calorimetry is the measurement of the heat released or absorbed during physical changes and reactions. Calorimetry does not measure the absolute heat of a sample Q, but changes in Q with temperature. Note that the Q mentioned here is not the wave vector, but the heat content of the sample.

The DSC measurements were performed in a Perkin Elmer power-compensated DSC 8500. Power-compensated DSCs consist of two separate furnaces, one for the sample, one for the reference. During the measurement, the temperature in both furnaces is kept constant, which requires a power compensation. The heat flow of the sample is given by

$$\dot{Q} = \frac{dQ}{dt} = mc_p \frac{dT}{dt}$$

where $\dot{Q}$ is the heat flow, m is the mass and c_p is the specific heat capacity [30].

In order to achieve higher heating and cooling rates, a flash calorimeter was used. The Mettler Toledo Flash DSC 1 is a power compensated calorimeter and can reach rates of 4,000 K s^{-1} in cooling and 40,000 K s^{-1} upon heating. This is achieved through very small sample sizes in the range of nano- to microgram [171,217,218] and a direct contact of the sample with the chip sensor which is directly heated. Therefore, the sample is heated and cooled very homogeneously, and the low heat capacity of the systems allow high heating and cooling rates. The temperature range, in which the calorimeter can measure is 178 K to 723 K.

This temperature range makes is possible to melt the $Au_{49}Cu_{26.9}Si_{16.3}Ag_{5.5}Pd_{2.3}$ alloy on the chip and vitrify it as the critical cooling rate of the alloy is determined as 1000 K s^{-1} [171] and therefore significantly lower than the possible cooling rates.

3.3.1 Enthalpy recovery

The enthalpy recovery is a measurement method to determine the enthalpic state of a sample with respect to a standard treated, unaged one [219]. Through aging below T_g a sample reaches lower enthalpic states as indicated in Figure 3-14a. The longer a sample is aged, the deeper the enthalpic state, in which the sample is if the equilibrium is not reached. The relative position of the enthalpic state with respect to the unaged sample is determined from the enthalpy, which is recovered when the sample is heated back into the SCL. The higher enthalpy gain of the relaxed sample during heating into the SCL is shown in Figure 3-14b. The marked area corresponds to the enthalpy difference in Figure 3-14a.

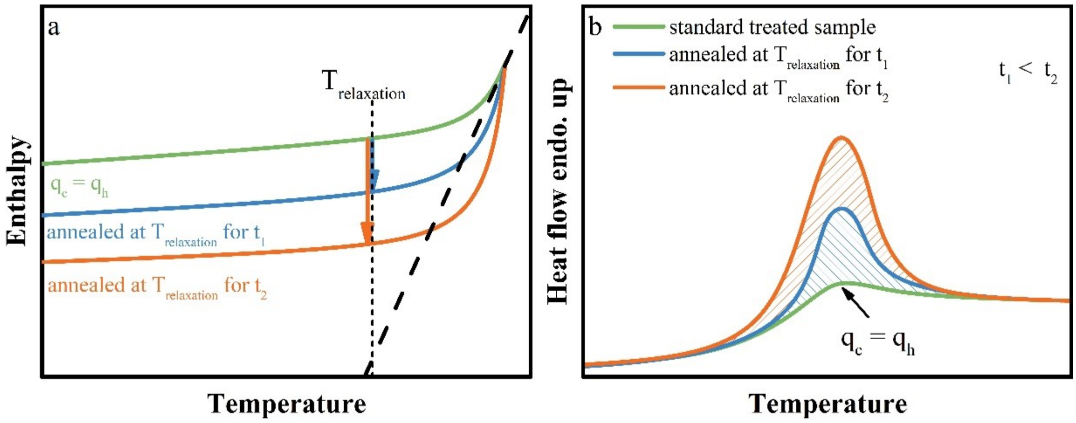

Figure 3-14: a) Enthalpy as a function of temperature upon heating an unrelaxed sample which was heated with the same rate it was cooled before (green) and two samples which were relaxed at $T_{relaxation}$ for different times (orange longer than blue). The arrows show the amount of enthalpy, which is relaxed during the isothermal annealing b) Heat flow as a function of temperature of the three samples. The most relaxed sample (orange) shows a large enthalpy recovery peak in comparison to the unrelaxed sample.

From such measurements not only the enthalpic state, but also the molar heat capacity difference between glass and liquid $\Delta c_p^{liquid\text{-}glass}$ can be determined. For a temperature $T=(T_1+T_2)/2$, $\Delta c_p^{liquid\text{-}glass}(T) = \Delta H^{liquid\text{-}glass}(T_1)-\Delta H^{liquid\text{-}glass}(T_2)/(T_2-T_1)$. $\Delta H^{liquid\text{-}glass}(T_i)$ can be determined by comparing the enthalpy recovered after long isothermal annealing to the recovery after short time annealing as the long time reflects the liquid and the short time reflect the glassy state. The absolute molar heat capacity of the supercooled liquid is $\Delta c_p^{liquid}(T) = \Delta c_p^{liquid\text{-}glass}(T) + c_p^{glass}$ [220,221].

Data collection

The enthalpy recovery experiments were performed in a Perkin Elmer power compensated DSC 8500 and a Mettler Toledo Flash DSC 1. After a standard treatment of the samples, where they were heated into the supercooled liquid at 418 K and cooled with a rate q_c of 0.333 K s^{-1} to guarantee the same enthalpic state for all samples, the experiments were done in two steps. At first, the samples are held isothermally for different times at a given temperature below T_g and then cooled to room temperature with a rate of 0.333 K s^{-1}. Then, the samples were heated with the same rate above T_g to determine the enthalpy recovery. This procedure was done at 358 K, 363 K, 373 K, 378 K.

3.3.2 T_g shift measurements

It has been shown that the structural relaxation time at which a system is frozen into a glass is proportional to the applied cooling rate and hence T_g changes with the rate [222–224]. To determine structural relaxation times from calorimetric measurements, T_g shift experiments are performed. Samples are cooled with different rates through the glass transition. The structural relaxation time is determined in the subsequent heating step with the same rate.

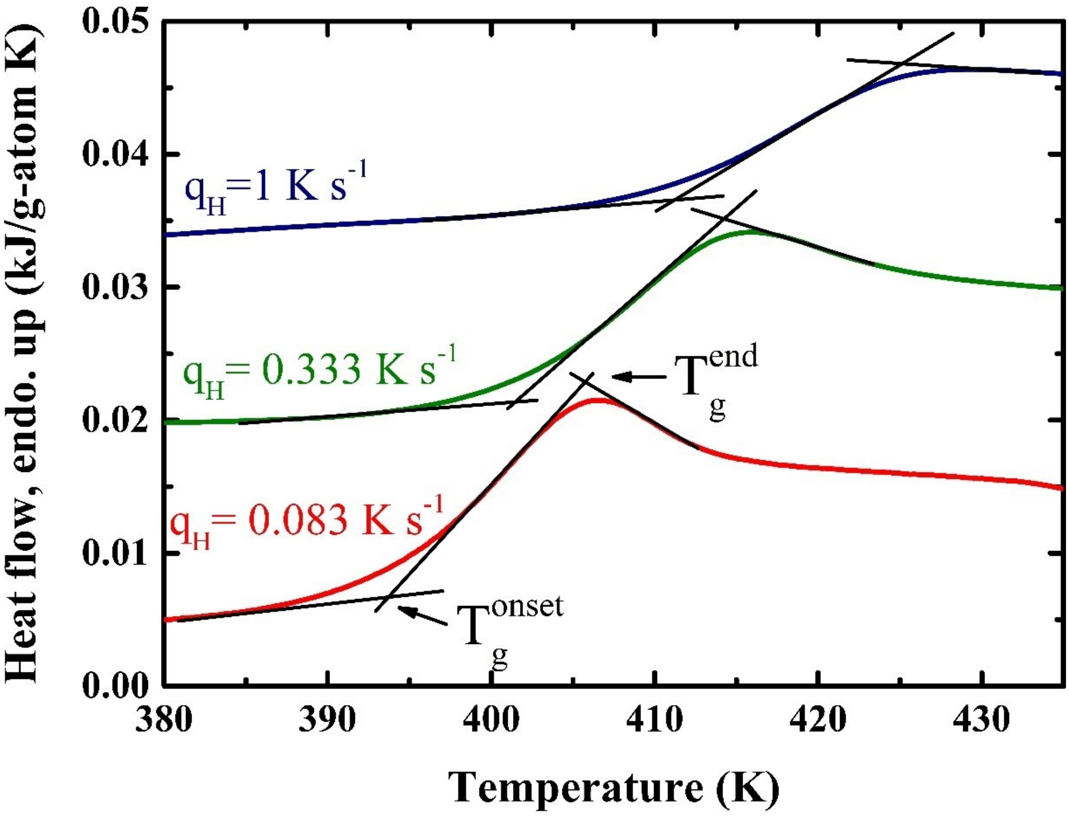

Figure 3-15: Determination of T_g^{onset} and T_g^{end} of the three different heating rates for T_g shift experiments of the $Au_{49}Cu_{26.9}Si_{16.3}Ag_{5.5}Pd_{2.3}$ alloy. The curves are shifted for better clarity.

From the onset and end temperature of T_g, which are determined using the double tangent method as shown in Figure 3-15, the relaxation time τ at the temperature T_g^{onset} is [225]:

$$\tau\left(T_g^{onset}\right) = \frac{T_g^{end} - T_g^{onset}}{q_H}$$

Here, T_g^{end} and T_g^{onset} are the end and the onset temperatures of the glass transition and q_H is the heating rate.

3.4 Thermomechanical Analysis (TMA)

Three-point beam bending is used in the thermomechanical analysis (TMA) to determine viscosities in the range of 10^9 to 10^{14} Pas, which includes the glass transition ($\eta(T_g) = 10^{12}$ Pas) for glass-forming systems.

Data collection

Beams with rectangular cross-sections are centrally loaded with a constant load in a three-point beam bending setup via a silica tip [55]. The setup, which is schematically shown in Figure 3-16, is then heated to the desired temperature and held isothermally. The beam starts to bend under the applied load and the deformation speed, which is measured, is proportional to the viscosity of the material. The viscosity can be calculated from the dimensions of the beam and deformation speed using the Hagy equation [226]:

$$\eta = \frac{g \cdot L^3}{144 \cdot I_c \cdot v} \cdot (M + \frac{\rho \cdot A \cdot L}{1.6})$$

Here, g is the gravity acceleration, L is the distance between the support points, and I_c is the cross-sectional moment of inertia. M is the load, ρ is the density of the material, v is the deformation speed of the beam and A is the cross-section.

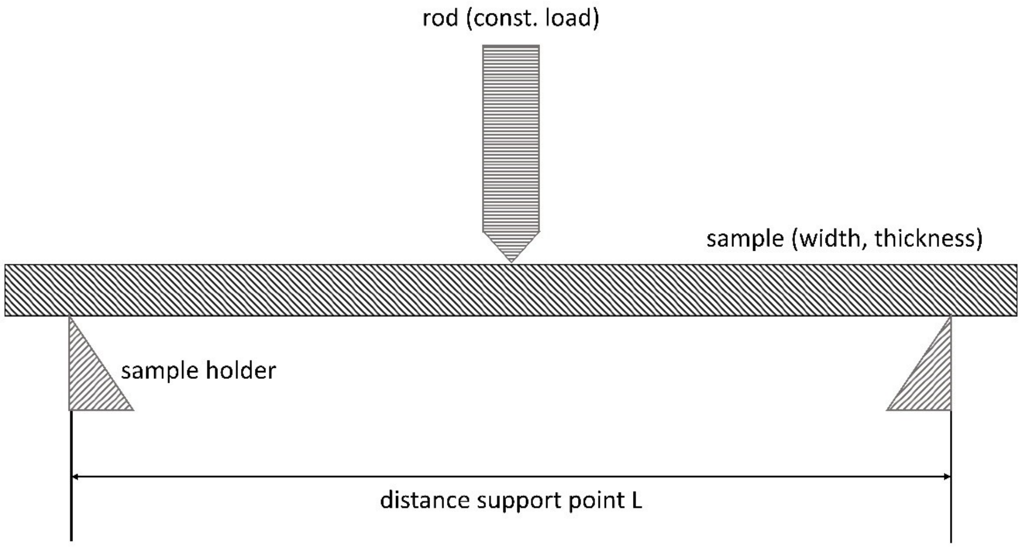

Figure 3-16: Schematic of the three-point beam bending setup used to determine viscosity in vicinity of the glass transition. The sample is loaded by the rod leading to a continuous deflection of the beam from which the viscosity of the sample can be determined.

Beams with rectangular cross-section (width= 2 mm, thickness= 0.4-0.9 mm) were loaded centrally with 10 g and heated with a constant heating rate of 20 K min^{-1} and held isothermally at different temperatures between 368 and 393 K in a Netzsch TMA 402 F3 Hyperion Thermomechanical Analyzer. The samples were held isothermally during the aging process until the equilibrium viscosity was reached. The equilibration process was fitted with a Kohlrausch-Williams-Watts (KWW) stretched exponential equation to determine the equilibrium viscosity η_{eq} , e.g. [227]:

$$\eta = \eta_{initial} + \eta_{equilibirum-initial}(1 - \exp(-\left(\frac{t}{\tau_{aging}}\right)^{\gamma}))$$

$\eta_{initial}$ is the initial viscosity when the isothermal temperature is reached. $\eta_{equilibrium-initial}$ is the change in viscosity until the equilibrium is reached. Therefore, $\eta_{equilibirum}$=$\eta_{initial}$ + $\eta_{equilibrium-initial}$. t is the experimental time, τ_{aging} is the aging time and γ is the shape parameter for that process. τ_{aging} and γ are different to the structural relaxation time τ and the shape parameter β described in section 3.2.1. In XPCS the relaxation time is measured on the atomic level and here it is measured on a macroscopic sample.

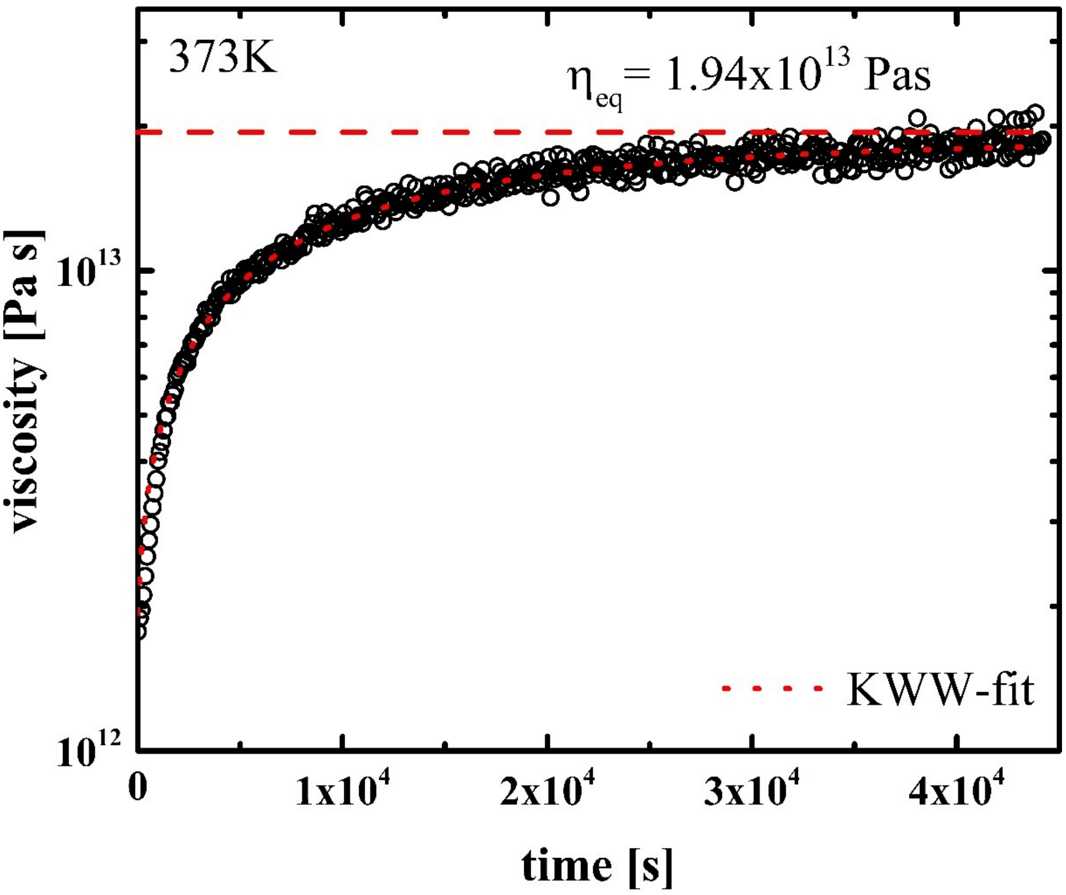

Figure 3-17: Viscosity of the $Au_{49}Cu_{26.9}Si_{16.3}Ag_{5.5}Pd_{2.3}$ as a function of time measured in a 3PBB setup at 373 K. The data are fitted with the KWW equation and the equilibrium viscosity is determined as 1.94x10^{13} Pa s.

The macroscopic measurements rather give the time to age into equilibrium [228], whereas the microscopic XPCS measurements determine an instantanious equilibrium relaxation time. The results from atomic and macroscopic measurements can deviate considerably [52]. Figure 3-17 shows the viscosity as a function of temperature for the isothermal measurement. The data are fitted with the KWW equation given above.

3.5 Couette rheometry

A Couette rheometer has been used to measure viscosities at controlled temperatures and shear rates. The apparatus uses a rotating concentric cylinder in a shear cell geometry adhering to DIN 53019-3 standards (Mooney/Ewart measuring system). The viscosity η (Pa s) is calculated according to Ref. [229]:

$$\eta = \frac{(R_0^2 - R_i^2)}{4\pi L\, R_0^2\, R_i^2\, c_L} \frac{M}{\omega}$$

Where L, R_i and R_o, correspond to the immersion length of the bob in the melt, the radius of the inner cylinder (bob) and the outer radius of the shear cell (inner radius of the cup), respectively. ω is the radial velocity of the bob in rad/s, which is computer controlled. M is the reaction torque on the cup in Nm, which is measured with a high sensitivity torque sensor. The conical apex of the bob prevents the entrapment of gas bubbles. The correction factor c_L accounts for the torque contribution from the conical apex.

The vacuum chamber was evacuated to 10^{-4} mbar and subsequently filled with approximately 500 mbar of high purity Ar (≥ 99.999 %)) before each experiment. The titanium getters and shear cell were heated inductively using a high frequency rf generator. A type K thermocouple, which was embedded in the crucible, was used to measure the temperature. The temperature of the shear cell was regulated by a custom built LABVIEW controller. NIST traceable silicone oils possessing viscosities of 9.6 mPa s, 99.0 mPa s, and 960 mPa s are used for the calibration of the viscosity range of the device.

Steel (C45) was used as shear cell and bob material. Both components were exposed to a nitriding process (4 h at 833 K in N_2), in order to generate a protective nitride layer on the surface of both parts providing the combination of sufficient wetting and no severe reaction between crucible material and melt.

The samples were heated to 300 K above their liquidus temperature in the Couette rheometer and a stepwise shear rate profile was applied in clockwise and counterclockwise directions. The melt was cooled at a rate of 0.33 K s^{-1} until just prior to the onset of crystallization and then immediately reheated to the starting temperature at the same rate. While shearing, this cooling and heating cycle was repeated a total of three times [230].

3.6 Dynamical Mechanical Analysis (DMA)

Dynamical mechanical analysis (DMA) is a technique, in which a material is cyclically loaded and the response function of the material to the oscillating excitation is recorded. Ribbons, beams or plates are cyclically loaded in tension, bending or torsion. From the cyclic load with frequency f, the response function of the material is recorded and storage as well as loss modulus are determined. The schematic of the DMA measurement is shown in Figure 3-18. The loss modulus is calculated from the phase shift between the excitation and the response function of the material and the storage modulus with $E'' = E' \times \tan(\delta)$, where E'' is the loss modulus, $E'$is the storage modulus and δ is the phase shift of excitation and response function. Upon heating, the loss modulus of the material exhibits a maximum at that temperature, where the structural relaxation time corresponds exactly to the applied excitation frequency. The structural relaxation time τ of the material is connected to the applied frequency via

$$\tau = \frac{1}{2\pi f}$$

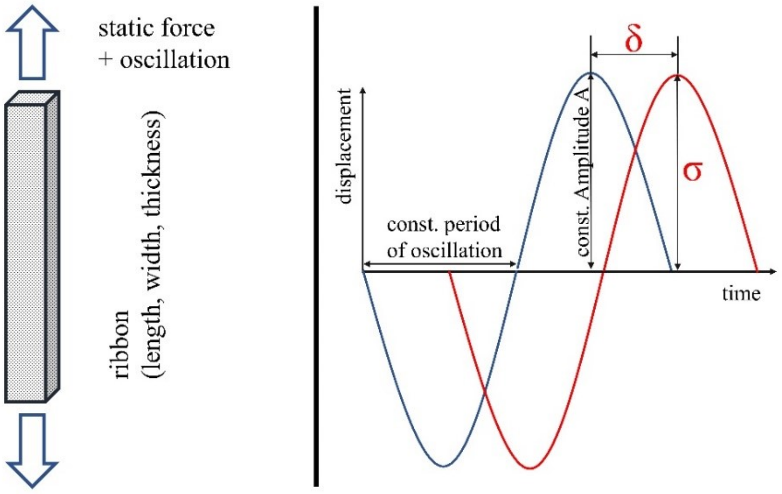

Figure 3-18: Schematic of the principle of measurement in a DMA. Ribbons are cyclically loaded with a fixed frequency upon continuous heating with a fixed rate and the response function of the material is recorded (red line) from which the storage and loss modulus of the material are determined.

Figure 3-19 shows the loss modulus curve recorded during a DMA measurement. For different frequencies (relaxation times) the peak is shifted to different temperatures. Therefore, the temperature dependence of the structural relaxation time τ can be determined by measuring at different frequencies.

Data collection

DMA measurements were performed in a TA Q800 Dynamic Mechanical Analyzer. Melt spun ribbons with thicknesses between 10 and 20 μm were measured in tensile mode. The measured length of the ribbons was about 5 mm. The preload force, which was applied to strain the ribbon during the cyclic experiment, was 0.5 N. The applied amplitude of the oscillation was 1 μm at 5 different frequencies (0.1, 0.3, 1, 3 and 10 Hz). The ribbons were heated with a constant heating rate of 2 K min^{-1} up to 430 K to determine the temperatures, which correspond to the relaxation times determined by the different frequencies.

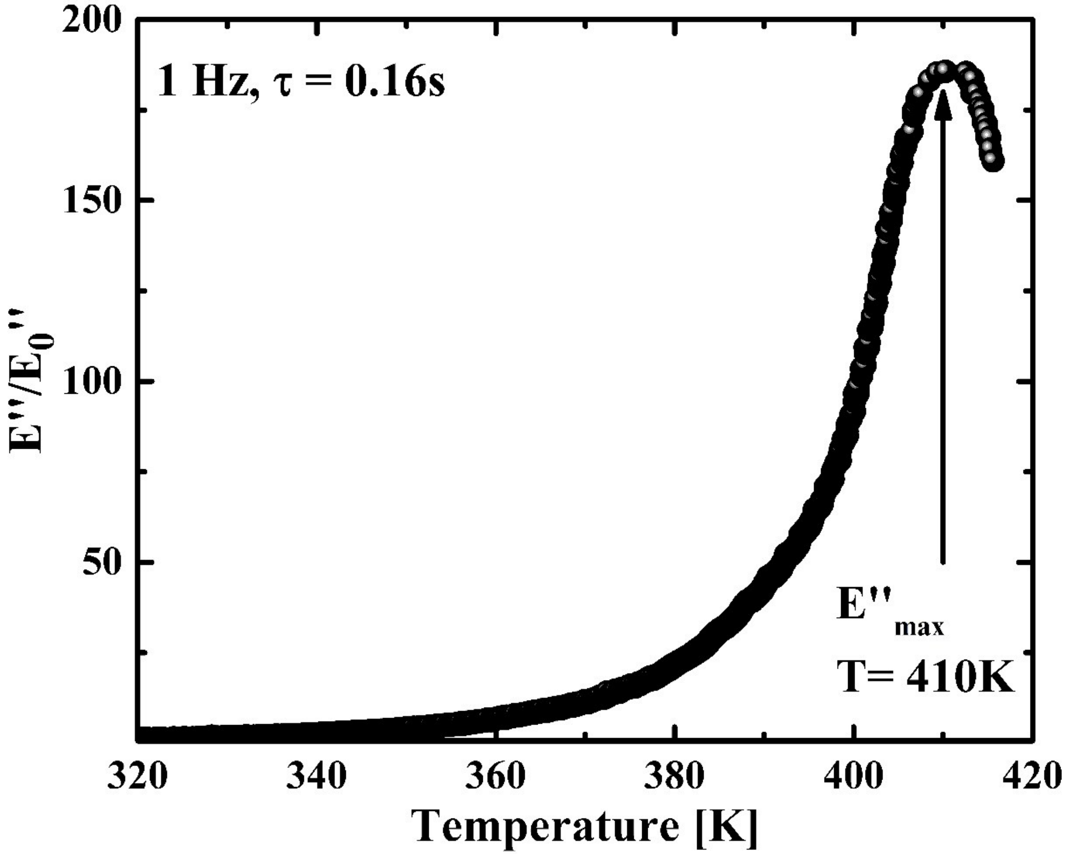

Figure 3-19: Normalized loss modulus as a function of temperature and a modulation frequency of 1Hz. The temperature, at which the loss modulus maximizes, corresponds to the relaxation time of 0.16 s, which results from the applied frequency.

4 The Glass

In the following chapter the behavior of the $Au_{49}Cu_{26.9}Si_{16.3}Ag_{5.5}Pd_{2.3}$ alloy in the glassy state is described and discussed. For that reason, the results from the XPCS measurements are analyzed during the slow heating protocol, which was used. As already mentioned before, the thermal history of a glass is crucial for the understanding of the state in which the glass is in. Hence, the thermal protocol, which the samples experienced in the experiments is described in the beginning.

4.1 Thermal Protocol in the glassy state during XPCS

The ribbons of the $Au_{49}Cu_{26.9}Si_{16.3}Ag_{5.5}Pd_{2.3}$ alloy, which were investigated during the XPCS experiments were produced by melt spinning (see section 3.1.4). Typical cooling rates for this process are up to 10^6 K s^{-1}. Due to this very high cooling rate, the material is frozen in a high energy state. As the material ages considerably at room temperature, the sample are kept in the freezer at 255 K.

As already described in section 3.2.1, XPCS can measure relaxation times in the range between 10s and 10.000 s. Due to the super-Arrhenius temperature dependence of relaxation time the temperature range, in which a metastable equilibrium liquid exhibits these structural relaxation times is narrow. For this reason, the equilibration of the glass into the liquid must be done slowly to stay in the measuring range of XPCS. If the glass is heated too fast to high temperature the dynamics become too fast to be measurable in XPCS. But on the other hand, the equilibration must be fast enough to be able to acquire sufficient data within the limited beam time at the synchrotron. In this light, the $Au_{49}Cu_{26.9}Si_{16.3}Ag_{5.5}Pd_{2.3}$ alloy is experimentally very advantageous for XPCS experiments. The low T_g of 395 K allows a slow equilibration upon heating from the glass within a reasonable amount of time. Within the six days of beamtime, which were provided by the ESRF, it was feasible to equilibrate the material into the supercooled liquid using a very slow heating protocol to be able to observe the equilibration process in situ.

To be able to determine the relaxation time upon heating from the glass, long isothermal intervals were chosen to record and correlate the speckle pattern at the given temperature between the heating steps.

The thermal protocol was the following: The sample was heated with 1 K min^{-1} from room temperature (295 K) to 363 K with isothermal steps of 3 h every 5 K. From 363 K on, the sample was held isothermally every 2 K and heated until 396 K with isothermal steps between 180 min and 20 min.

This thermal protocol is very different from standard thermal treatments of glasses. Normally, glasses are heated in a single step to temperatures below T_g and held isothermally to observe the equilibration process in-situ, as for example done in viscosity or volume equilibration experiments, or they are heated with a continuous rate into the supercooled liquid to observe T_g and the associated enthalpy recovery of the glass when entering the liquid phase. Therefore, the stepwise heating is a very special treatment allowing a new look on the equilibration process of glasses, which is described in the following section.

4.2 Aging behavior

Due to the melt spinning the liquid is frozen in a high energy state as a high cooling rate leads to a higher glass transition temperature and a high energy state of the glass (see Figure 2-9). During the thermal protocol (see previous section 4.1) the sample relaxes from its high energy state towards the supercooled liquid.

Figure 4-1a shows the temperature dependence of the structural relaxation time τ upon slowly heating from the high energy glassy state. Upon heating the glass should relax towards the supercooled liquid state. As can be seen, two regions are distinguishable. At lower temperatures, τ appears to be temperature independent. Upon further heating, τ becomes highly temperature dependent at a value of 377 K before the glass equilibrates at 395 K into the supercooled liquid.

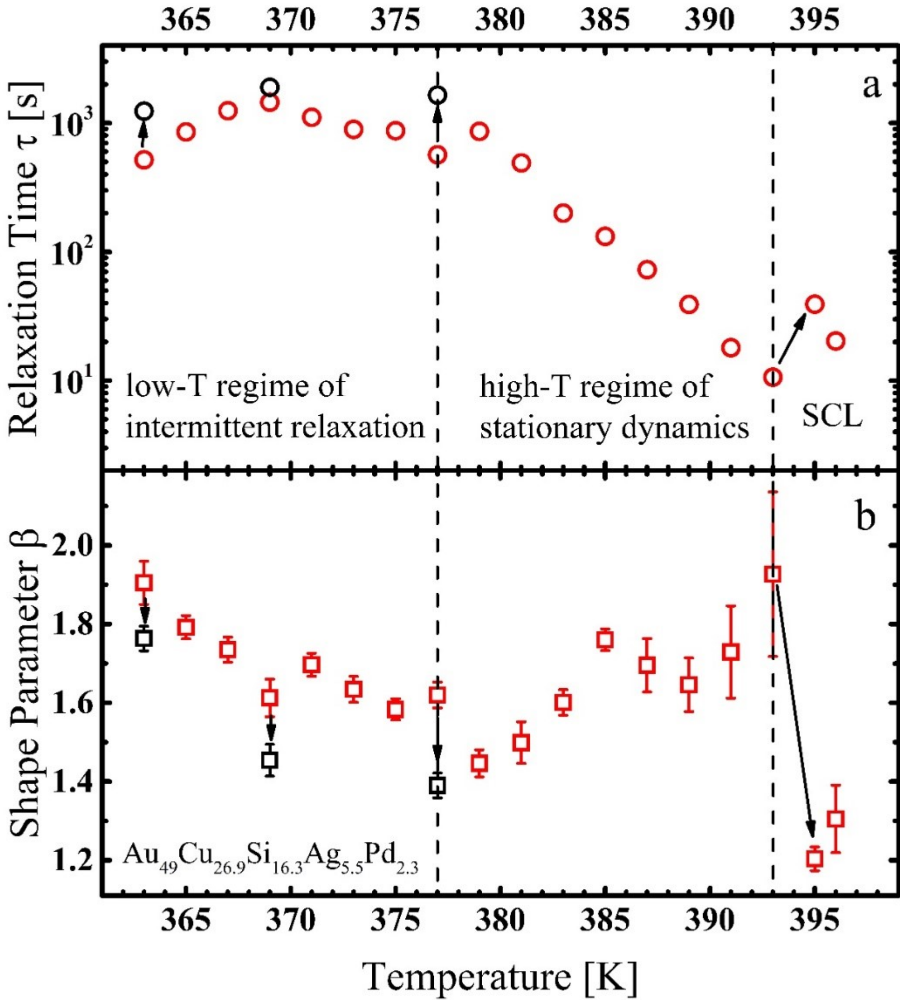

Figure 4-1: (a) Structural relaxation time τ as a function of the temperature. At 377 K the temperature dependence changes from a nearly temperature independent behavior below to a highly temperature dependent behavior above. (b) Shape parameter β as a function of temperature in the glassy state. β stays highly compressed even though the relaxation time becomes highly temperature dependent, proofing the glassy nature of the dynamics.

In the first region where we observe temperature independent behavior, the material exhibits stationary dynamics. Based on a statistic process the stationary dynamics are interrupted by intermittent aging events as can be seen in the TTCF shown in Figure 4-2. The figure is cut into two pieces as two sets of data were acquired which cannot be merged afterwards.

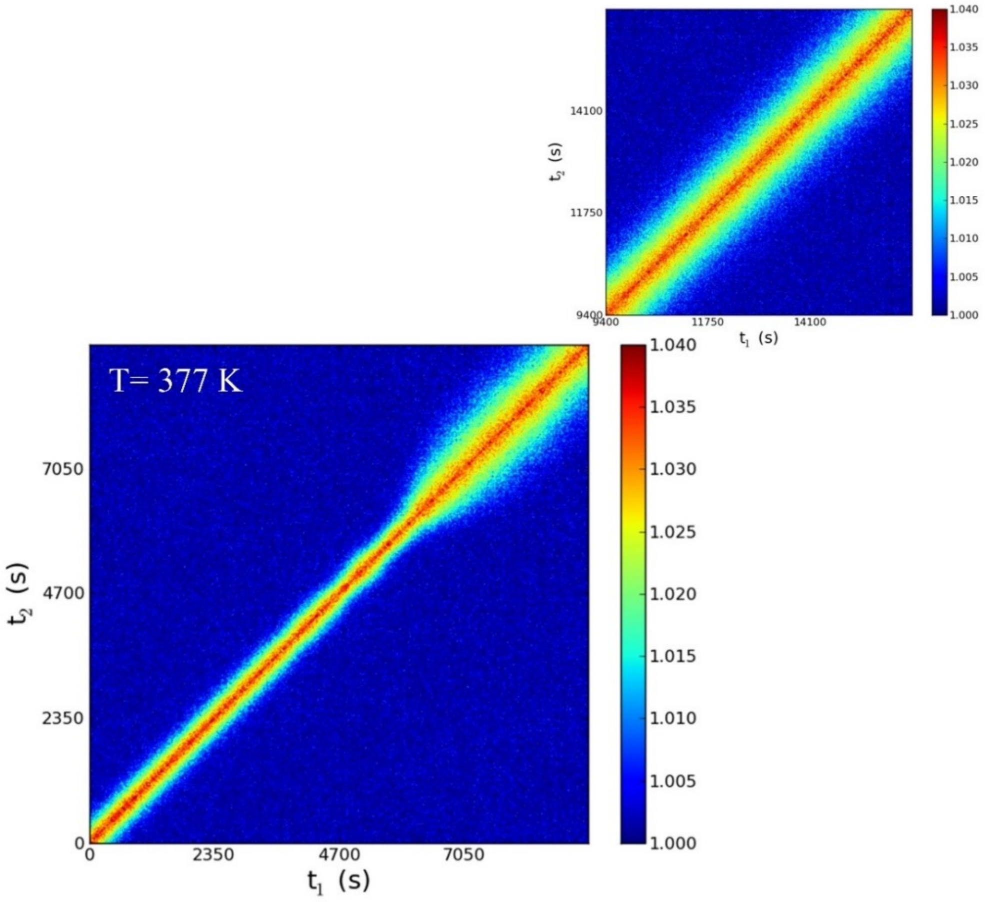

Figure 4-2: TTCF at 377 K. The aging occurs intermittently after about 6000s as the broadening indicates. After the aging event, the TTCF appears stationary again with no sign of further aging. The figure is reproduced from [219].

Such intermittent aging events lead to a significant increase in τ as shown by the arrow in Figure 4-1a and in the $g_2(Q,t)-1/c$ function of Figure 4-3. τ increases from a value of about 560 s before the aging event to 1650 s afterwards. During the aging process the shape parameter β increases from a value of 1.6 in the stationary dynamics before to a value of 2.0 and drops afterwards to a value of 1.4 in the following stationary regime. This is illustrated in Figure 4-4. The shape parameter shows a peak during the aging event and drops afterwards to a lower value than before. At the same time, τ increases significantly. Our research group has found this kind of aging behavior before in a Pd-based bulk metallic glass-forming alloy [52].

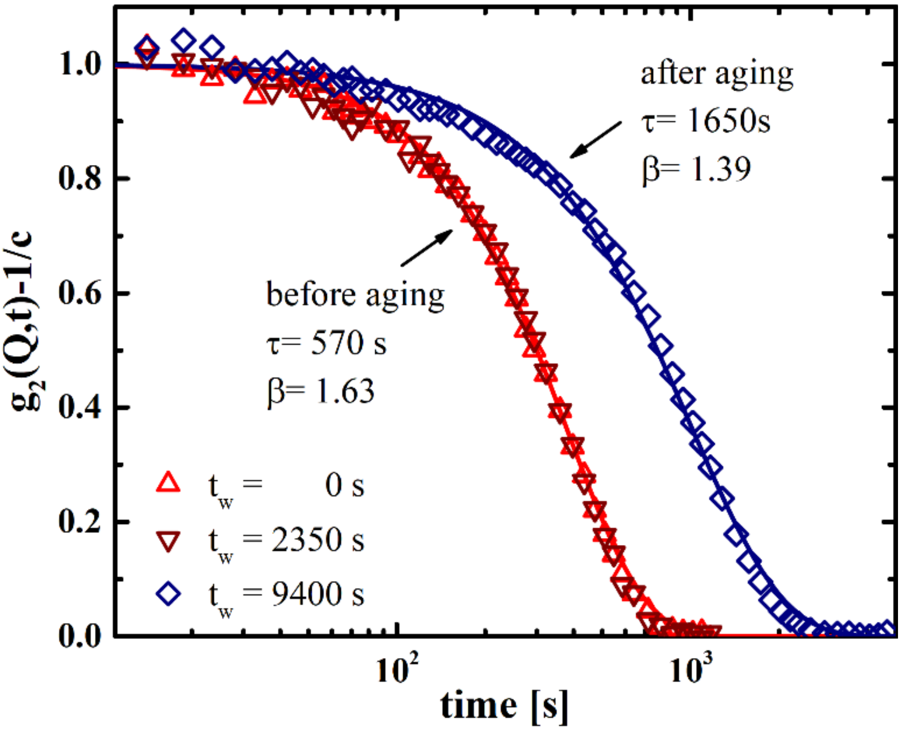

Figure 4-3: $g_2(Q,t)$-1/c at 377 K corresponding to the TTCF in Figure 4-2. The aging increases the relaxation time significantly from 570 s to 1650 s. The data are from [219].

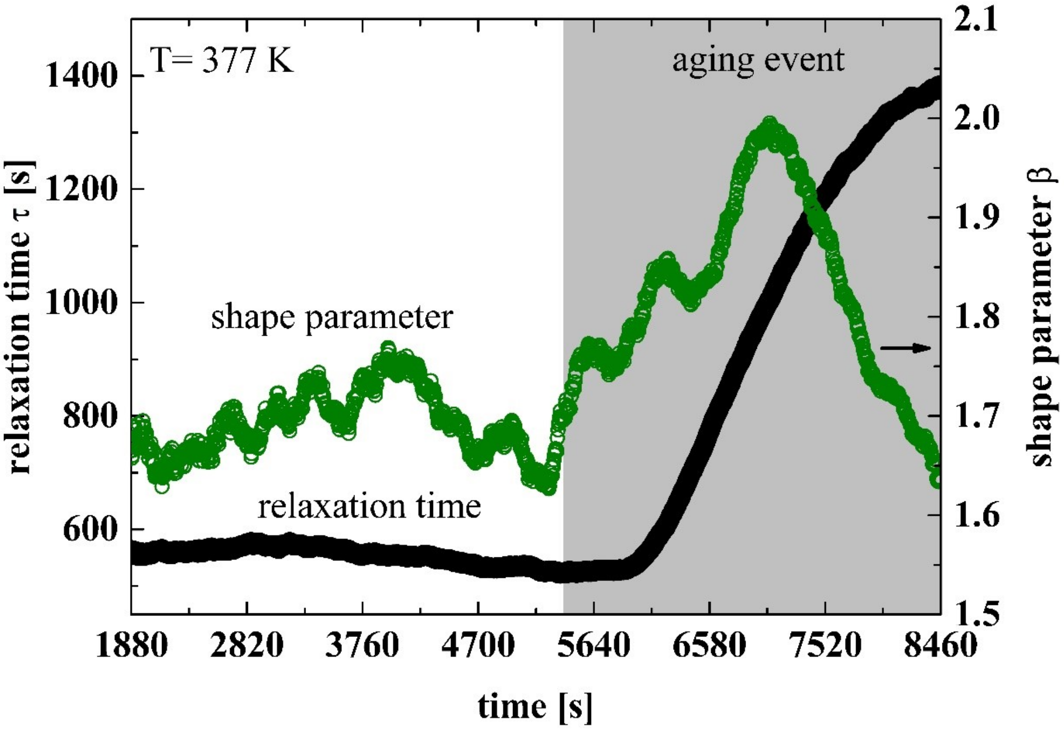

Figure 4-4: Evolution of relaxation time and shape parameter as a function of time at 377 K. τ exhibits a continuous increase, whereas β shows a maximum during the aging event.

In the highly temperature dependent region above 377 K, no sign of aging can be found anymore. The TTCFs in that region show stationary behavior (see Figure 4-5) over the entire experimental time even if the sample was held isothermally at a single temperature for several hours, which is one order of magnitude longer than the structural relaxation time. Figure 4-6 shows the intensity auto-correlation functions for several temperatures above 377 K in the temperature dependent region. The shape of all functions show compressed behavior with β >>1, which is a result of ballistic-like motion in the material due to the internal stresses introduced into the glass through the casting process [175,176,228]. This compressed behavior has been found in metallic glasses, oxidic glasses and colloid systems before. This is a clear indication for glassy behavior, proving that this region cannot be associated to the supercooled liquid.

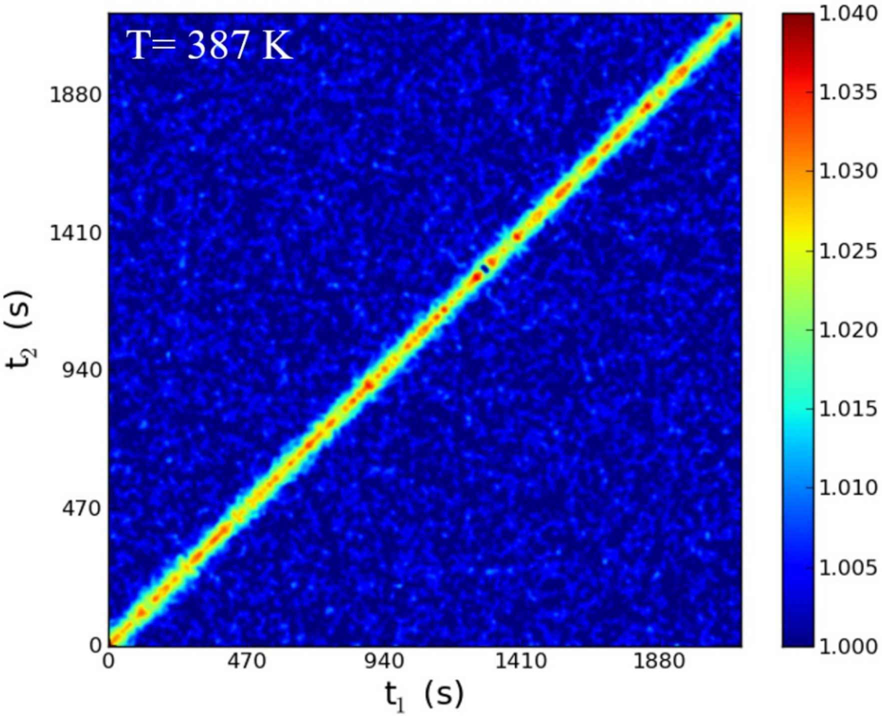

Figure 4-5: Two times correlation function measured at 387 K in the glass upon heating. The dynamics are stationary with no sign of aging.

Figure 4-1 illustrates the temperature dependence of τ and β for both regions. Although the temperature dependence changes significantly at 377 K the shape parameter β is not influenced, exhibiting values significantly above 1. The alloy appears to be stuck in a deep energy minimum, which is not the metastable supercooled equilibrium liquid.

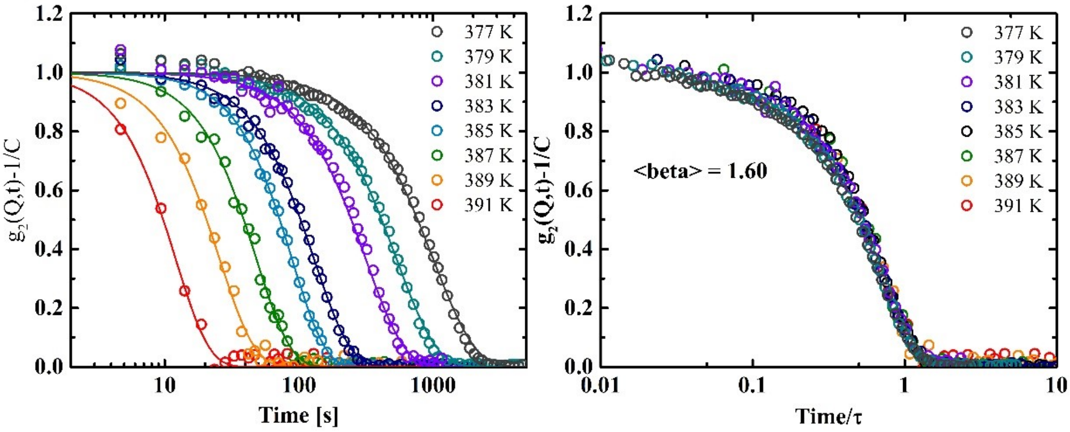

Figure 4-6: a) $g_2(Q,t)$-1/C at 8 different temperatures in the highly temperature dependent regime above 377 K. The functions are highly compressed. b) The temperature time superposition for the functions from a). The curves exhibit the same shape β=1.60±0.15.

4.2.1 Enthalpy recovery experiments

The enthalpy recovery experiments shown in Figure 4-7 mirror qualitatively the intermittent aging behavior observed below 377 K in the XPCS experiment. Figure 4-7a shows the enthalpy recovered after different annealing times at 373 K. The longer the annealing time, the larger the endothermic overshoot representing the enthalpy which is recovered. Each curve in Figure 4-7a reflects one data point in Figure 4-7b, where the enthalpy relative to the total enthalpy released at a temperature is shown as a function of time. The enthalpy release is not continuous. Figure 4-7b shows several plateaus for different annealing temperatures. The plateaus are clearly shaped especially at lower temperatures [231] and are reminiscent of the intermittent aging behavior observed in the XPCS experiment.

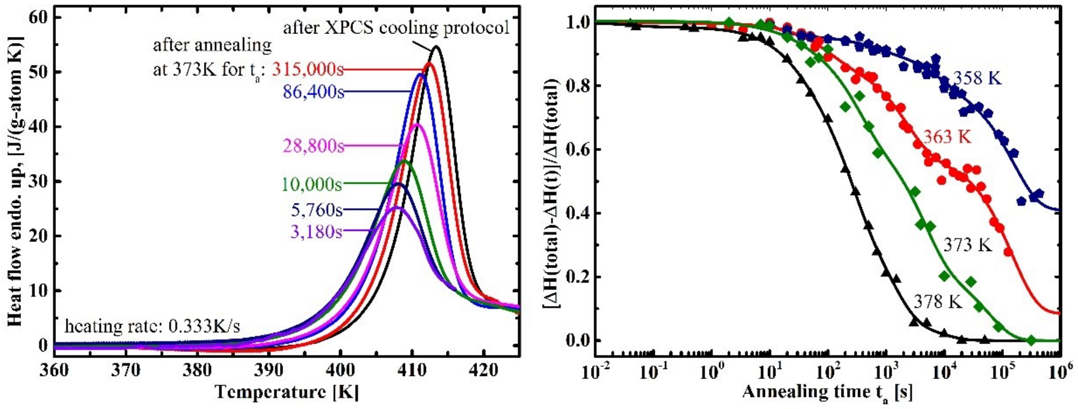

Figure 4-7: a) Enthalpy recovery measurements with a rate of 0.333 K s^{-1} after different annealing times at 373 K. The enthalpy which is recovered increases with increasing annealing time. b) Relative enthalpy which is recovered as a function of the annealing time for 4 different temperatures. As can be seen, the enthalpy does not increase plainly logarithmically with time, but shows step-like behavior. The figure is reproduced from [219]

4.3 Discussion

The alloy shows very particular aging behavior on the atomic scale in the XPCS experiments. At temperatures below 377 K, the dynamics of the alloy appears to be temperature independent (see Figure 4-1a). The dynamics is stationary with intermittent aging events during which the relaxation time increase continuously (see Figure 4-2, Figure 4-3, Figure 4-4). This intermittent aging has been observed before in a Pd-based metallic glass [52], where it has been associated to the evolution of the material from a high energy state to energetically lower states through hopping from one local minimum to the next in the energy landscape. The energy landscape reflects all possible configurations of the alloy energetically and each configuration is described by a local minimum in the energy landscape. Through aging events, the material evolves in this energy landscapes from energetically unfavored local minima to energetically more favored minima. This is a statistic process as each minimum possesses an activation energy barrier which must be overcome. This leads to an intermittent aging behavior as the system does not continuously evolve but gets trapped in local minima which it has to leave. This hopping down the energy landscape is likely also the reason for the intermittent aging behavior in the Au-based system. Each hopping event lead to an aging event in the TTCF. The plateaus in the enthalpy recovery experiments (see Figure 4-7) are reminiscent of the intermittent aging events in XPCS. Although the behavior appears to be very similar, there are several differences which must be considered.

First, the two measurement techniques probe different sample sizes. The enthalpy recovery experiments use large sized samples from which the released heat after the glass transition is measured to deduce the enthalpic state of the glass which was frozen-in. For this reason, the technique probes a macroscopic property. XPCS on the other hand is a technique that probes atomic motion microscopically.

Second, the thermal protocol of the XPCS sample is completely different from the one of the enthalpy recovery samples. The XPCS sample is heated slowly and held isothermally every 5 K. Therefore, the sample start to age at lower temperatures during the isothermal annealing and moves down the energy landscape. When it reaches the temperatures at which the samples of the enthalpy recovery experiments are annealed, the sample is on a significantly lower enthalpic state, as the enthalpy recovery samples, which are heated with a constant rate of 20 K min^{-1} to their annealing temperature and do not have the possibility to relax before reaching the annealing temperature.

The very different thermal protocols and the different length scales on which the two techniques probe the sample, make a quantitative comparison impossible, as can be seen when the enthalpy recovery at 378 K (see Figure 4-7) and the TTCF at 377 K (see Figure 4-2) are compared. The enthalpy recovery experiment shows no plateau-like behavior and the maximum heat is released after 2000 s, whereas the TTCF shows no aging for about 6000 s, before the first aging event occurs. This suggests that the sample, which has been heated very slowly during the XPCS measurements, is trapped in deep energy minima of the energy landscape, which it can only leave if the activation energy barrier is overcome. As this overcoming is a statistical process it can obviously take a long period of time.

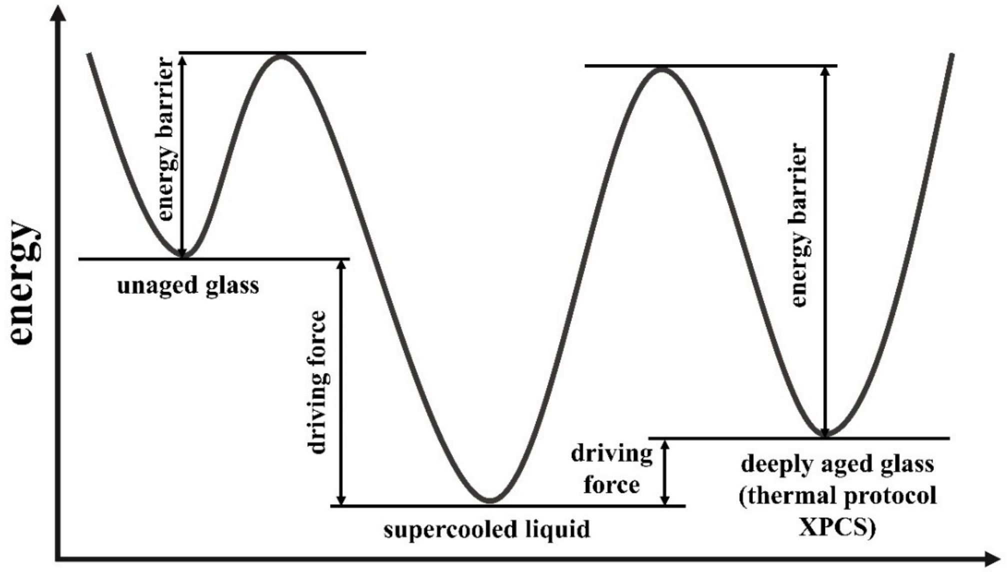

Figure 4-8: Schematic comparison of the energy state with respect to the supercooled liquid of an unaged glass in comparison to the deeply aged glass produced by the thermal protocol. The high energy barrier and the low driving force for equilibration is the reason why the deeply aged glass does not enter the SCL.

Such a deep minimum can be the reason for the temperature dependent region above 377 K measured in XPCS (Figure 4-1a). Figure 4-8 schematically shows the difference between an unaged glass and the glass which has been produced by the thermal protocol during the XPCS upon heating. In comparison to the unaged glass, the glass has aged its way down the energy landscape into a deep minimum so that the driving force for entering the SCL is very low and the activation energy barrier is very high. Therefore, the sample does not equilibrate from this deep minimum, which apparently exhibits a steep temperature dependence of the relaxation time into the SCL although it is held isothermally at various temperatures many times longer than its relaxation time. Only upon further heating it finally equilibrates at 395 K. A possible explanation for the deep minima in the energy landscape could be the different diffusivity of the elements in the alloy. Small atomic species like Si in this alloy is expected to move significantly faster than the large atoms like Au, as has been shown in Zr- based alloys [232]. When slowly heating the sample, the small atoms relax out stresses and free volume before the large atoms can move and lead to a very dense packing without giving the whole system the possibility to rearrange, which would result in the equilibration into the SCL. For this reason, the SCL can only be reached at elevated temperatures where the thermal energy is high enough to overcome the large energy barriers generated by the selective diffusion of the small atoms.

5 The Liquid

In the following chapter, the dynamical, thermodynamic and structural behavior in the supercooled and stable liquid state of the $Au_{49}Cu_{26.9}Si_{16.3}Ag_{5.5}Pd_{2.3}$ alloy is discussed based on results measured with the various techniques described in the material and methods section 3.

5.1 Dynamics in the liquid

5.1.1 Thermal Protocol during XPCS and XRD

As described in section 4.1, the material was slowly heated and equilibrated into the supercooled liquid at 395 K. From that point the material was cooled. Upon cooling, a quasi-static cooling protocol has been applied and the dynamics has been measured using XPCS. The sample was cooled with a rate of 0.1 K min^{-1} interrupted by isothermal annealing steps with a length of 20-240 min every 0.5 K down to 380 K. In a separate experiment the same protocol was used to investigate the structure of the liquid.

5.1.2 Preservation of the amorphous state

After the thermal protocol the material retained its amorphous structure. Although the sample was held in the supercooled liquid for several days, no crystallization occurred. Figure 5-1 shows the S(Q) at 380 K after the quasi-static cooling before quenching the material with a rate of 7 K min^{-1} to room temperature.

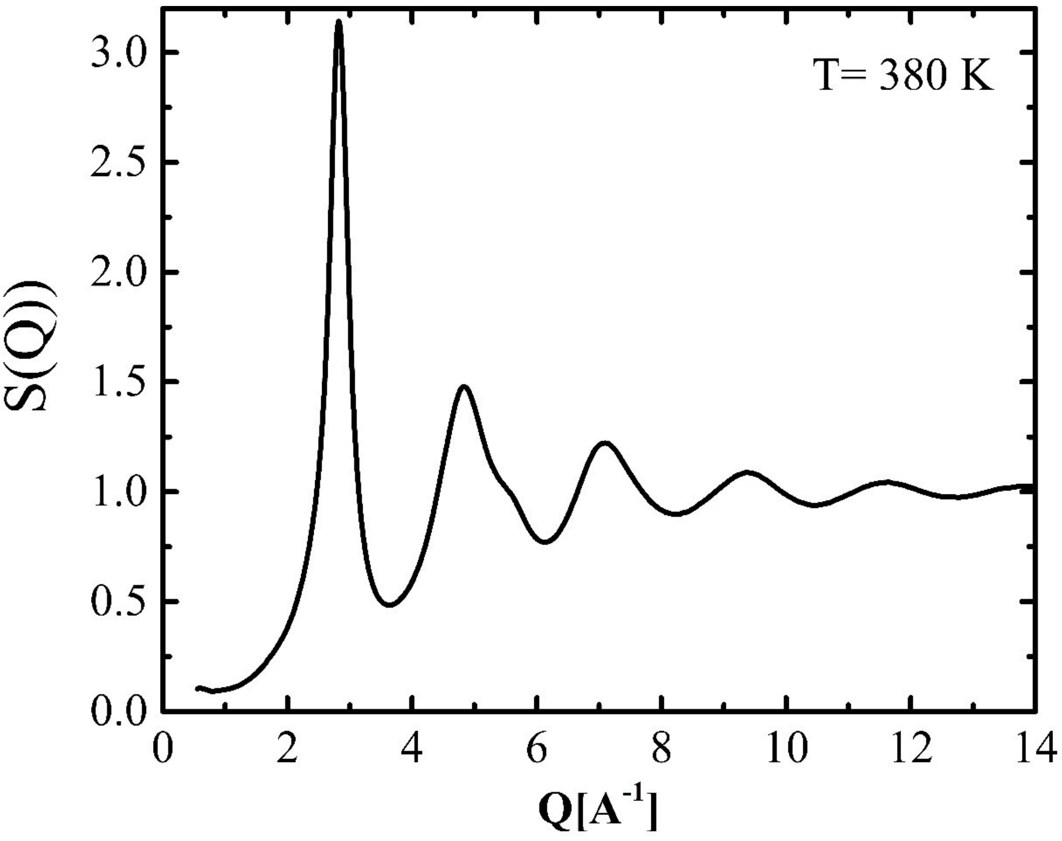

Figure 5-1: Total structure factor S(Q) after the equilibrium cooling at 380 K. No reflexes of crystalline phases are visible after the thermal treatment of six days.

The S(Q) is smooth with no sharp peaks occurring, indicating the preservation of the amorphous structure during the thermal treatment. To confirm the amorphous structure, the heat flow of a sample, which was heat treated with the thermal protocol applied during the XPCS measurements, is compared to a standard treated sample. Figure 5-2 shows the comparison of the two samples. As can be seen, the curves deviate from each other but within the accuracy of the method and exhibit comparable crystallization enthalpies indicating a fully amorphous sample after the thermal protocol.

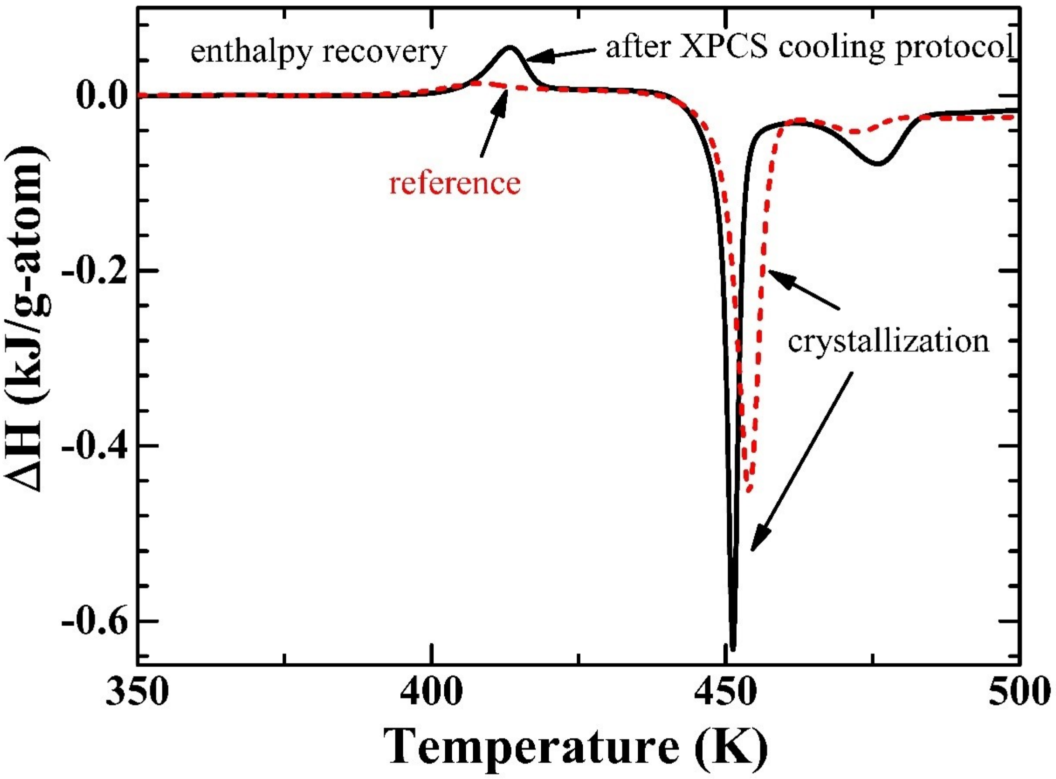

Figure 5-2: DSC scan of the ribbon after the quasi-static cooling treatment as applied in the XPCS experiment (black) and of a as cast reference sample heated with a 20 K min^{-1} (orange). The samples exhibit approximately the same enthalpy of crystallization.

5.1.3 Thermal history and glass transition

Although the amorphous structure is preserved, the thermal history of the sample is changed completely and very unique in comparison to standard heat treatments.

Normally, very high cooling rates are applied to freeze the amorphous structure of the liquid and supercooled liquid to a glass and to avoid crystallization. In the case of the $Au_{49}Cu_{26.9}Si_{16.3}Ag_{5.5}Pd_{2.3}$ alloy, the critical cooling rate in the flash DSC is determined to be between 600 and 1000 K s^{-1} [171,217,218]. To normalize as cast samples, they are standard treated to guarantee the same thermal history and frozen-in state for all samples. The standard treatment includes the heating of the sample into the supercooled liquid, the equilibration in the supercooled liquid and a subsequent cooling with a rate of 20 K min^{-1}.

The thermal protocol applied here is very different. The hyper-quenched ribbons are heated slowly from room temperature above T_g, where they equilibrate into the supercooled liquid and are then cooled with a quasi-static cooling protocol. This very slow cooling rate shifts T_g to lower temperatures in comparison to the standard treatment as T_g is a kinetic event, which occurs at lower temperatures for lower cooling rates. Figure 5-3 shows T_g for different cooling rates (circles) and heating rates (triangles) in a logarithmic diagram. T_g of the applied cooling rate (0.1 K min^{-1}) is extrapolated from the values of different Flash DSC and XRD measurements at higher cooling rates and is estimated to be 380±4 K. The influence of the cooling rate on T_g is significant. T_g changes from 440 K when cooled with 6000 K s^{-1} to 380 K when cooled with 0.00167 K s^{-1}.

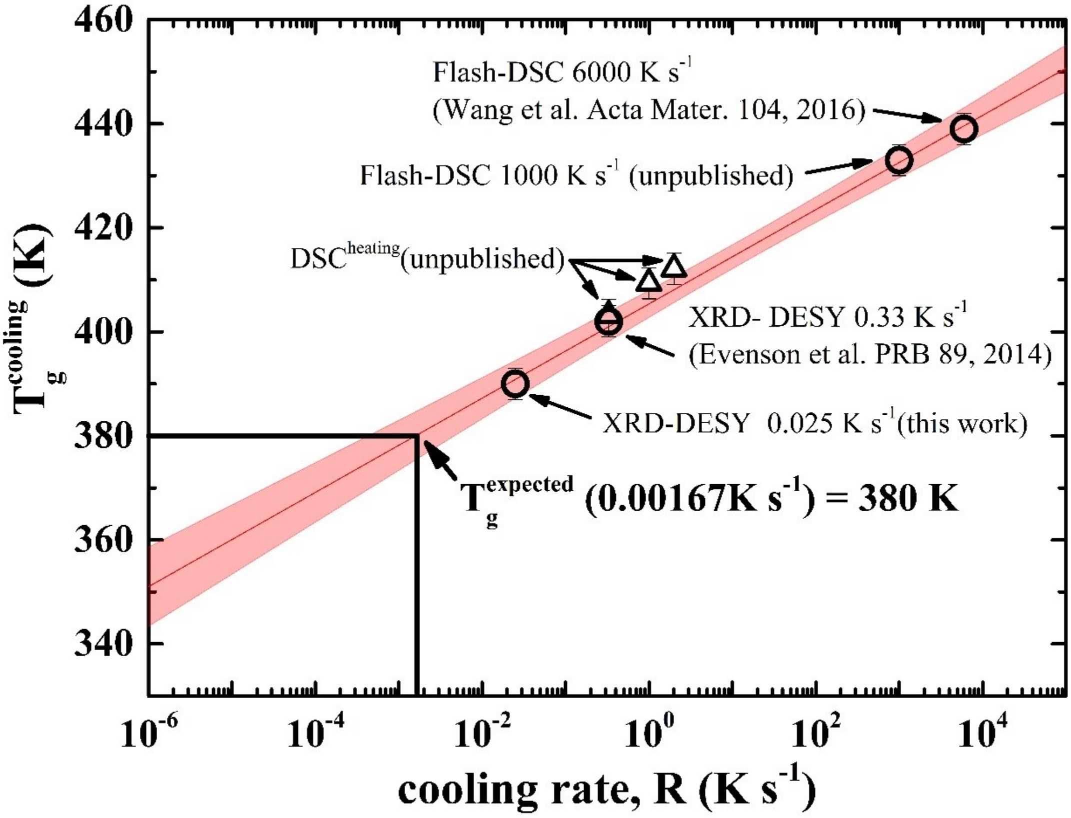

Figure 5-3: Cooling rate dependence of T_g of the $Au_{49}Cu_{26.9}Si_{16.3}Ag_{5.5}Pd_{2.3}$ metallic glass. The expected T_g for the applied cooling rate of 0.1 K min^{-1} is 380±4 K extrapolated from unpublished Flash-DSC data, from Flash-DSC data taken from [171], XRD experiments done in this work and in [168] upon cooling with different rates.

Additionally, the figure illustrates the good agreement of T_g^{end} in heating with the T_g^{onset} upon cooling as can be seen at the standard cooling rate of 20 K min^{-1}. The cooling experiment in XRD gives the same result as the heating experiment in the DSC.

The extrapolation of T_g to 380 K strengthens the assumption that the material is in the supercooled liquid down to at least 380 K upon quasi-static cooling. The investigation of the dynamics between 396 K and 380 K is discussed in the following section.

5.1.4 Dynamics in the supercooled liquid

Upon cooling, the dynamics of the liquid is stationary between 396 K and 380 K. Figure 5-4 shows a representative TTCF for the liquid state. The TTCF's show no sign of aging. We have learned from chapter 4 that stationary behavior is no proof of liquid dynamics as it can be observed in the glass as well.

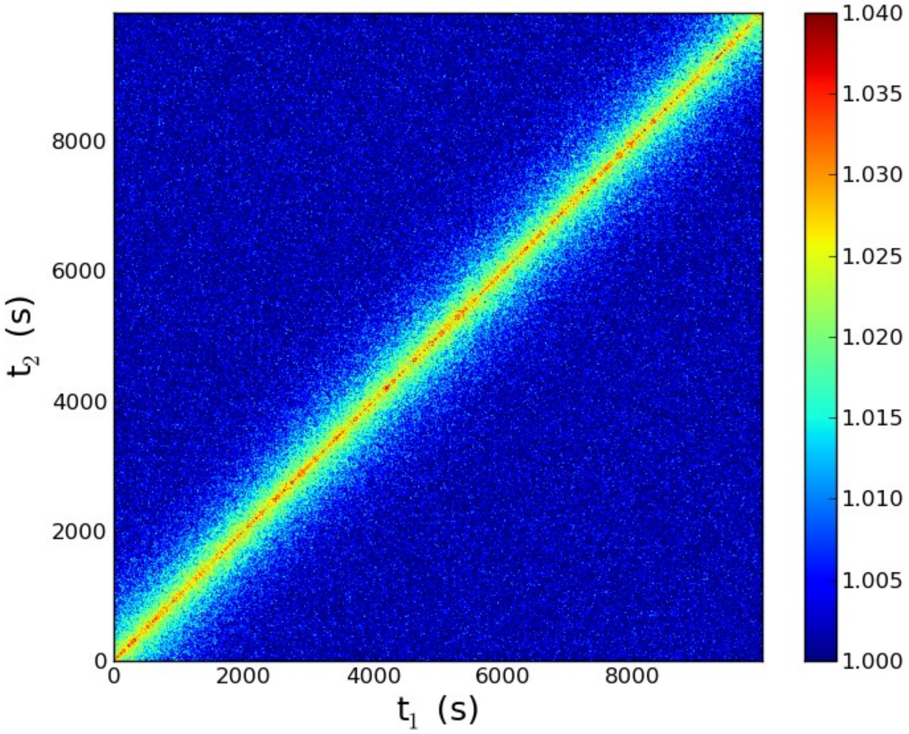

Figure 5-4: TTCF at 386 K. The diagonal keeps a constant width indicating stationary liquid-like behavior.

Nevertheless, stationary dynamics is a necessary condition for liquid behavior. The difference between glass and liquid is observable in the normalized intensity autocorrelation function $g_2(Q,t)$. If it is compressed, ballistic-like motion is dominant and the material behaves as a glass (see chapter 4). The dynamics in the liquid is different. The different atomic species in the alloy diffuse with different timescales resulting in a stretched exponential decay of $g_2(Q,t)$. Figure 5-5a illustrates the temperature dependence of the normalized intensity autocorrelation function $g_2(Q,t)-1/c$. As can be seen, the decay is shifted to longer times with decreasing temperature. The temperature-time superposition holds true and all functions decay with the same shape parameter β of 0.87±0.10 as can be seen in the inset. This is the decisive characteristic and sufficient condition for liquid behavior. The difference between liquid and glassy behavior is shown in Figure 5-5b. Here, the normalized intensity autocorrelation function of the glass upon heating and the liquid upon cooling at 383 K are compared. The differences are obvious. Although measured at the same temperature, the dynamics in the glass is more than one order of magnitude faster than in the liquid. Simultaneously, the shape parameter in the glass is highly compressed whereas it is stretched in the liquid.

Figure 5-6 shows the dynamic susceptibility χ_T (Q,t) measured using XPCS at the FSDP of the S(Q) at 385.5 K. The dynamics exhibits heterogenous processes with relaxation times around 30 s, as indicated by the peak in the dynamic susceptibility. This value is similar to values obtained in colloids and gels close to their dynamical arrest just above T_g [38,193–195]. This is a further indication of liquid-like behavior.

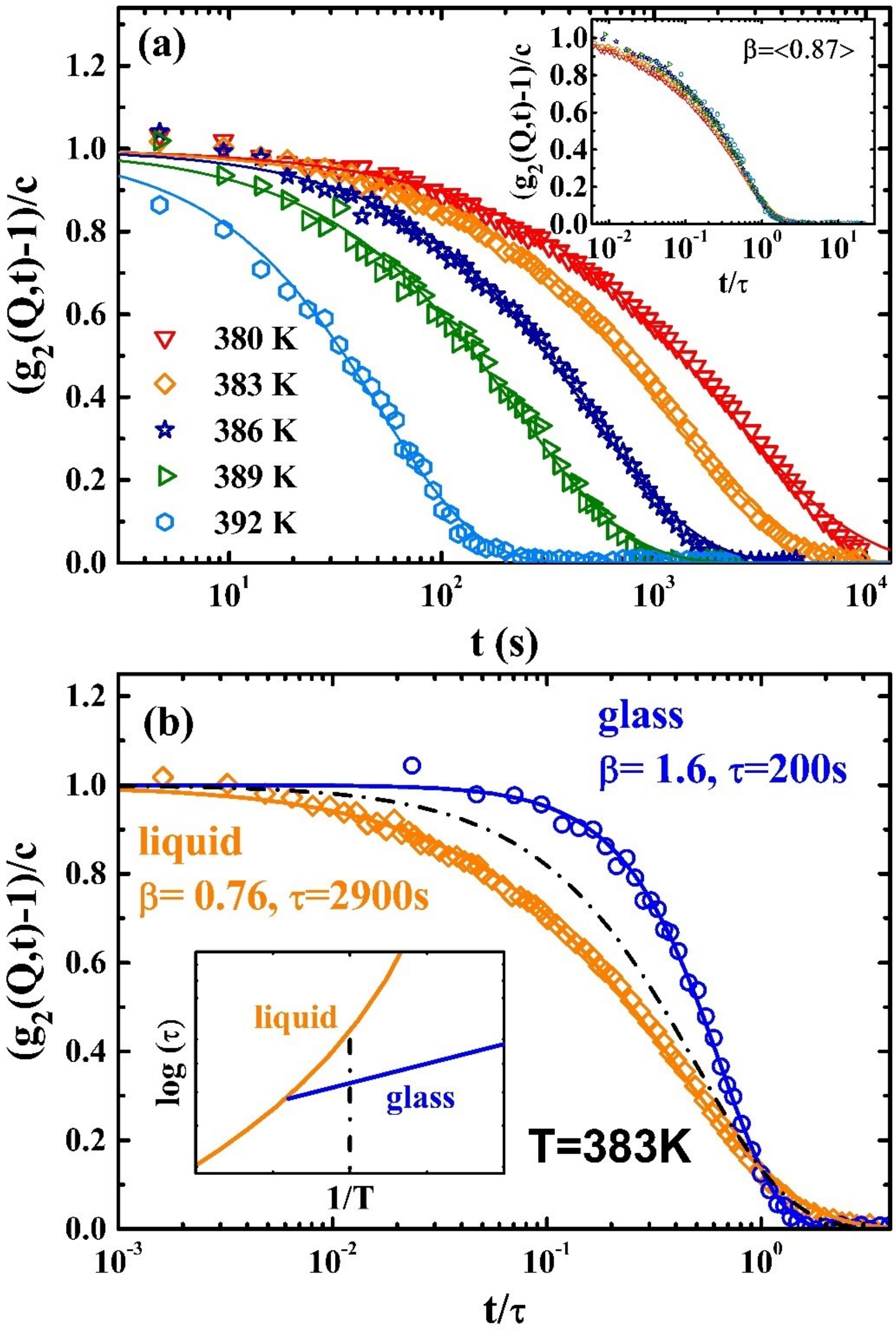

Figure 5-5: (a) Temperature dependence of normalized intensity autocorrelation functions measured with XPCS at $Q_p=2.78$ Å^{-1}. Lines are fits using the KWW function. Inset: Same data shown over t/τ. (b) $g_2(Q_p,t)-1/c$ as a function of t/τ measured at 383 K in an hyperquenched glass heated from low temperature (blue circles), and in the quasi-statically cooled supercooled liquid shown in panel (a) (orange diamonds). The dashed line is a single exponential decay ($\beta=1$). The two curves correspond to two distinct dynamics as sketched in the inset by the intersection of the vertical line with the glass or the liquid.

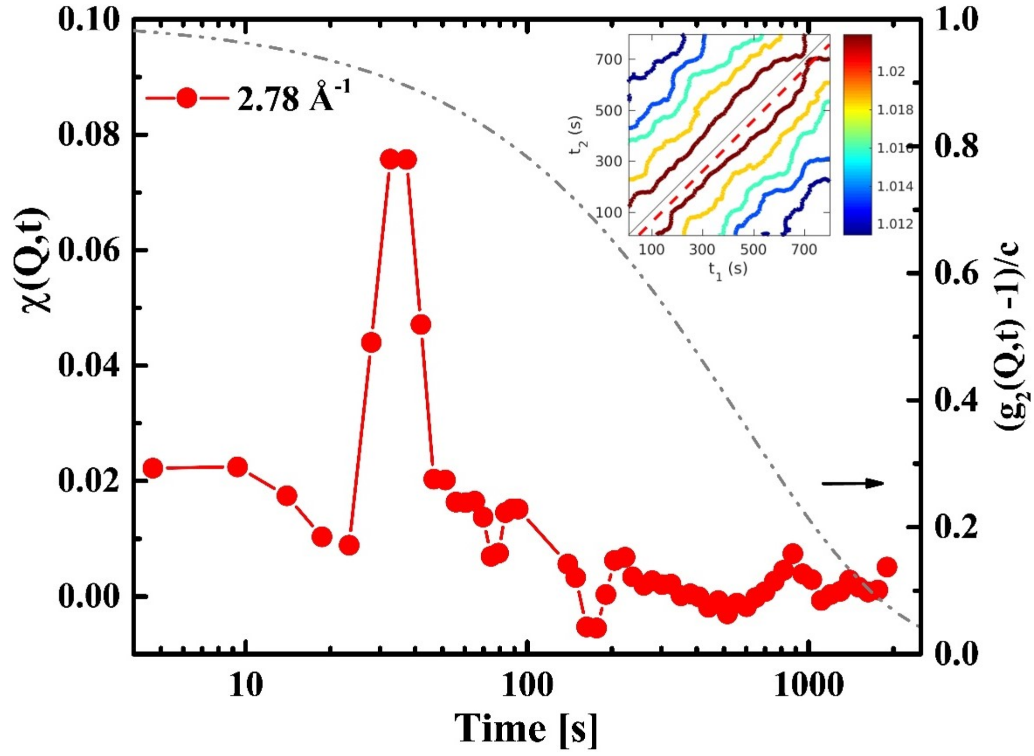

Figure 5-6: Dynamic susceptibility χ_T (Q,t) measured at the FSDP of the S(Q) for Q=2.78 Å^{-1} at 385.5 K. The peaks show the occurrence of dynamical heterogeneities involving mainly processes with fast relaxation times of ≈30 s. The corresponding intensity fluctuations are marked by the red line in the contour plot of a portion of the TTCF (Q=2.78 Å^{-1}) reported in the inset. The dashed-dotted grey line is the fit of g_2 (Q=2.78 Å^{-1},t).

5.1.5 Q-dependence in the ultra-viscous liquid state

To further clarify, whether the nature of the dyamics is glassy- or liquid-like, the Q dependence of the dynamics has been measured. At 385.5 K, which is above the expected glass transition for the applied cooling rate, the dynamics was measured at eight Q values around the FSDP. Figure 5-7 shows two TTCF at different Q values on the low Q side of the FSDP (Figure 5-7a,b) and on the maximum (Figure 5-7c), which has been investigated during the temperature dependent measurements. The dynamics is stationary at all Q values. This contrasts the dynamics in metallic glasses, where intermittent or continuous aging is observed on the atomic level (see chapter 4) [52,219,228,233,234].

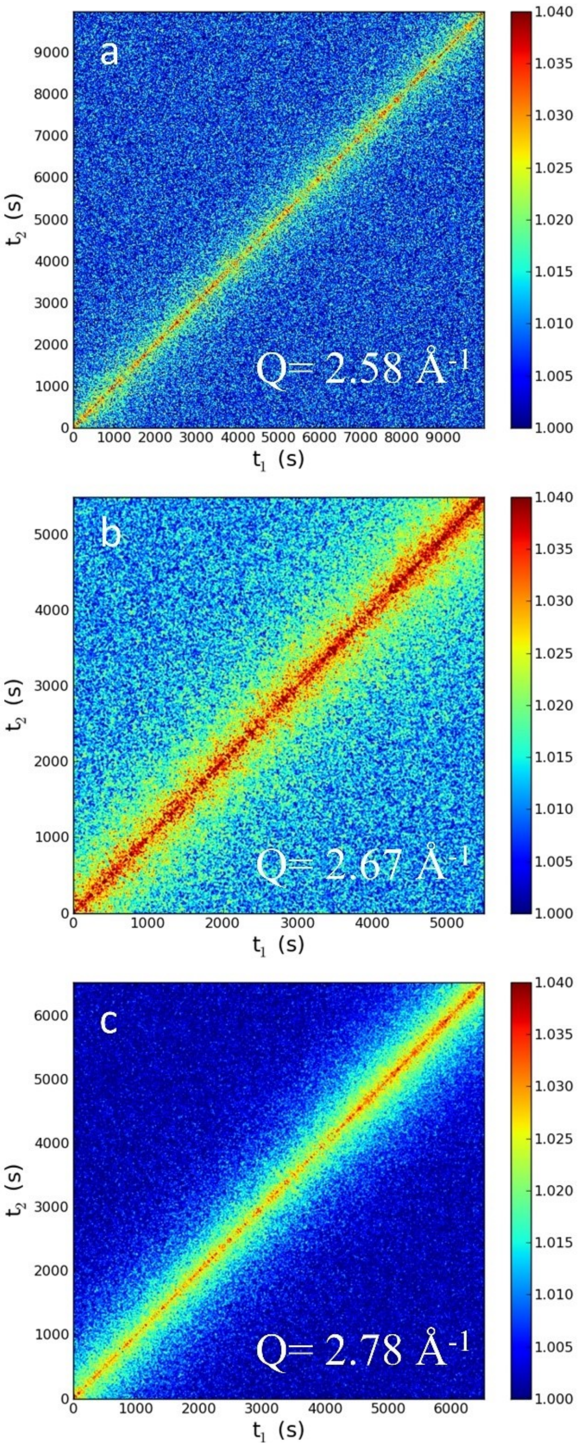

Figure 5-7: Two-times correlation function at 385.5 K for three different Q values (2.58 $Å^{-1}$ (a), 2.67 $Å^{-1}$ (b), 2.78 $Å^{-1}$ (c)). The dynamics behaves stationary during the entire measurement.

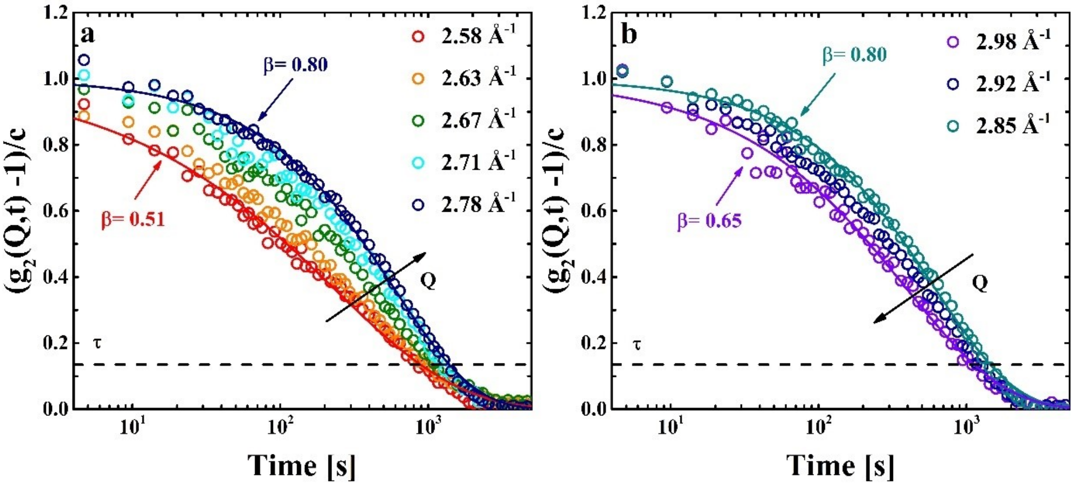

Figure 5-8: Normalized intensity autocorrelation functions for the low (a) and the high (b) Q side of the FSDP.

The decreasing intensity of the signal from Figure 5-7c to Figure 5-7a is due to the lower scattered signal when moving away from the FSDP. The fluctuations in the TTCF are a result of the heterogenous dynamics in supercooled liquids, e.g. [44,48,213], which are caused by an increasing cooperativity as shown in the previous section in the light of dynamic susceptibility.

The intensity auto-correlation functions determined at the eight different wave vectors Q are shown in Figure 5-8. Figure 5-8a illustrates intensity auto-correlation functions on the low Q side, whereas Figure 5-8b shows the intensity auto-correlation functions on the high Q side of the FSDP. As can be seen from Figure 5-8a, the dynamics depends strongly on the wave vector. When departing from the FSDP, the shape parameter changes from $\beta(Q)$= 0.80±0.02 at 2.78 Å^{-1} to 0.51±0.02 at 2.58 Å^{-1}. This change of approximately 40 % is significant considering the small change in Q of only 0.2 Å^{-1}. The distinct Q dependence of the shape parameter contrasts the behavior observed in the glassy state of metallic glass-formers, where the highly compressed shape parameter has been found to be independent of Q around the FSDP [235]. The correlation between structure and the dynamics can be seen in Figure 5-9a-c, where the S(Q) around the FSDP (a) is shown along with the structural relaxation time τ (b) and the shape parameter β (c). All data are fitted with a pseudo-Voigt function (lines).

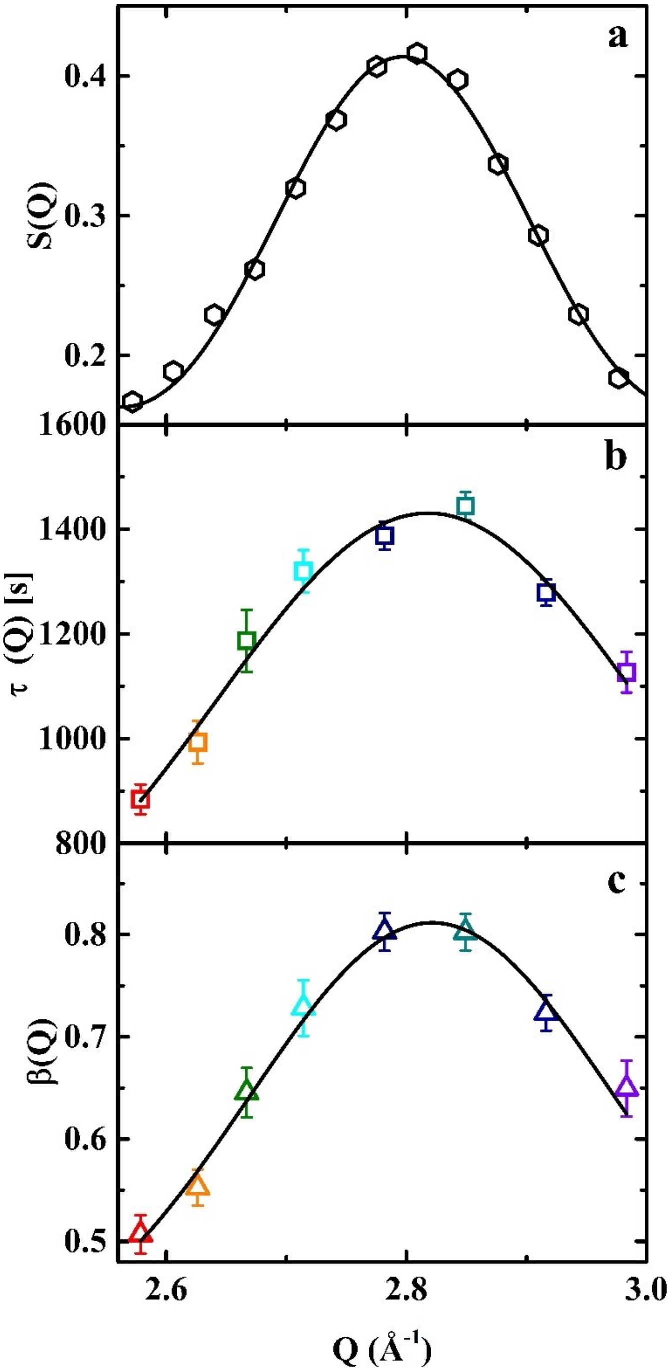

Figure 5-9: (a) Q dependence of the static structure factor S(Q), (b) the relaxation time τ, (c) the shape parameter β. τ and β follow the S(Q) in phase. The colors in (b) and (c)correspond to Figure 5-8.

As can clearly be seen, τ and β follow the shape of the S(Q) around the FSDP. τ shows a maximum at the FSDP and β indicates a pronounced narrowing of the relaxation time spectrum at the FSDP. This is a clear indication for de Gennes narrowing due to an increasing cooperativity when approaching the length scale of the next neighbor distances [201,210]. The cooperativity implies that the most stable configurations with the longest relaxation time are found on the length scale of the FSDP leading to a more homogenous relaxation time spectrum. τ and β are codependent parameters. To account for the β dependence of τ, the mean relaxation time <τ> is calculated as $\langle\tau(Q)\rangle = \Gamma\left(\frac{1}{\beta(Q)}\right)\frac{\tau(Q)}{\beta(Q)}$, where Γ is the Gamma function [30]. Figure 5-10 shows <τ> as a function of Q, which reflects the typical increase towards small Q values as larger length scales are probed. At high temperatures <τ> ~ Q^{-2} as diffusive motion is present [236–238] with β= 1. At low temperatures the diffusive motion becomes less dominant in the Q range around the FSDP, where instead cooperative atomic motion is present as can be seen from simulations e.g. [202,239], and experiments, e.g. [196,207,239]. The dashed line in Figure 5-10 describes the Q^{-1} dependence of <τ> in the measured Q range, which is an effect of the large distribution of the collective motion to the dynamics in the observed Q range.

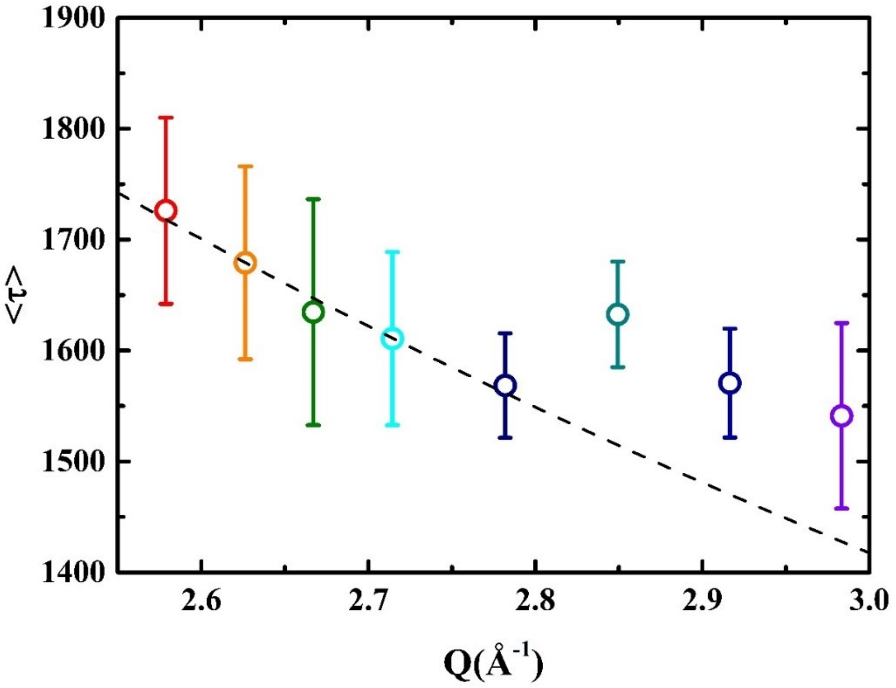

Figure 5-10: <τ> as a function of Q. The dashed line describes the Q^{-1} dependence of <τ> The colors correspond to the colors in Figure 5-8 and Figure 5-9.

5.1.6 Connection between supercooled and stable liquid

In the following section, the relaxation time results from the XPCS measurements are compared to different measurements performed in the supercooled liquid and stable liquid state. In the supercooled liquid just above T_g, the XPCS measurements are complemented by T_g shift, TMA and DMA measurements (see methods).

As discussed above, the material is equilibrated in the supercooled liquid state between 396 K and 380 K during the quasi-static cooling protocol. Figure 5-11 shows the structural relaxation time of the liquid as a function of temperature, determined from $g_2(Q,t)$, measured on melt-spun ribbons in XPCS. As can be seen, the temperature dependence of the dynamics changes at 389 K. The two regimes are fitted with the VFT function.

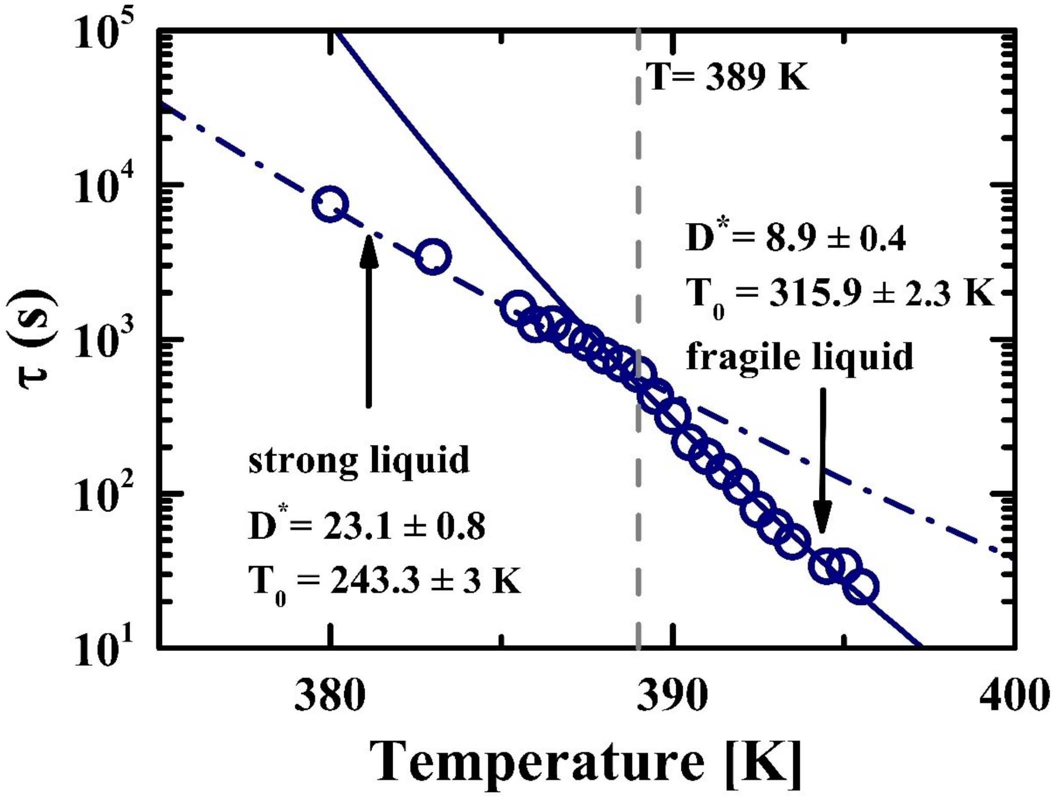

Figure 5-11: Structural relaxation time as a function of temperature determined from XPCS measurements on melt-spun ribbons. The data show a clear dynamic crossover at 389 K (dashed line). The two regimes are fitted with a VFT function (lines). The figure is reproduced from [234].

They show very different fitting parameters. The low temperature regime exhibits strong behavior with D*= 23.1±0.8 and T_0= 243.3±3 K. The high temperature regime exhibits fragile behavior with D*= 8.9±0.4 and T_0= 315.9±2.3 K.

This difference is significant. The fragile behavior is one of the most fragile behaviors ever observed for a metallic glass-forming liquid [67,68]. In Zr-based metallic glass-forming systems, for example, such a fragile behavior is typically detected in the stable liquid above the LLT [3,82,97] above T_l. The strong behavior is comparable to values observed for the strongest metallic glass-formers in the viscosity range around their T_g [67,70].

The results on the atomic level from the XPCS measurement are flanked with macroscopic measurements using DMA, T_g shift and TMA.

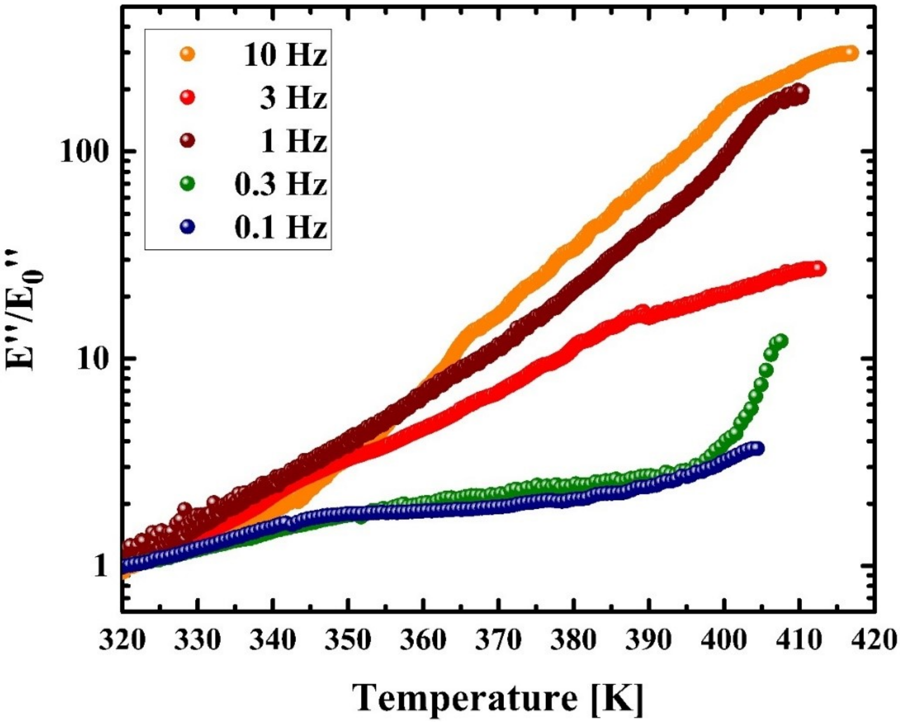

Figure 5-12: Normalized loss modulus for five different frequencies measured in DMA. The loss modulus exhibits a maximum (end of each curve) at the temperature where the relaxation time of the material fits to the excitation frequency so that the excitation is damped. With increasing frequency increases the temperature at which the loss modulus maximizes. As the machine was only temperature calibrated, the absolute value of the loss modulus is not reliable.

Figure 5-12 illustrates the DMA measurements from which the structural relaxation time is calculated as described in section 3.6. From these measurements the relaxation time at five different temperatures can be determined and compared to the XPCS results. The DMA provides macroscopic measurements and therefore information on the relaxation time of the whole melt-spun ribbon, which is measured.

The T_g shift measurements are shown in Figure 5-13. From these measurements, the structural relaxation time at three different temperatures can be determined as described in section 3.3.2. It provides information on the relaxation time of the bulk samples, which were measured.

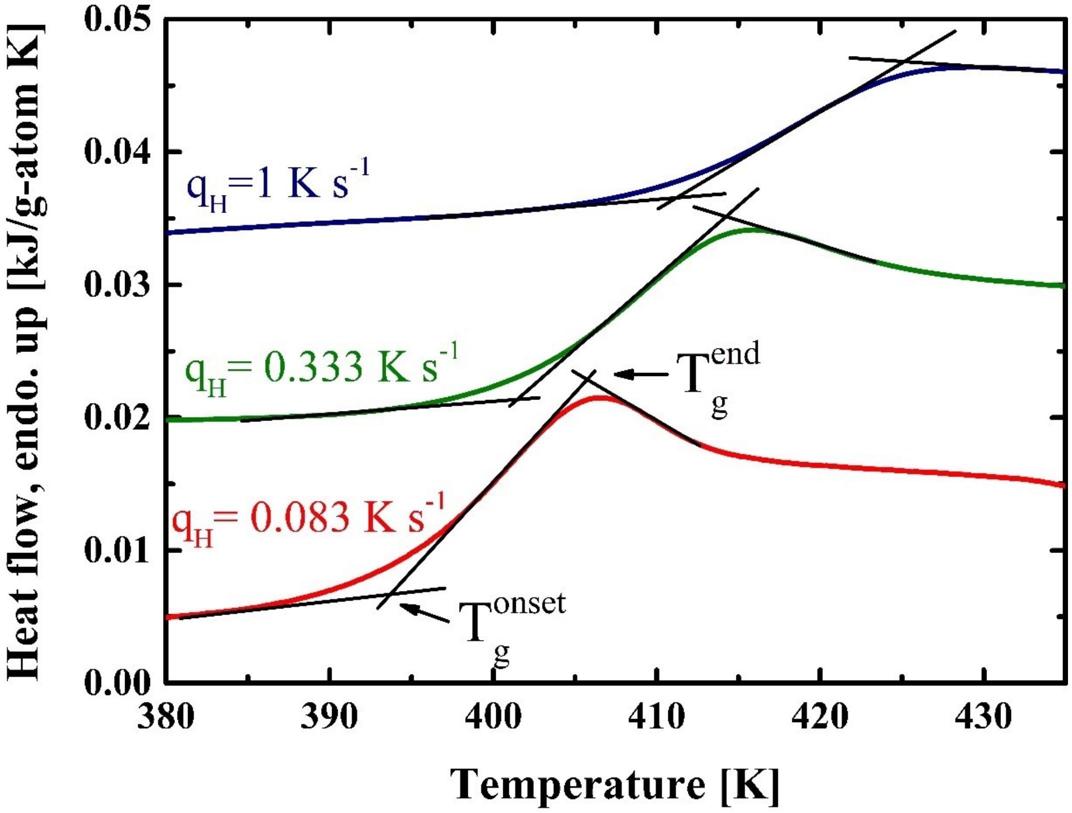

Figure 5-13: T_g shift experiments with three different heating rates of the $Au_{49}Cu_{26.9}Si_{16.3}Ag_{5.5}Pd_{2.3}$ alloy. The curves are shifted vertically for better clarity.

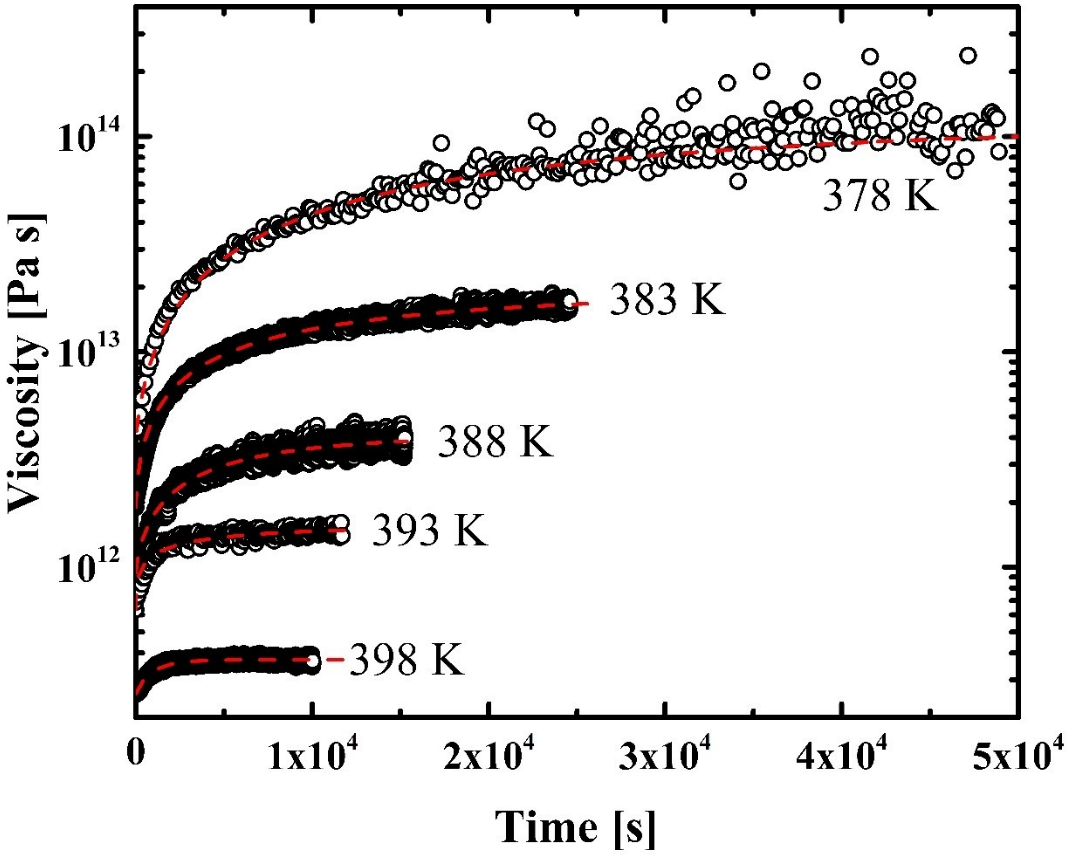

Figure 5-14: Selection of isothermal three-point beam bending measurements at 5 different temperatures. The equilibrium viscosity is determined using a KWW stretched exponential equation.

The TMA measurements are shown in Figure 5-14. The equilibrium values of the isothermal viscosity measurements are determined as described in section 3.4. The measurement provides information on the macroscopic viscosity of the bulk samples, which were measured. The equilibrium viscosities of the bulk samples are converted into relaxation times. Figure 5-15 unites the relaxation times determined from XPCS (blue circles) with DMA measurements on ribbons (blue triangles), T_g shift experiment (red crosses) and three-point beam bending measurements (red squares). The viscosity measurements from three-point beam bending align perfectly with the XPCS results below 389 K, where strong dynamic behavior is found. The viscosity data are converted into relaxation times using the relation $\eta = G_{\tau\text{-}\eta} \times \tau$ (see e.g. [68]). The constant of proportionality $G_{\tau\text{-}\eta}$, which is the high frequency shear modulus, is determined to be $G_{\tau\text{-}\eta}$, of 4.5×10^8 Pa [219]. The VFT fit to the relaxation times converted from the viscosity data and the XPCS data

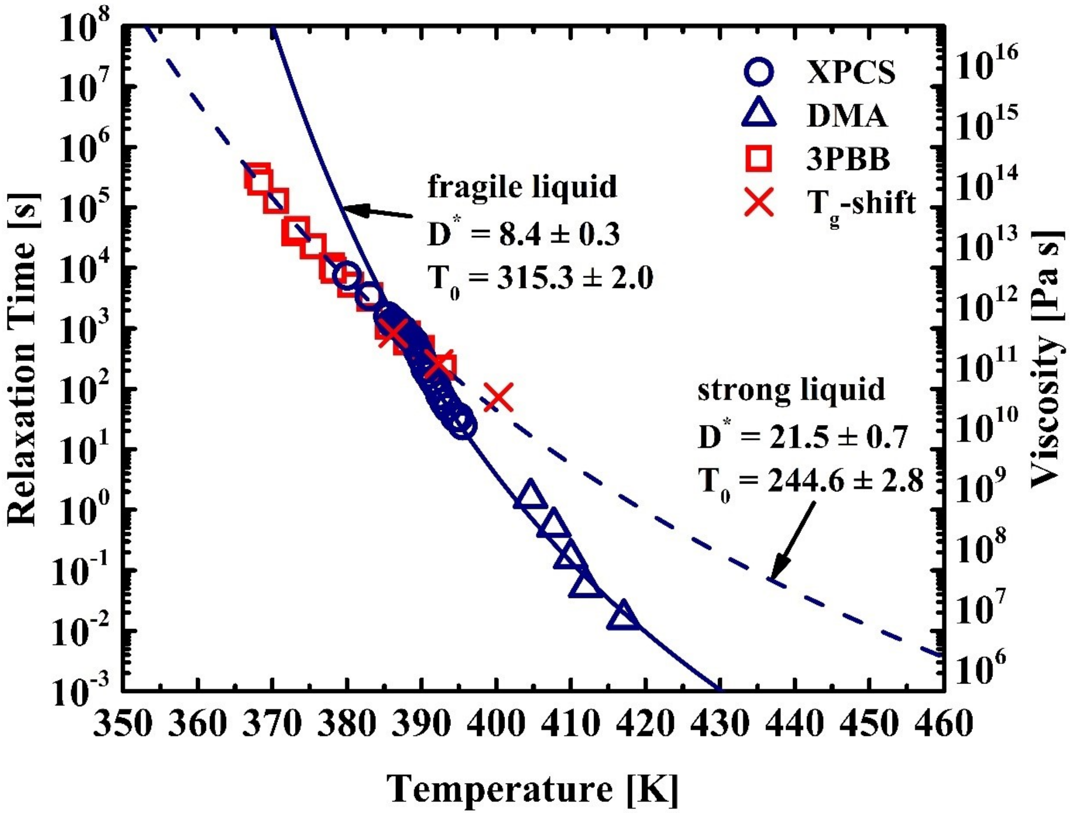

Figure 5-15: XPCS results from Figure 5-11 (blue circles) extended with results from 3PBB (red squares) and T_g-shift (red crosses) on bulk samples and DMA measurements on ribbons (blue triangles). As can be seen, the viscosity and the T_g shift data of the bulk samples align nicely with the strong liquid regime measured in XPCS on melt-spun ribbons, whereas the DMA measurements align with the fragile regime.

below 389 K gives $D^* = 21.5 \pm 0.7$ and $T_0 = 244.6 \pm 2.8$ K, which is similar to the fit of the XPCS results, proofing that the same liquid phase is probed with both techniques. The relaxation times determined from the DMA measurements align nicely with the fragile regime determined from XPCS. The VFT fit to the fragile XPCS data above 389 K and the DMA measurements gives $D^*= 8.4 \pm 0.3$ together with $T_0= 315.3 \pm 2.0$ K. The fit is very similar to the fit, which is based only on the XPCS data, and the measured dynamics clearly belong to the same liquid phase.

Viscosity measurements in the stable liquid above the melting point T_m= 614 K complete the measurements of the dynamics in the $Au_{49}Cu_{26.9}Si_{16.3}Ag_{5.5}Pd_{2.3}$ metallic glass-forming liquid. Figure 5-16 shows the results of the viscosity measurement using Couette rheometry.

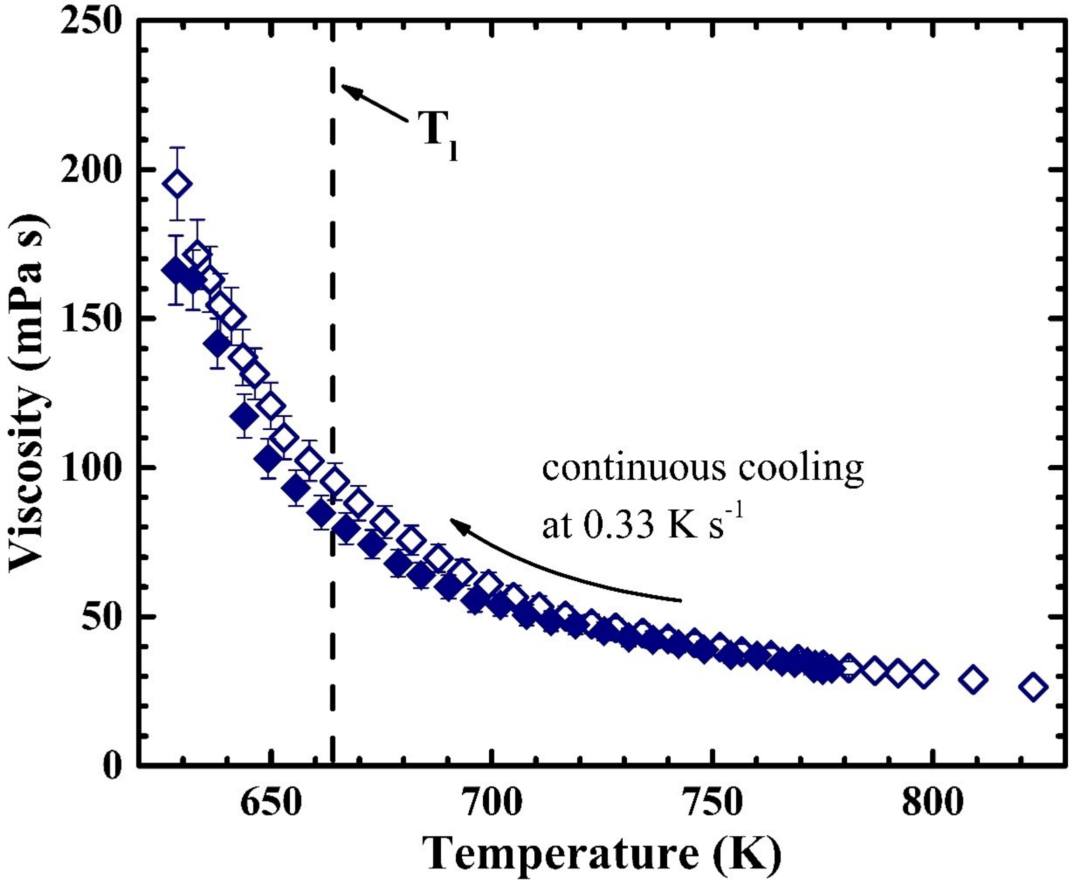

Figure 5-16: High temperature viscosity measurement upon cooling with 0.33 K s^{-1} in the equilibrium liquid above the liquidus temperature and in the supercooled liquid with an undercooling of up to 36 K using Couette rheometry. At 36 K undercooling below the liquidus temperature (T_l) the material crystallizes.

The viscosity can be determined upon cooling with a constant rate of 0.33 K s^{-1} starting at 830 K in the stable liquid down to 628 K which is 36 K below the liquidus temperature (T_l). Two data sets show the reproducibility of the measurements. Figure 5-17 connects the Couette measurements, which have been converted into relaxation times using $G_{\tau\text{-}\eta}$, with the XPCS and DMA measurement. The three techniques cover different ranges of relaxation times from 10^3 s down to 10^{-10} s and deliver a congruent picture of the dynamics.

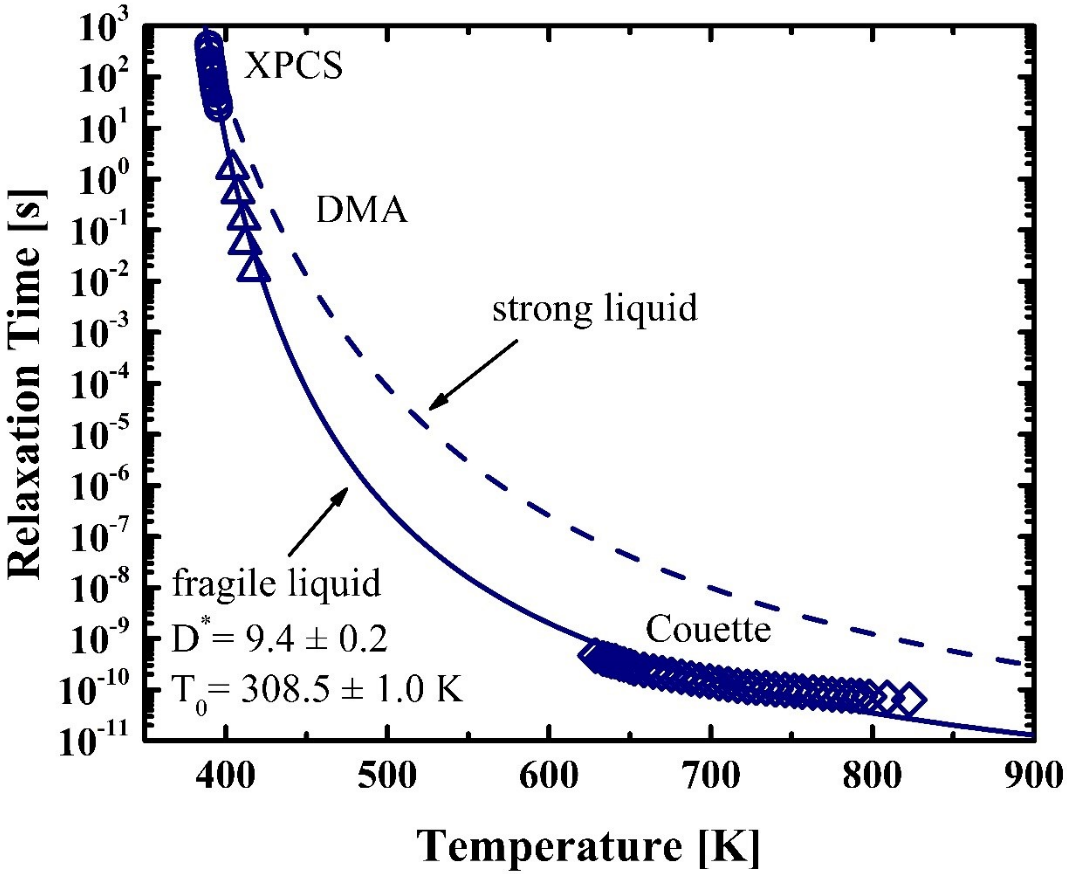

Figure 5-17: VFT fit to data acquired by XPCS (blue circles), DMA (blue triangles) and Couette rheometry (blue diamonds). The fit shows the fragile behavior of the liquid above 389 K.

The results are fitted with the VFT equation resulting in a $D^* = 9.4 \pm 0.2$ and $T_0 = 308.5 \pm 1.0$ K. The fit is very good considering the large range of relaxation times of 13 orders of magnitude. The fit parameters are in good agreement with the ones determined only in the deeply supercooled liquid. The nice fit between high temperature and low temperature data indicates that the three techniques XPCS, DMA and Couette rheometry probe the dynamics of the same fragile liquid.

The results indicate that bulk samples behave strong, whereas melt-spun ribbons show fragile liquid behavior.

5.2 The liquid-liquid transition

5.2.1 Dynamical signature of the LLT

The bend in the relaxation time data at 389 K occurs in the liquid state, as shown in Figure 5-11 and Figure 5-15. Therefore, the bend cannot be associated to a freezing of the liquid. As already mentioned, the change in the dynamics is significant as the change of the D^* parameter from more than 20 for the region below 389 K and less than 10 above is in good agreement with the values measured in Zr-based metallic glass-forming liquids below and above a liquid-liquid phase transition (LLT) [80,97]. This fact suggests the occurrence of such a LLT in the $Au_{49}Cu_{26.9}Si_{16.3}Ag_{5.5}Pd_{2.3}$ metallic glass-forming liquid in the deeply supercooled liquid just above the glass transition temperature. The transition can only be seen in-situ during very slow cooling in XPCS as the glass transition, which at standard cooling rates obscures the LLT, is shifted to lower temperatures. Other techniques can show the change in the dynamics only ex-situ. The DMA measurements which were performed at hyper-quenched ribbons show the dynamics of the fragile liquid as this is frozen-in during the fast cooling. The three-point beam bending is performed on bulk samples, which experienced a slower cooling rate, allowing the liquid to transform either directly during the casting process or later during aging into the strong liquid phase. For this reason, the three-point beam bending delivers the dynamics of the strong phase. The change in the dynamics is only a signature of the LLT and must be associated with a calorimetric signature and structural changes. These two fields are discussed in the following sections.

5.2.2 Calorimetric signature of the LLT

A LLT must be visible in the thermodynamic functions of the system, when it is considered as a phase transition. When looking at the specific heat capacity of a system, a first order transition causes a singularity, a second order transition leads to a discontinuity at the transition temperature. Wei et al. [3] and Stolpe et al. [82] have shown that the LLT in Zr- based glass-forming liquids exhibit an endothermic peak in C_p. In the present system, the enthalpic signature of the LLT is found in the glassy state for standard cooling rates. As the signal of the transition smears out and vanishes in the noise of the measurement if the sample is cooled with the quasi-static cooling protocol used during synchrotron measurements at the ESRF, the signal can only be found in ex situ measurements. By enthalpy recovery measurements after isothermal treatment for different times at several temperatures below T_g, our research group could show that the two liquid phases possess different heat capacities as described in section 4.2.1 [219]. Figure 5-18 shows the heat capacity of the glassy, crystalline, supercooled and liquid state (open squares, triangles, red diamonds and black circles respectively). These data show a step of the specific heat capacity at T_g of approximately 20 J (g-atom K)$^{-1}$, which corresponds to a rather fragile liquid (see e.g. [51]). But when annealing the material below 375.5 K for a long time, the released enthalpy is significantly lower than above. This can be explained by a significant decrease of the specific heat capacity at lower temperatures, which is associated to the LLT from a fragile high temperature liquid with a larger specific heat capacity to a strong low temperature liquid with a smaller specific heat capacity. The heat capacity values of the two different liquids are shown as grey and blue diamonds in Figure 5-18.

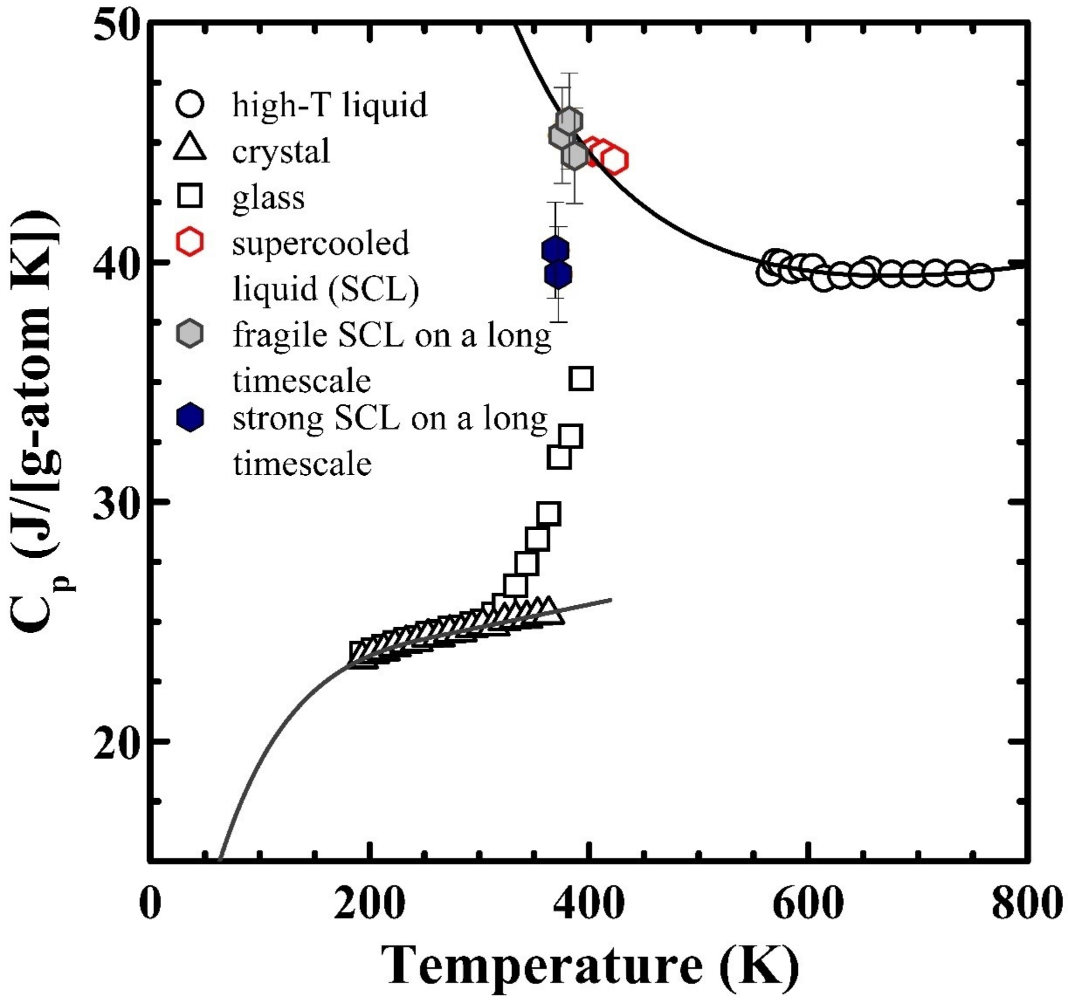

Figure 5-18: The molar heat capacity of the $Au_{49}Cu_{26.9}Si_{16.3}Ag_{5.5}Pd_{2.3}$ alloy as a function of temperature, measured with the step method for the glassy (squares), the crystalline (triangles), the supercooled liquid (circles) and liquid state (hexagons). The alloy exhibits an increase of the molar heat capacity of about 20 J (g-atom K)$^{-1}$ from the glass into the liquid upon heating. Through enthalpy recovery measurements after different annealing times at several temperatures, the molar heat capacity can be determined (see section 3.3) and is given by the grey filled circles for the fragile and by the blue filled circles for the strong liquid. The figure is reproduced from [219].

5.2.3 Structural evolution in the supercooled liquid, the stable liquid and during the LLT

Beside the dynamics and thermodynamics of the liquid, the structural evolution has been investigated using XRD in the stable liquid as well as in the supercooled liquid. The supercooled liquid state has been investigated using the same quasi-static cooling protocol, which has been used during the XPCS measurements. The structure of the stable liquid is investigated during continuous cooling with 0.33 K s^{-1}.

Figure 5-19 shows the $(Q_1^{max}(T_{ref})/Q_1^{max})^3$ in the glass, the deeply supercooled and the stable equilibrium liquid above the liquidus temperature T_l. At low temperatures, bulk samples, which were produced with different cooling rates, were heated with 0.33 K s^{-1} from the glassy state into the supercooled liquid. Both samples exhibit a significant change of the slope of $(Q_1^{max}(T_{ref})/Q_1^{max})^3$ at the glass transition which occurs for the two samples at different temperatures due to the different cooling rate upon casting the samples. The most salient feature is the large difference in the temperature dependence of $(Q_1^{max}(T_{ref})/Q_1^{max})^3$ in the deeply supercooled liquid and in the stable equilibrium liquid. This large difference is in stark contrast to what is observed in Zr- based metallic glasses. There, the slope of $(Q_1^{max}(T_{ref})/Q_1^{max})^3$ is very similar close to the glass transition and in the high temperature liquid [3,82], despite the occurring liquid-liquid transition. For this reason, the change in the slope seems not to be associated to a liquid-liquid transition. It could be the result of a continuous change in this value in the same liquid structure. If this is the case, the structural data agree with the dynamic measurements on the fragile phase observed above 389 K in XPCS, DMA and Couette rheometry (see section 5.1.6)

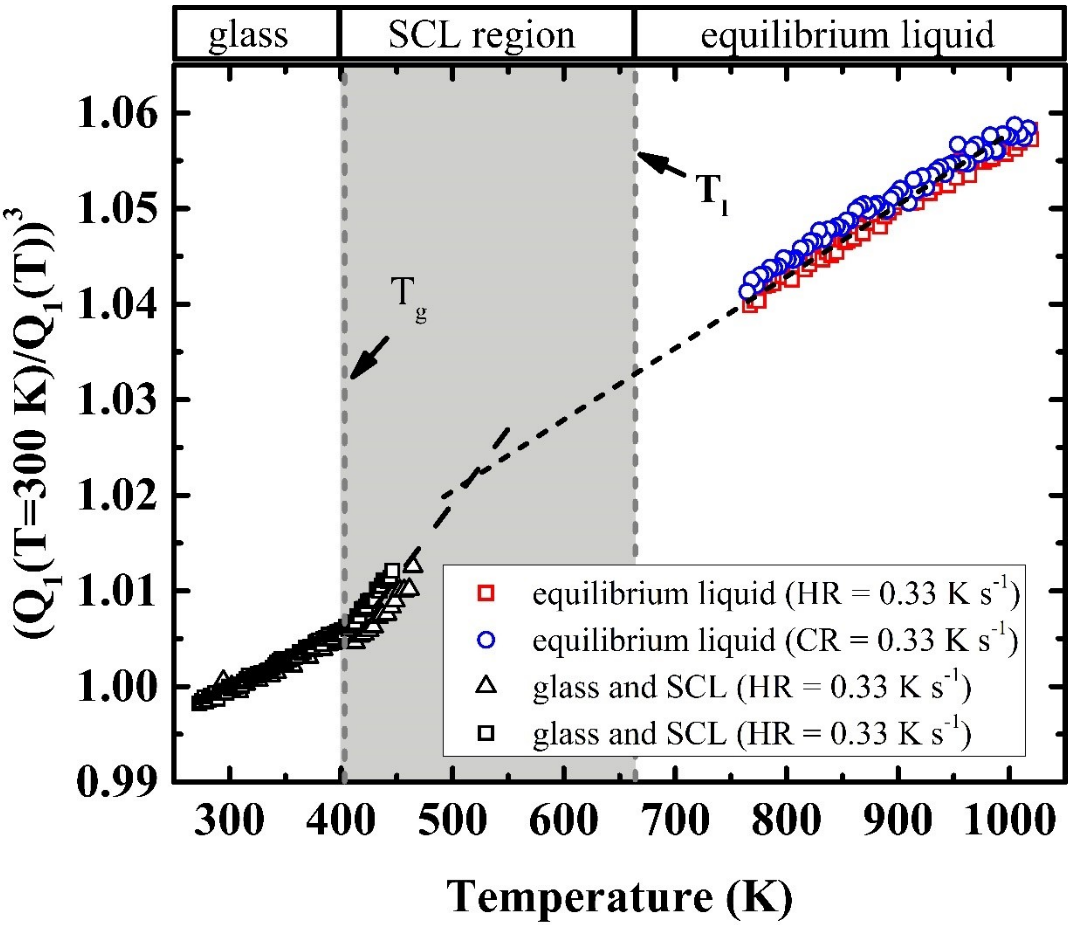

Figure 5-19: $(Q_1^{max}(T_{ref})/Q_1^{max})^3$ in the glass and in the deeply supercooled liquid region (triangles and squares) and in the equilibrium liquid (blue circles and red squares). The temperature dependence of $(Q_1^{max}(T_{ref})/Q_1^{max})^3$ is significantly steeper in the supercooled liquid than in the equilibrium liquid as indicated by the dashed lines [230].

The quasi-static cooling protocol in the ultra-viscous state, which was applied to reveal the dynamical crossover at 389 K by shifting T_g to lower temperatures using XPCS, was reproduced to investigate the structural evolution during the crossover. Figure 5-20 shows the evolution of $(Q_1^{max}(T_{ref})/Q_1^{max})^3$ as a function of temperature upon quasi-static cooling as blue diamonds. As can be seen upon cooling in the supercooled liquid, $(Q_1^{max}(T_{ref})/Q_1^{max})^3$ shows an anomalous increase, which cannot be associated to a glass transition for several reasons: (a) the glass transition is expected to occur at 380 K, so well below the start of the anomalous increase due to the slow cooling protocol (see Figure 5-3).

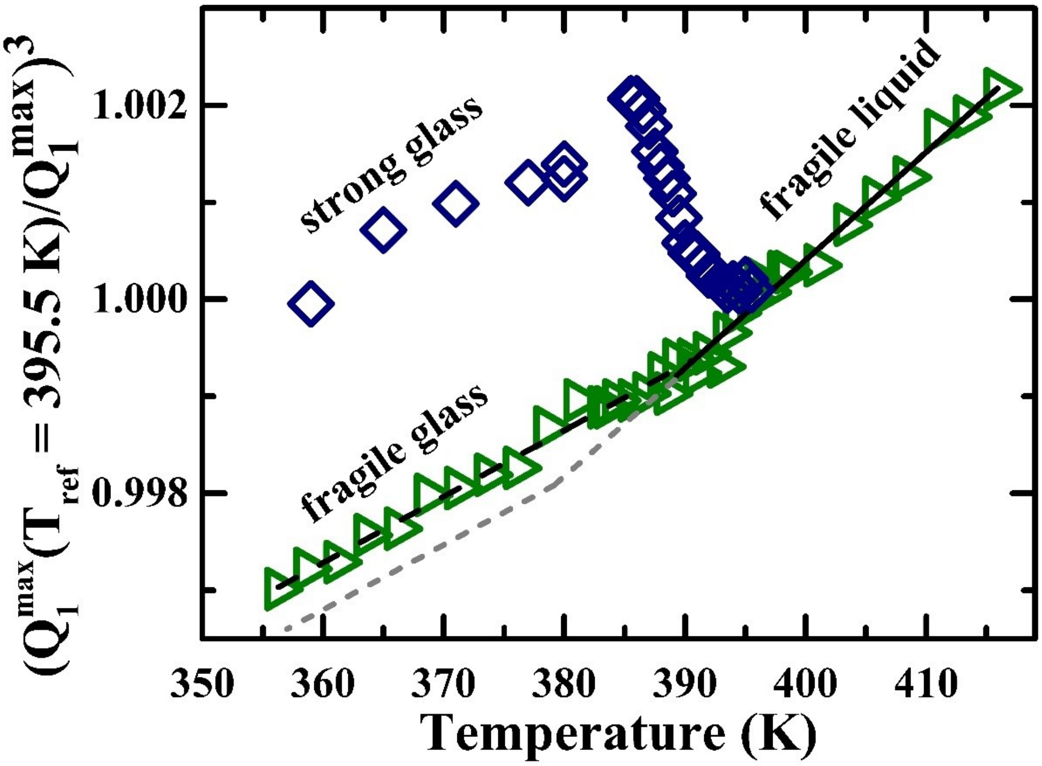

Figure 5-20: Changes in $(Q_1^{max}(T_{ref})/Q_1^{max})$ as a function of temperature. The changes which occur during the quasi-static cooling are shown as blue diamonds. The changes during cooling with a constant rate of 1.5 K min^{-1} are shown as green triangles. The expected progress for a standard glass transition with the cooling rate of the quasi-static cooling protocol is shown as grey dashed line. The figure is reproduced from [234].

(b) The appearance of a glass transition is completely different. As can be seen from the green triangles in Figure 5-20, T_g occurs at 390 K for the applied cooling rate of 1.5 K min^{-1} and results in a kink from a steep to a shallower temperature dependence. For this reason, at T_g for the applied quasi-static cooling such a kink would be expected at 380 K as indicated by the grey dashed line.

The different behavior in the peak position of the FSDP of S(Q) during the quasi-static cooling and the continuous cooling with 1.5 K min^{-1} is visualized in Figure 5-21. It is clearly visible, that the peak position increases between 396 K and 385 K upon cooling continuously with 1.5 K min^{-1} (left panel), whereas the opposite is happening during the quasi-static protocol (right panel).

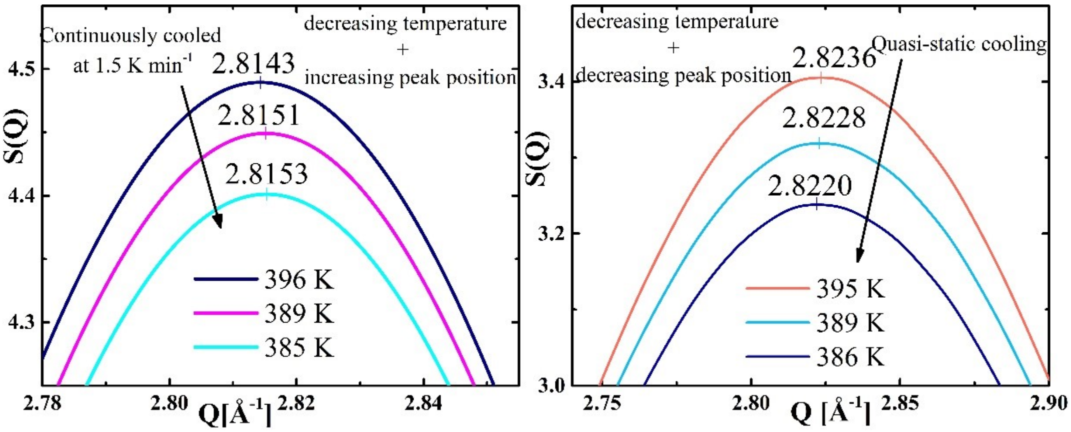

Figure 5-21: Evolution of the peak position of the FSDP during continuous cooling with 1.5 K min^{-1} (left panel) and upon quasi-static cooling (right panel) between 396 K and 385 K, where the LLT occurs. When the liquid is cooled fast enough, the LLT is preempted by the glass transition and the peak position increases with decreasing temperature as expected due to the thermal contraction during cooling (left panel). If the material is cooled quasi-statically, the glass transition is shifted to lower temperatures and the material undergoes a LLT which results in a decreasing peak position upon cooling (right panel).

The increase in $(Q_1^{max}(T_{ref})/Q_1^{max})^3$ is not the signature of T_g but of the liquid-liquid transition from a fragile to a strong liquid, which was already suggested from dynamical and enthalpy recovery experiments. The same kind of discontinuity in $(Q_1^{max}(T_{ref})/Q_1^{max})^3$ has been observed during a LLT in a Zr-based alloys by our research group [3] and is illustrated in Figure 2-20.

5.2.4 The glass transition of the strong phase

T_g of the new built strong phase occurs below 385.5 K where it freezes upon cooling with 7 K min^{-1} into a glass, which has a comparable temperature dependence of $(Q_1^{max}(T_{ref})/Q_1^{max})^3$ as the glass of the fragile liquid frozen-in at 390 K upon faster cooling (see Figure 5-20). The material behaves like a glass below 385.5 K.

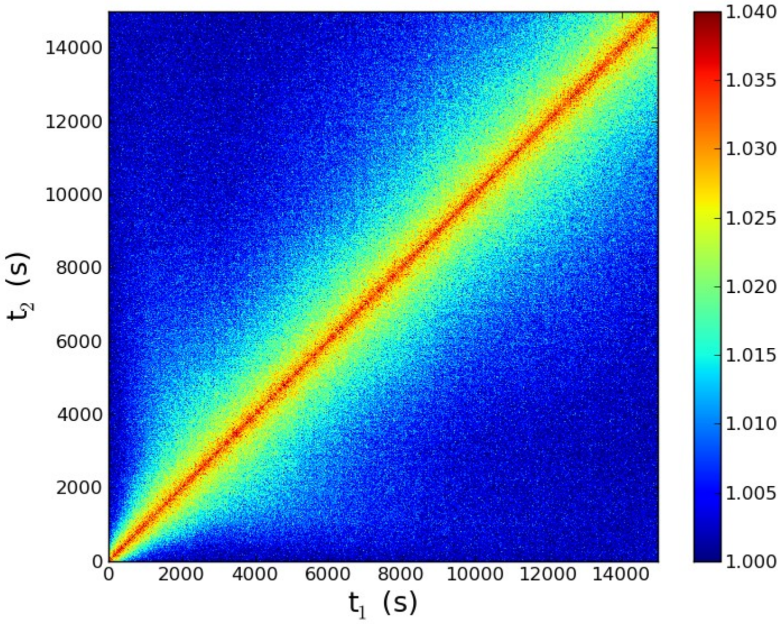

Figure 5-22: TTCF at 380 K. The diagonal broadens for about 2800 s before it stays constant. The figure is reprinted from [234].

As can be seen from Figure 5-22, the dynamics is not stationary anymore. After cooling the material from 385.5 K to 380 K with 7 K min^{-1}, the TTCF broadens, which is a clear sign of aging. The frozen liquid starts to evolve towards the supercooled liquid and equilibrates after approximately 2800 s. The same can be seen in the structure of the material. Figure 5-23 illustrates the evolution of $(Q_1^{max}(t_{initial})/Q_1^{max}(t))^3$ at 380 K after cooling from 385.5 K. Analog to the dynamics, $(Q_1^{max}(t_{initial})/Q_1^{max}(t))^3$ decreases due to aging for about 2500 s before it stays constant as the material has reached the supercooled liquid again.

From this observation it is clear, that the strong liquid which has been built during the liquid-liquid transition, possesses a glass transition temperature, which is very similar to the one of the fragile liquid. But as T_g is a kinetic event, a direct comparison of the glass transition temperatures of the two liquids is difficult due to the occurring liquid-liquid transition. When applying high cooling rates, the fragile liquid is frozen in. When applying low cooling rates, the LLT occurs and the strong liquid is frozen.

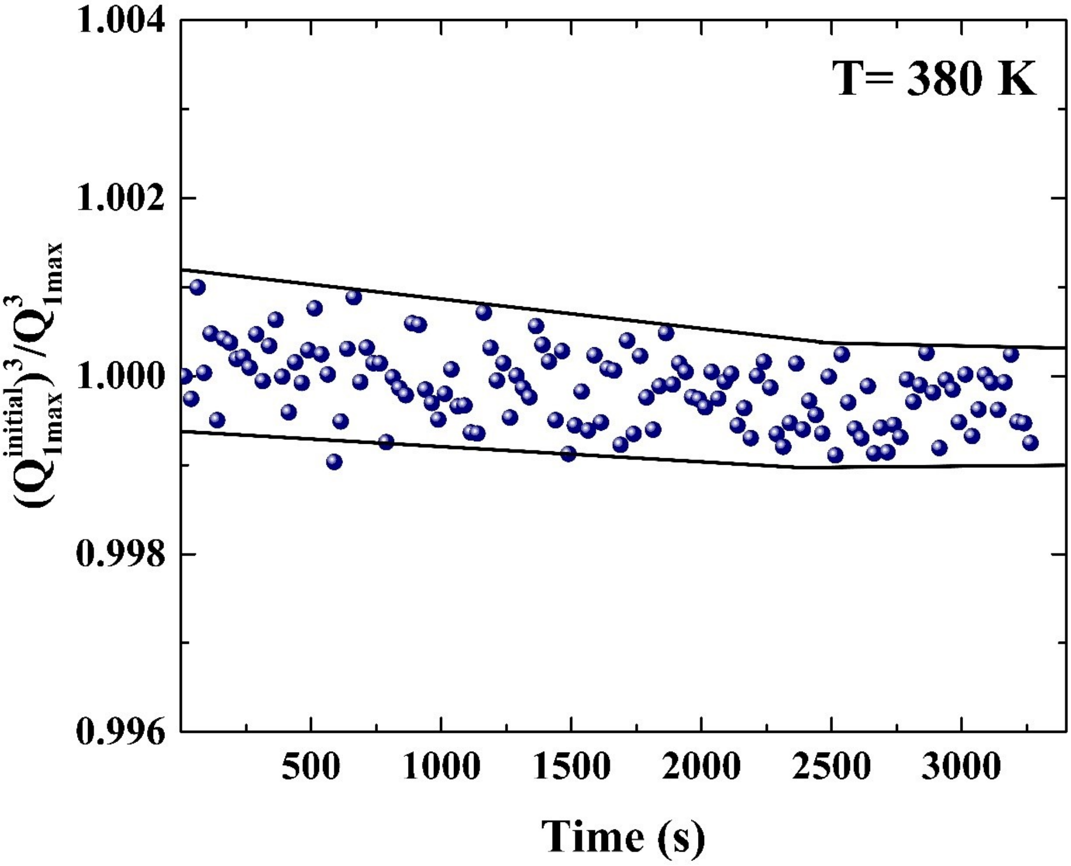

Figure 5-23: Normalized changes in the peak position of the FSDP as a function of temperature at 380 K during an isothermal measurement. The peak position changes during aging over the first 2500 s. Afterwards, the aging stops as the material has entered the supercooled liquid.

After this short parenthesis about the glass transition of the strong phase, the nature of the liquid-liquid transition is discussed in the following section.

5.2.5 The liquid-liquid transition in comparison to Zr-based alloys

The change in $(Q_1^{max}(T_{ref})/Q_1^{max})^3$ of the $Au_{49}Cu_{26.9}Si_{16.3}Ag_{5.5}Pd_{2.3}$, which is shown in Figure 5-20, is reminiscent of what has been observed during a LLT in the $Zr_{41.2}Ti_{13.8}Cu_{12.5}Ni_{10}Be_{22.5}$ glass-forming alloy upon cooling at about 830 K [3] (see Figure 2-20). Similar behavior has been observed in the $Zr_{58.5}Cu_{15.6}Ni_{12.8}Al_{10.3}Nb_{2.8}$ glass-forming alloy [82]. The slope in $(Q_1^{max}(T_{ref})/Q_1^{max})^3$ is very similar above and below the transition, with a discontinuity during the LLT. Additionally, the structural changes during the LLT in the Zr-based and the $Au_{49}Cu_{26.9}Si_{16.3}Ag_{5.5}Pd_{2.3}$ alloys are accompanied by similar changes in the dynamics in terms of fragility. In the Au-based alloy the fragility changes upon cooling from D*= 8.9±0.4 in the high temperature fragile liquid to D*= 23.1±0.8 in the low temperature strong liquid below the LLT. The Zr- based alloys exhibit changes from D*between 10-12 in the fragile to D* > 20 in the strong liquid [82,97].

Due to the dynamical and structural measurements, the transitions seem to be phenomenologically the same for the Zr- based and the Au-based alloys. But there is a difference which should be mentioned. In the Zr-based alloys, the transition occurs 400 K to 700 K above the conventional glass transition, whereas it occurs at temperatures around the glass transition in the Au-based alloy. This leads lead to completely different impact of the LLT in terms of energy. According to Tanaka [88], $T_{LLT} = \frac{\Delta E - p\Delta\tilde{v}}{\Delta S}$ (see section 2.5.1). The volume change between fragile and strong liquid can be neglected as it has been shown that no macroscopic density change is visible for Zr-based alloys [3,82]. Additionally, it has been shown, that the ΔS due to the ordering process during the LLT [77,81] is smaller for the Au- than for the Zr-based alloys [219]. As a direct consequence of the lower transition temperature, the ordering energy ΔE in the formula given above must be significantly lower in the Au- alloy than in the Zr-based alloys.

5.2.6 The order of the transition

The transition appears very differently in terms of dynamics and structure. In the dynamics, the transition occurs abruptly at 389 K, whereas the structure changes continuously between 395.5 K and 385.5 K. Within this temperature interval $(Q_1^{max}(T_{ref})/Q_1^{max})^3$ increases continuously upon cooling as a function of temperature.

Due to the long isotherms, which were performed during the quasi-static cooling protocol, there is a lot of structural information about the peak position of the FSDP and its shape, which can help to elucidate the nature of the transition.

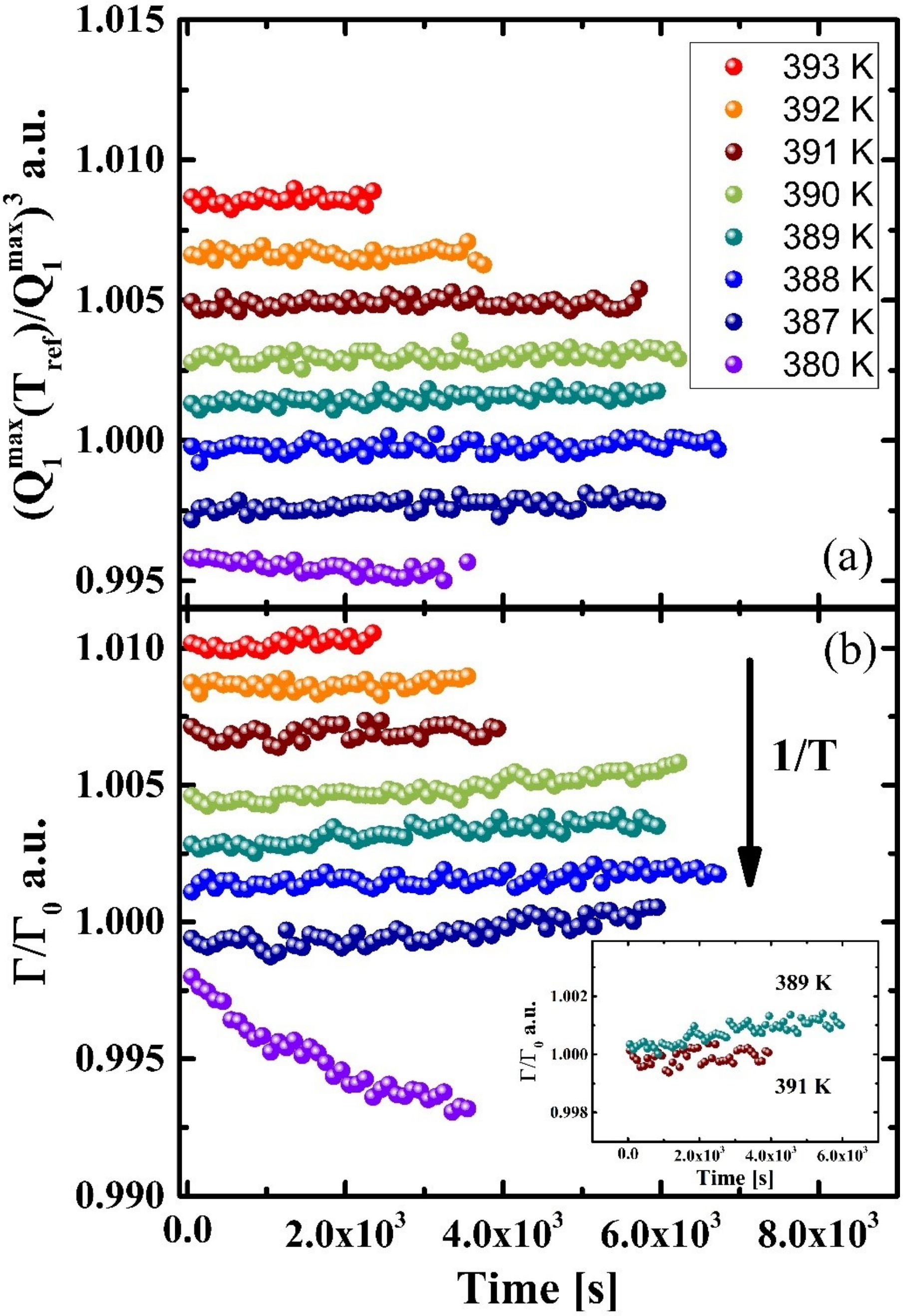

Figure 5-24: Temporal evolution of $(Q_1^{max}(T_{ref})/Q_1^{max})^3$ (a) and FWHM (b) during isotherms between 395.5 and 385.5 K. All data are vertically shifted for clarity. While $(Q_1^{max}(T_{ref})/Q_1^{max})^3$ is constant, the FWHM slightly increases with time in the crossover region. At 380 K, both parameters decrease due to the equilibration at short times from the glass.

Figure 5-24 shows the temporal evolution of $(Q_1^{max}(T_{ref})/Q_1^{max})^3$ (panel a) and the full width at half maximum (FWHM) of the FSDP (panel b) at different temperatures within the transition range and during the aging of the glass at 380 K.

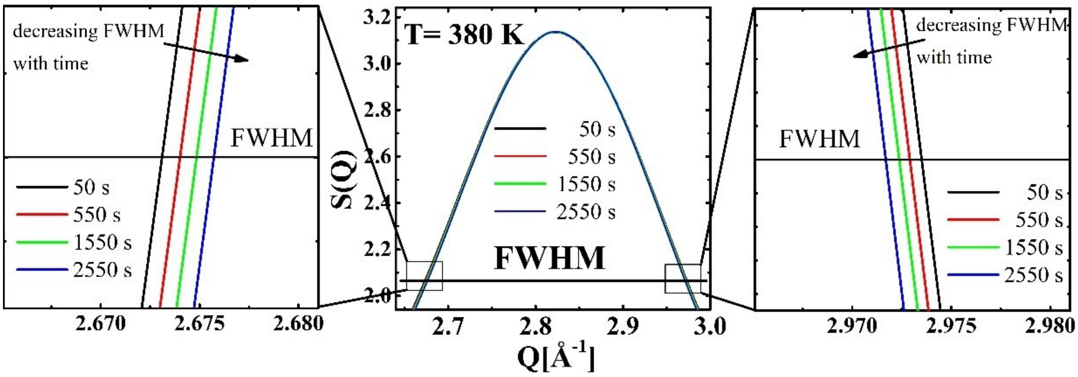

Figure 5-25: Temporal evolution of the FWHM of the FSDP at 380 K during aging of the quenched-in glass into the supercooled liquid. As can be seen the peak sharpens upon annealing indicating ordering processes in the material.

The aging behavior at 380 K is shown in purple (at the bottom of each panel) to relate the structural changes during the isotherms in the transition region to structural changes during aging.

During aging $(Q_1^{max}(T_{ref})/Q_1^{max})^3$ decreases slightly due to densification of the material. The FWHM decreases significantly as the aging results in ordering processes as configurations, which were frozen-in on a high energy state age out leading to a sharpening of the FSDP and accordingly to a decrease in the FWHM. This decrease of the FWHM of the FSDP is illustrated in Figure 5-25. The FSDP sharpens as a function of the annealing time.

In comparison to the changes during aging at 380 K, the changes during the isotherms within the transition region from one liquid structure to the other are small. In the entire transition region $(Q_1^{max}(T_{ref})/Q_1^{max})^3$ does not change as a function of time at any temperature, indicating that the structural equilibration occurs relatively fast before the start of each measurement when the annealing temperature is reached. The development of the FWHM is different. Down to 391 K, the FWHM does not change with time and stays constant as also shown in Figure 5-26. But from 390 K downwards, the FWHM increases with time for each temperature. This is shown exemplarily in Figure 5-27 for 389 K. The FWHM increases slightly upon annealing.

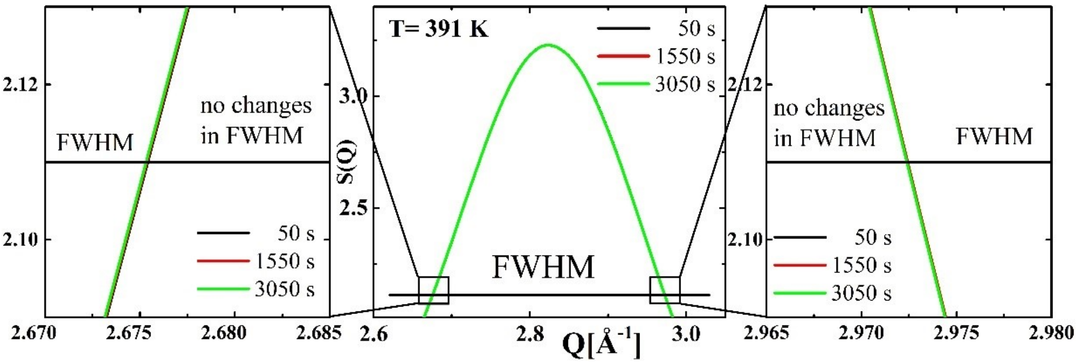

Figure 5-26: Temporal evolution of the FWHM of the FSDP at 391 K during annealing. The FSDP keeps a constant FWHM with no visible changes.

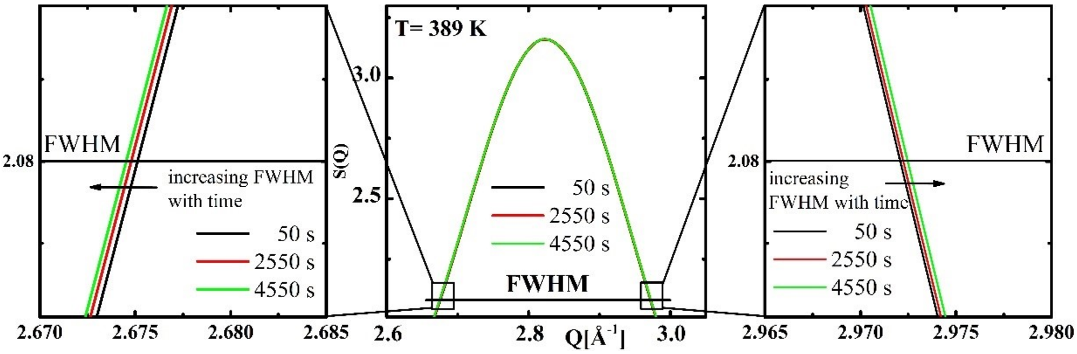

Figure 5-27: Temporal evolution of the FWHM of the FSDP at 389 K during annealing. The FSDP broadens due to structural changes during the LLT.

The fact that bulk samples behave strong and ribbons behave fragile, which has been discussed in section 5.1.6 indicates, that the bulk material has transformed upon cooling during the processing of the samples, whereas in melt-spun material the fragile liquid is frozen-in and the LLT is suppressed. This strengthens the idea that a first order phase transition is observed as an undercooling of the fragile phase below this temperature is possible.

When looking at the structural changes during the transition upon quasi-static cooling (see Figure 5-20) the increase in $(Q_1^{max}(T_{ref})/Q_1^{max})^3$ occurs over a temperature interval of 10 K. Within this temperature range $(Q_1^{max}(T_{ref})/Q_1^{max})^3$ does not change with time during the isothermal annealing (see Figure 5-24). This fact suggests a transition through a region where both liquid structures coexist in thermodynamic equilibrium. If that would not be the case and only the strong phase would be stable, the transformation should continue also during the isotherms. The increase in the FWHM in the transition region (see Figure 5-24b) indicates that there are smaller structural rearrangements going on during the isotherms, which do not affect the density. The abrupt change in the dynamics (see Figure 5-11) occurs at 389 K in the middle of the structural transition range between 395.5 and 385.5 K. The bend could occur at a single temperature as at this point the strong liquid becomes dominant in terms of dynamics leading to the stronger behavior at lower temperatures. But there is a strong argument, which opposes this interpretation. Even if the two liquids possess the same density, the intensity auto-correlation function should exhibit a two-step behavior, when the dynamics of two liquids with different relaxation times is studied at the same time, which is not the case.

Therefore, the order and nature of the liquid-liquid transition, is difficult to determine. There are several indications that the transition is a first order transition, but whether it passes through a two-phase region remains unclear as well as the critical temperature of the transition (see next section 5.2.7).

Figure 5-28 shows the time-temperature-transition (TTT) diagram of the $Au_{49}Cu_{26.9}Si_{16.3}Ag_{5.5}Pd_{2.3}$ alloy. The crystallization events in the TTT diagram were determined using a FDSC. The crystallization behavior was investigated isothermally by cooling the material with 6000 K s^{-1} from 823 K through the liquidus temperature at 664 K [161] to the desired temperature [218]. The results fit very well with the results from Pogatscher et al. [217] concerning the crystallization behavior and the critical cooling rate of approximately 600 K s^{-1}. Wang et al. [171] determined the critical cooling rate to be 1000 K s^{-1} using a very small sample mass of around 250 ng. The mass, which is used, influences the crystallization behavior. The smaller the sample, the higher the critical cooling rate, which is needed to circumvent the crystallization as surface effects, which facilitate crystallization, become more important [217]. This is the reason, why the cooling curve of the amorphous 5 mm rod, which has a sample mass of several grams cuts the crystallization nose of the FDSC measurements.

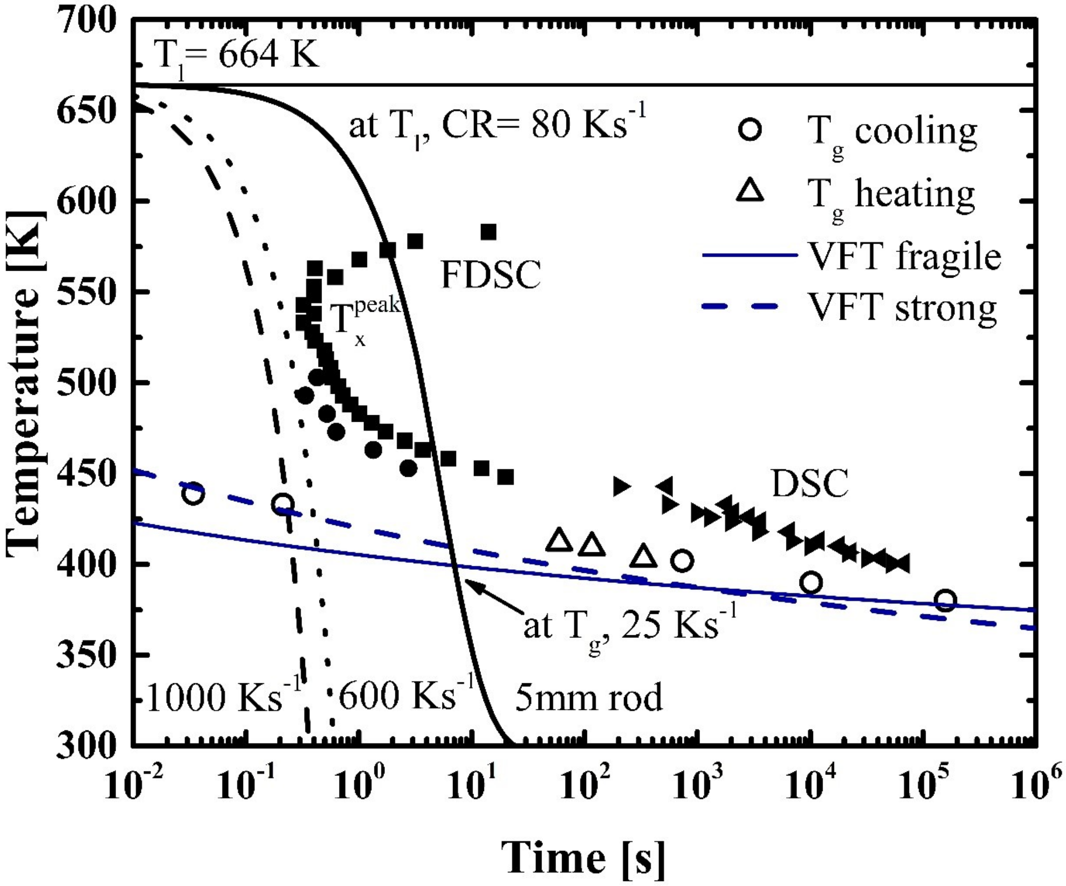

Figure 5-28: TTT diagram of the $Au_{49}Cu_{26.9}Si_{16.3}Ag_{5.5}Pd_{2.3}$ glass-forming liquid. The liquidus temperature is 664 K [161].The critical cooling rate of the alloy for small samples is determined in a Flash DSC to be between 1000 Ks^{-1}[171] (black, dashed line) and 600 Ks^{-1} [217,218] (black, dotted line). The cooling protocol of a 5 mm thick rod is given as the solid black line. The crystallization behavior is determined using DSC and FDSC [218] (filled squares, circles and triangles). The glass transition is determined from XRD results, FDSC (open circles) upon cooling and DSC open triangles upon heating. The VFT function of the fragile (blue, solid line) and strong liquid (blue, dashed line) are inserted as well.

As the strong liquid is frozen upon processing the bulk samples like a 5 mm rod and the fragile liquid is frozen in the FDSC and during melt spinning with cooling rates above 600 K s^{-1}, the LLT seems to be of first order, which is the working basis for the discussion about the critical temperature of the transition in the following section.

5.2.7 The critical temperature of the LLT

If the transition is assumed to be of first order, then there is a critical temperature below which the strong liquid phase is thermodynamically stable. This temperature is crucial for the understanding of the transition, but it is very difficult to determine.

The laboratory-based techniques, like DMA, DSC, and TMA, probe only the dynamics of the phase, which was formed during the processing. From those ex-situ measurements, we can speculate that the fragile liquid is frozen-in when forming ribbons with a cooling rate of 10^6 K s^{-1} and the strong liquid is frozen-in when we cast bulk samples with 50 K s^{-1}, as we have discussed in the previous sections. This suggestion is straight forward as only samples with different cooling rates are compared in terms of their dynamics and the rapidly cooled samples behave fragile, whereas the slowly cooled samples behave strong.

The XPCS and XRD measurements were the only measurements, in which the transition was observed in-situ. The transition has been observed after heating a melt-spun ribbon very slowly from room temperature into the supercooled liquid at 395.5 K and then cooled quasi-statically. The LLT occurred in terms of dynamics at 389 K. When the transition is of first order, there are only two possible scenarios where the critical temperature could lie. It could be at 389 K or higher.

Figure 5-29 shows the TTT diagram schematically for the scenario, where the critical temperature of the transition would be 389 K. As can be seen, the casting process of the ribbon avoids the formation of the strong phase. Then, the ribbon is heated very slowly with long isotherms as described in section 4.1. The material equilibrated upon heating at 393 K, so above the critical temperature. During the quasi-static cooling protocol, the material transforms into the strong liquid as soon as temperature falls below the critical temperature of 389 K.

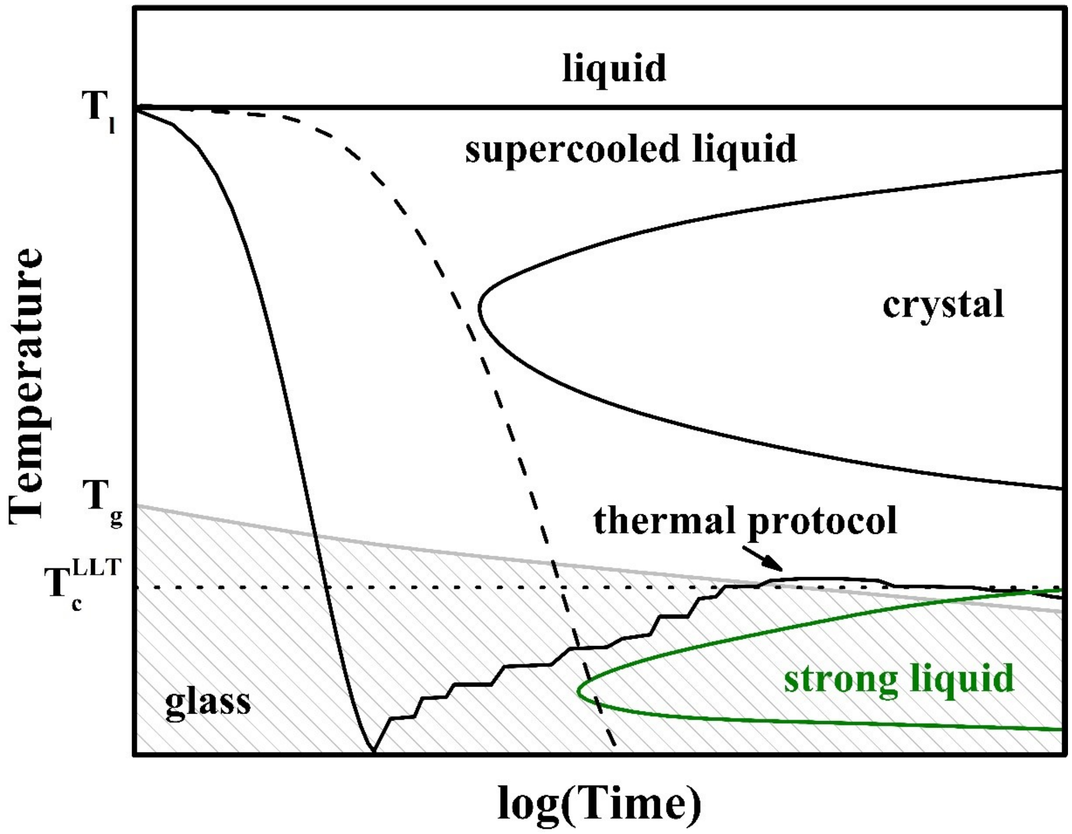

Figure 5-29: Schematic TTT diagram of scenario 1, where the critical temperature of the LLT is 389 K (dotted line). The solid line describes the thermal protocol in which the LLT was observed in-situ during XPCS and XRD synchrotron measurements. The dashed line describes the thermal protocol of a bulk sample. The solid black nose is the crystallization nose. The solid green nose is the nose of the strong liquid.

If this scenario would be the case, then transformation nose of the LLT is very close to the critical temperature implying a small interfacial energy difference between the two liquids, relatively large driving force and a fast transformation process despite the sluggish dynamics with relaxation times in the range of 100 s. Additionally, when bulk samples are cast, the liquid would have to undergo the transition below 389 K, which is lower than the expected glass transition of the fragile liquid phase for this cooling rates. According to Figure 5-3 the glass transition temperature upon cooling is well above 400 K for cooling rates of 10 K s^{-1} to 100 K s^{-1}. Therefore, the fragile liquid would form a glass and the glass of the fragile liquid would have to transform into a glass of the strong liquid. This fact makes this scenario not impossible but unlikely. In the light of Angell's "Big Picture" [7], which is illustrated in Figure 2-15, this scenario would be an example of the transition from fragile to intermediate behavior. At high cooling rates the $Au_{49}Cu_{26.9}Si_{16.3}Ag_{5.5}Pd_{2.3}$ glass-forming liquid behaves like a fragile glass-former (see Figure 2-15c). The glass transition occurs upon cooling at higher temperatures than the critical temperature of the LLT, which would be 389 K. When looking at the quasi-static cooling, the glass transition is shifted to temperatures below the critical temperature of the LLT, which then occurs in the supercooled liquid state above T_g. This is the behavior of intermediate glass-formers (see Figure 2-15b).

Figure 5-30 shows the schematic TTT diagram of the second scenario, where the critical temperature is significantly higher than 389 K. It is set arbitrarily. In this case, the casting process avoids the formation of the strong phase as in the first scenario. Upon heating, the material equilibrates at 393 K into the SCL as well. The main difference is that the fragile liquid is thermodynamically less favorable than the strong phase at all temperatures below the critical temperature. For this reason, it is only a question of time, when the transition occurs during the quasi-static cooling protocol. In this scenario, the fragile liquid can transform at higher temperatures into the strong phase during the processing of bulk samples and makes it more likely than the previous discussed scenario. According to Angell's "Big Picture" [7], the material is an intermediate glass-former no matter what cooling rate is applied. The critical temperature of the LLT is always higher than T_g. But when the transition is of first order, a high cooling rate can suppress the transformation due to the sluggish kinetics in that temperature range.

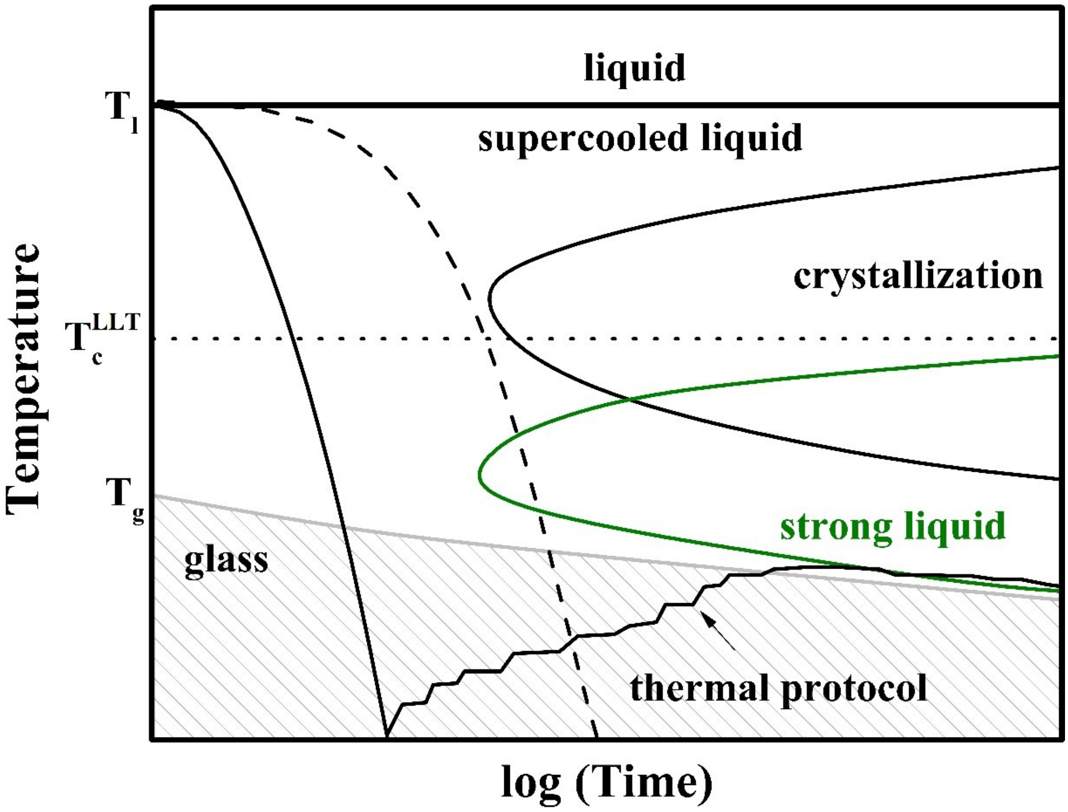

Figure 5-30: Schematic TTT diagram of scenario 2, where the critical temperature of the LLT is higher than 389 K (dotted line). The temperature is chosen arbitrarily. The solid line describes the thermal protocol in which the LLT was observed in-situ during XPCS and XRD synchrotron measurements. The dashed line describes the thermal protocol of a bulk sample. The solid black nose is the crystallization nose. The solid green nose is the nose of the strong liquid.

6 Summary and conclusion

The aging behavior of the glass, which was discussed in chapter 4 gives evidence for a complex aging behavior on the microscopic scale, which is qualitatively reflected by the macroscopic enthalpy recovery measurements. Due to the slow heating protocol the glass gets trapped in a deep energy minimum, which is why it does not equilibrate even if it is annealed for many times longer than the relaxation time of the liquid.

In the supercooled liquid, the different measurement techniques clearly indicate a liquid-liquid transition. During XPCS and XRD measurements upon quasi-static cooling the transition can be observed in-situ. Based on XPCS, DMA, TMA and Couette rheometry, a clear change in the dynamics from a very fragile liquid, which is stable from the equilibrium liquid above the liquidus temperature down to temperatures in vicinity of the glass transition to a strong liquid is obvious (see Figure 5-15 and Figure 5-17). The structural changes occur in the same temperature range where the dynamical cross-over occurs, indicating a direct connection between the two phenomena (see Figure 6-1). Additionally, the enthalpic signature of the transition has also been observed ex-situ in enthalpy recovery measurements, where a change of the heat capacity between the two liquids has been shown (see Figure 5-18).

The fact that both liquids can be frozen-in during the processing of the $Au_{49}Cu_{26.9}Si_{16.3}Ag_{5.5}Pd_{2.3}$ alloy indicates a first order transition between a high temperature fragile liquid and a low temperature strong liquid. When the dynamical and structural crossovers during the quasi-static cooling are compared as shown in Figure 6-1, one main difference stands out. The structure $((Q_1^{max}(T_{ref})/Q_1^{max})^3)$ changes constantly within a range of 10 K, whereas the dynamical crossover occurs at a well-defined temperature, when the increase in $(Q_1^{max}(T_{ref})/Q_1^{max})^3$ has happened to 50%.

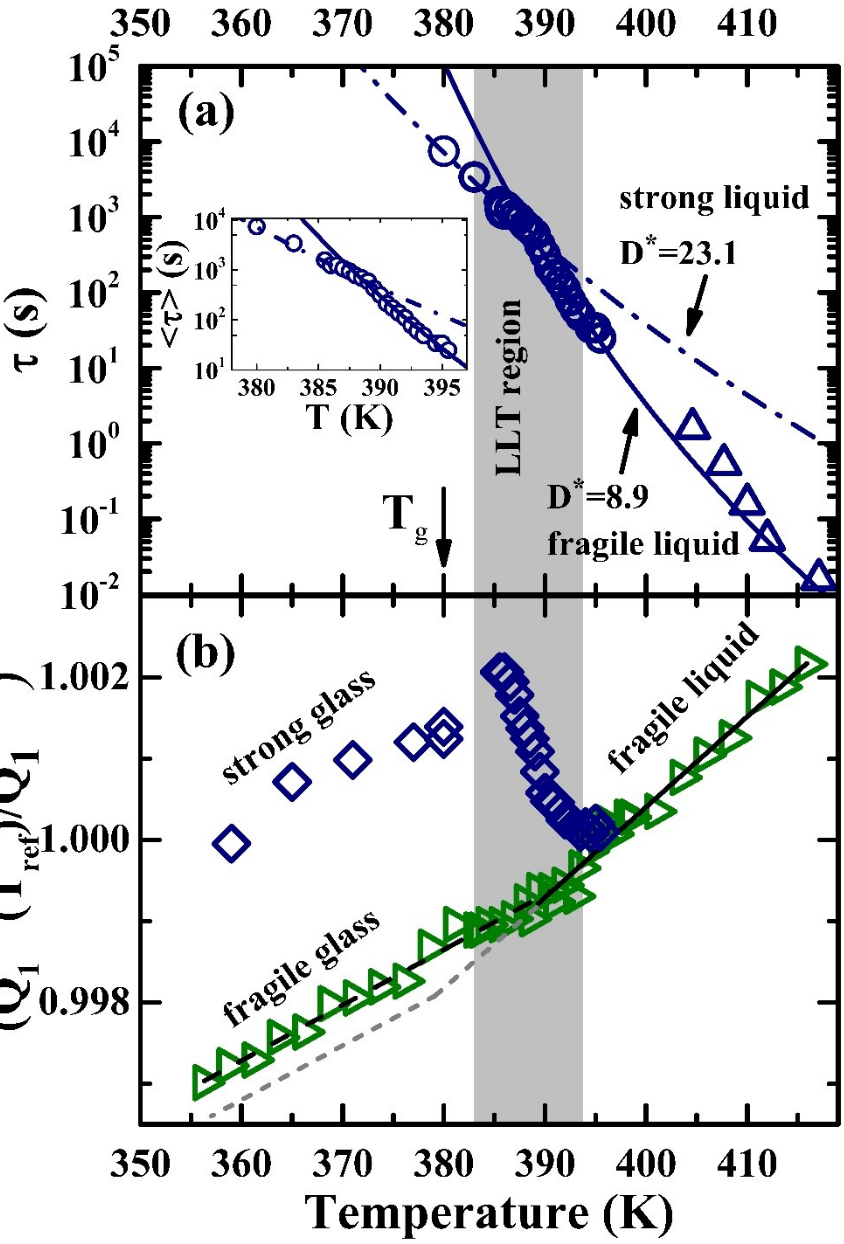

Figure 6-1: (a) Temperature dependence of τ measured by XPCS (circles) and DMA (triangles). The LLT occurs at 389 K leading to two regimes with distinct fragilities (magnified in the inset). (b) Temperature dependence of the relative shift $(Q_1^{max}(T_{ref})/Q_1^{max})^3$ of the FSDP measured with XRD by continuous cooling with 1.5 K min^{-1} (green triangles), and by applying the quasi-static protocol used for the XPCS data (blue diamonds). The grey dashed line shows the standard behavior that one would have expected to see in absence of the LLT. The figure is reproduced from [234].

In the light of Tanaka's two-state model based on locally ordered structures (see section 2.5.1), the change in the dynamics is expected to happen exactly when the structure consists to 50% of the locally ordered structure. This is one of the boundary conditions for the transition. At that point the locally more ordered structure (strong liquid phase) dominates the dynamics of the system. But the missing two-step behavior in the intensity auto-correlation function questions this idea and a coherent description of the transition cannot be made. Assuming a first order phase transition between the two liquids, schematic time-temperature-transition diagrams have been prepared (see Figure 5-29 and Figure 5-30) to discuss whether the critical temperature of the transition is 389 K or lies at higher temperatures. Although both scenarios are possible, scenario 2 (Figure 5-30), where the critical temperature is assumed to be significantly higher than 389 K, appears to be more coherent with the observations.

7 Outlook

The LLT in the $Au_{49}Cu_{26.9}Si_{16.3}Ag_{5.5}Pd_{2.3}$ alloy has been revealed as the main result of this work. It can stimulate the discussion whether a liquid exhibits a divergence in properties like structural relaxation time below T_g [71] or not [240–242], as such a transition could occur in any liquid below its glass transition. If it occurs in any liquid, the transition lowers the temperature at which the properties diverge, which could lead to the prevention any divergence at temperatures above 0 K. For the investigation of liquids in the relaxation time regime of the glass transition, synchrotron-based techniques like XPCS are a key tool to investigate the dynamics of liquids and glasses as these techniques possess the highest resolution by far. To push the frontier of our experimental possibilities, the quality of the synchrotron radiation is continuously improved. In the specific case of the ESRF, the upcoming upgrade will result in a fourth generation synchrotron source [173,243]. Due to significant improvements of the synchrotron radiation and the improved detector technology, the contrast and the temporal resolution will improve several orders of magnitude. Therefore, faster dynamics will be measurable at higher beam energies. But the quantum leap will be the use of free electron lasers which will improve the coherent flux of the radiation by five orders of magnitude and the average brilliance by at least two orders of magnitude with respect to synchrotron radiation [172,244]. Especially for XPCS, this evolution will widen the field of application significantly to faster dynamics and hopefully make his contribution to deepen our understanding of the dynamics of liquids and the understanding of LLTs.

But despite the improvements in synchrotron radiation, the main task will be to resolve the structure of liquids. It appears that the physical origin of LLTs and the question if there is a divergence below T_g can only be understood and predicted when the structure of liquids and their glasses can be described. Considering that, the increasing potential of computer-based simulation must be used to support the experimental progress or even guide the way for new experiments.

Besides the scientific progress which has been made by investigating the alloy, there is an industrial interest to solve the tarnishing problem of the alloy to make its unique properties regarding hardness, color and processing accessible for jewelry applications as it. For this reason, several derivates of the alloy have been developed to solve the tarnishing problem [161].

For amorphous metals in general, there is an increasing interest to get the unique mechanical properties into industrial applications as the superior casting properties and decreasing wrought material costs make e.g. Zr-, Cu-, Fe-, Ti- based amorphous metals competitive in the field of small high-strength components. Precious metal alloys based on platinum, palladium and gold become increasingly interesting for jewelry and luxuries like watches. Recently a new class of amorphous alloys have been developed, which could lower the barriers of entry into the market for amorphous metals [245].

8 Bibliography

[1] Y.-Q. Cheng, E. Ma, Atomic-level structure and structure-property relationship in metallic glasses, Prog. Mater. Sci. 56 (2011) 379–473. doi:10.1016/j.pmatsci.2010.12.002.

[2] S. Aasland, P.F. McMillan, Density-driven liquid-liquid phase separation in the system Al_2O_3-Y_2O_3, Lett. to Nat. 369 (1994) 633–636. doi:10.1038/369633a0.

[3] S. Wei, F. Yang, J. Bednarcik, I. Kaban, O. Shuleshova, A. Meyer, R. Busch, Liquid-liquid transition in a strong bulk metallic glass-forming liquid., Nat. Commun. 4 (2013) 2083. doi:10.1038/ncomms3083.

[4] S. Wei, M. Stolpe, O. Gross, W. Hembree, S. Hechler, J. Bednarcik, R. Busch, P. Lucas, Structural evolution on medium-range-order during the fragile-strong transition in $Ge_{15}Te_{85}$, Acta Mater. 129 (2017) 259–267. doi:10.1016/j.actamat.2017.02.055.

[5] V.V. Brazhkin, R.N. Voloshin, S.V. Popova, A.G. Umnov, Nonmetal-metal transition in sulphur melt under high pressure, Phys. Lett. A. 154 (1991) 413–415. doi:10.1016/0375-9601(91)90043-8.

[6] M. Kobayashi, H. Tanaka, The reversibility and first-order nature of liquid-liquid transition in a molecular liquid., Nat. Commun. 7 (2016) 13438. doi:10.1038/ncomms13438.

[7] C.A. Angell, Glass-Formers and Viscous Liquid Slowdown since David Turnbull: Enduring Puzzles and New Twists, MRS Bull. 33 (2011) 544–555. doi:10.1557/mrs2008.108.

[8] W. Klement, R.H. Willens, P. Duwez, Non-crystalline Structure in Solidified Gold–Silicon Alloys, Nature. 187 (1960) 869–870. doi:10.1038/187869b0.

[9] H. Bülow, W. Buckel, Elektronenbeugungsaufnahmen von dünnen

Metallschichten bei tiefen Temperaturen, Zeitschrift Für Phys. 138 (1956) 136–150. doi:10.1007/BF01339052.

[10] J. Schroers, B. Lohwongwatana, W.L. Johnson, A. Peker, Gold based bulk metallic glass, Appl. Phys. Lett. 87 (2005) 404–406. doi:10.1063/1.2008374.

[11] M. Telford, The case for bulk metallic glass, Mater. Today. 7 (2004) 36–43. doi:10.1016/S1369-7021(04)00124-5.

[12] J. Wang, R. Li, N. Hua, L. Huang, T. Zhang, Ternary Fe-P-C bulk metallic glass with good soft-magnetic and mechanical properties, Scr. Mater. 65 (2011) 536–539. doi:10.1016/j.scriptamat.2011.06.020.

[13] M. Shi, Z. Liu, T. Zhang, Effects of Metalloid B Addition on the Glass Formation, Magnetic and Mechanical Properties of FePCB Bulk Metallic Glasses, J. Mater. Sci. Technol. 31 (2015) 493–497. doi:10.1016/j.jmst.2014.10.009.

[14] M.F. Ashby, A.L. Greer, Metallic glasses as structural materials, Scr. Mater. 54 (2006) 321–326. doi:10.1016/j.scriptamat.2005.09.051.

[15] P.H. Gaskell, The structure of simple inorganic amorphous solids, J. Phys. C Solid State Phys. 12 (1979) 4337–4368. doi:10.1351/pac196918040489.

[16] J.D. Bernal, A Geometrical Approach to the Structure of Liquids, Nature. 183 (1959) 55–56. doi:10.1038/183055a0.

[17] J.D. Bernal, Geometry of the Structure of Monatomic Liquids, Nature. 185 (1960) 68–70.

[18] J.D. Bernal, Coordination of Randomly Packed Spheres, Nature. 188 (1960) 910–911.

[19] H.W. Sheng, W.K. Luo, F.M. Alamgir, J.M. Bai, E. Ma, Atomic packing and short-to-medium-range order in metallic glasses, Nature. 439 (2006) 419–425. doi:10.1038/nature04421.

[20] F.C. Frank, Supercooling of liquids, Proc. R. Soc. London Ser. A, Math. Phys. Sci. 215 (1952) 43–46.

[21] W. Hume-Rothery, E. Anderson, Eutectic compositions and liquid immiscibility in certain binary alloys, Philos. Mag. 5 (1960) 383–405. doi:10.1080/14786436008235856.

[22] H. Tanaka, General view of a liquid-liquid phase transition, Phys. Rev. E. 62 (2000) 6968–6976. doi:10.1103/PhysRevE.62.6968.

[23] T. Schenk, D. Holland-Moritz, V. Simonet, R. Bellissent, D.M. Herlach, Icosahedral Short-Range Order in Deeply Undercooled Metallic Melts, Phys. Rev. Lett. 89 (2002) 075507. doi:10.1103/PhysRevLett.89.075507.

[24] A. Hirata, L.J. Kang, T. Fujita, B. Klumov, K. Matsue, M. Kotani, A.R. Yavari, M.W. Chen, Geometric Frustration of Icosahedron in Metallic Glasses, Science (80-.). 341 (2013) 376–379. doi:10.1126/science.1232450.

[25] D.B. Miracle, W.S. Sanders, O.N. Senkov, The influence of efficient atomic packing on the constitution of metallic glasses, Philos. Mag. 83 (2003) 2409–2428. doi:10.1080/1478643031000098828.

[26] D.B. Miracle, Efficient local packing in metallic glasses, J. Non. Cryst. Solids. 342 (2004) 89–96. doi:10.1016/j.jnoncrysol.2004.05.017.

[27] D.B. Miracle, A structural model for metallic glasses, Nat. Mater. 3 (2004) 697–702. doi:10.1038/nmat1219.

[28] D.B. Miracle, T. Egami, K.M. Flores, K.F. Kelton, Structural Aspects of Metallic Glasses, MRS Bull. 32 (2007) 629–634. doi:10.1557/mrs2007.124.

[29] A.P. Wang, J.Q. Wang, E. Ma, Modified efficient cluster packing model for calculating alloy compositions with high glass forming ability, Appl. Phys. Lett. 90 (2007) 2005–2008. doi:10.1063/1.2715172.

[30] Z. Evenson, On the thermodynamic and kinetic properties of bulk glass forming metallic systems, Universität des Saarlandes, 2012.

[31] O. Gross, S.S. Riegler, M. Stolpe, B. Bochtler, A. Kuball, S. Hechler, R. Busch, I. Gallino, On the high glass-forming ability of Pt-Cu-Ni/Co-P-based liquids, Acta Mater. 141 (2017) 109–119. doi:10.1016/j.actamat.2017.09.013.

[32] E. Tombari, C. Ferrari, G. Salvetti, G.P. Johari, Vibrational and configurational specific heats during isothermal structural relaxation of a glass to equilibrium liquid, Phys. Rev. B - Condens. Matter Mater. Phys. 78 (2008) 1–8. doi:10.1103/PhysRevB.78.144203.

[33] E. Donth, H. Huth, M. Beiner, Characteristic Length of the Glass Transition; J. Non-Cryst. Solids, J. Physics. Condens. Matter. 13 (2001) L451–L462.

[34] S.A. Reinsberg, X.H. Qiu, M. Wilhelm, H.W. Spiess, M.D. Ediger, Length scale of dynamic heterogeneity in supercooled glycerol near Tg, J. Chem. Phys. 114 (2001) 7299–7302. doi:10.1063/1.1369160.

[35] U. Tracht, M. Wilhelm, A. Heuer, H. Feng, K. Schmidt-Rohr, H.W. Spiess, Length Scale of Dynamic Heterogeneities at the Glass Transition Determined by Multidimensional Nuclear Magnetic Resonance, Phys. Rev. Lett. 81 (1998) 2727–2730. doi:10.1103/PhysRevLett.81.2727.

[36] U. Tracht, M. Wilhelm, A. Heuer, H.W. Spiess, Combined reduced 4D 13C exchange and 1H spin diffusion experiment for determining the length scale of dynamic heterogeneities., J. Magn. Reson. 140 (1999) 460–470. doi:10.1006/jmre.1999.1854.

[37] A. Duri, L. Cipelletti, Length scale dependence of dynamical heterogeneity in a colloidal fractal gel, Europhys. Lett. 76 (2006) 972–978. doi:10.1209/epl/i2006-10357-4.

[38] D. Orsi, L. Cristofolini, G. Baldi, A. Madsen, Heterogeneous and anisotropic dynamics of a 2D Gel, Phys. Rev. Lett. 108 (2012) 1–5. doi:10.1103/PhysRevLett.108.105701.

[39] C. Dalle-Ferrier, C. Thibierge, C. Alba-Simionesco, L. Berthier, G. Biroli, J.-P. Bouchaud, F. Ladieu, D. L'Hôte, G. Tarjus, Spatial correlations in the dynamics of glassforming liquids: Experimental determination of their temperature dependence, Phys. Rev. E - Stat. Nonlinear, Soft Matter Phys. 76 (2007) 1–15. doi:10.1103/PhysRevE.76.041510.

[40] P. Gadige, D. Saha, S.K. Behera, R. Bandyopadhyay, Study of dynamical heterogeneities in colloidal nanoclay suspensions approaching dynamical

arrest, Sci. Rep. 7 (2017) 8017. doi:10.1038/s41598-017-08495-9.

[41] L. Berthier, G. Biroli, J.-P. Bouchaud, L. Cipelletti, D. El Masri, D. L'Hôte, F. Ladieu, M. Pierno, Direct Experimental Evidence of a Growing Length Scale Accompanying the Glass Transition, Sci. Reports. 310 (2005) 1797–1800. doi:10.1126/science.1120714.

[42] L. Berthier, G. Biroli, J.-P. Bouchaud, L. Cipelletti, W. van Saarloos, Dynamical Heterogeneities in Glasses, Colloids and Granular Media, Oxford University Press, Oxford, New York, 2011.

[43] R. Richert, Heterogeneous dynamics in liquids: fluctuations in space and time, J. Phys. Condens. Matter. 14 (2002) R703–R738. doi:10.1088/0953-8984/14/23/201.

[44] L. Berthier, Time and length scales in supercooled liquids, Phys. Rev. E - Stat. Nonlinear, Soft Matter Phys. 69 (2004) 14–16. doi:10.1103/PhysRevE.69.020201.

[45] M.M. Hurley, P. Harrowell, Kinetic structure of a two-dimensional liquid, Phys. Rev. E. 52 (1995) 1694–1698.

[46] C. Bennemann, C. Donati, J. Baschnagel, S.C. Glotzer, Growing range of correlated motion in a polymer melt on cooling towards the glass transition, Nature. 399 (1999) 246–249. doi:10.1038/20406.

[47] C. Donati, S. Franz, S.C. Glotzer, G. Parisi, Theory of non-linear susceptibility and correlation length in glasses and liquids, J. Non. Cryst. Solids. 307–310 (2002) 215–224. doi:10.1016/S0022-3093(02)01461-8.

[48] S. Whitelam, L. Berthier, J.P. Garrahan, Dynamic criticality in glass-forming liquids, Phys. Rev. Lett. 92 (2004) 185705–1. doi:10.1103/PhysRevLett.92.185705.

[49] J.P. Garrahan, D. Chandler, Geometrical explanation and scaling of dynamical heterogeneities in glass forming systems, Phys. Rev. Lett. 89 (2002) 357041–357044. doi:10.1103/PhysRevLett.89.035704.

[50] C. Toninelli, M. Wyart, L. Berthier, G. Biroli, J.-P. Bouchaud, Dynamical

susceptibility of glass formers: Contrasting the predictions of theoretical scenarios, Phys. Rev. E - Stat. Nonlinear, Soft Matter Phys. 71 (2005) 1–20. doi:10.1103/PhysRevE.71.041505.

[51] S. Hechler, I. Gallino, M. Stolpe, F.-T. Lentes, R. Busch, Analysis of thermophysical properties of lead silicates in comparison to bulk metallic glasses, J. Non. Cryst. Solids. 485 (2018) 66–73. doi:10.1016/j.jnoncrysol.2018.01.041.

[52] Z. Evenson, B. Ruta, S. Hechler, M. Stolpe, E. Pineda, I. Gallino, R. Busch, X-Ray Photon Correlation Spectroscopy Reveals Intermittent Aging Dynamics in a Metallic Glass, Phys. Rev. Lett. 115 (2015) 175701. doi:10.1103/PhysRevLett.115.175701.

[53] C.A. Angell, K.L. Ngai, G.B. McKenna, P.F. McMillan, S.W. Martin, Relaxation in glassforming liquids and amorphous solids, J. Appl. Phys. 88 (2000) 3113. doi:10.1063/1.1286035.

[54] S. Mossa, F. Sciortino, Crossover (or Kovacs) Effect in an Aging Molecular Liquid, Phys. Rev. Lett. 92 (2004) 045504. doi:10.1103/PhysRevLett.92.045504.

[55] Z. Evenson, R. Busch, Equilibrium viscosity, enthalpy recovery and free volume relaxation in a $Zr_{44}Ti_{11}Ni_{10}Cu_{10}Be_{25}$ bulk metallic glass, Acta Mater. 59 (2011) 4404–4415. doi:http://dx.doi.org/10.1016/j.actamat.2011.03.064.

[56] C.A. Angell, Perspectives on the Glass Transition, J. Phys. Chem. Solids. 49 (1988) 863–871. doi:10.1016/0022-3697(88)90002-9.

[57] C.A. Angell, Relaxation in liquids, polymers and plastic crystals — strong/fragile patterns and problems, J. Non. Cryst. Solids. 131 (1991) 13–31. doi:10.1016/0022-3093(91)90266-9.

[58] R. Böhmer, K.L. Ngai, C.A. Angell, D.J. Plazek, Nonexponential relaxations in strong and fragile glass formers, J. Chem. Phys. 99 (1993) 4201. doi:10.1063/1.466117.

[59] C.A. Angell, Formation of Glasses from Liquids and Biopolymers, Science

(80-.). 267 (1995) 1924–1935.

[60] W. Oldekop, Theoretische Betrachtungen über die Zähigkeit von Gläsern, Glas. Berichte. 30 (1957).

[61] W.T. Laughlin, D.R. Uhlmann, Viscous flow in simple organic liquids, J. Phys. Chem. 76 (1972) 2317–2325. doi:10.1021/j100660a023.

[62] C.A. Angell, The old problems of glass and the glass transition, and the many new twists., Proc. Natl. Acad. Sci. U. S. A. 92 (1995) 6675–6682. doi:10.1073/pnas.92.15.6675.

[63] L.-M. Martinez, C.A. Angell, A thermodynamic connection to the fragility of glass-forming liquids, Lett. to Nat. 410 (2001) 663–667.

[64] H. Vogel, -, Phys. Zeitschrift. 22 (1921).

[65] J. Fulcher, -, J. Am. Ceram. Soc. 8 (1925).

[66] G. Tammann, -, J. Soc. Glas. Technol. 9 (1925) 166–185.

[67] I. Gallino, J. Schroers, R. Busch, Kinetic and thermodynamic studies of the fragility of bulk metallic glass forming liquids, J. Appl. Phys. 108 (2010) 1–9. doi:10.1063/1.3480805.

[68] O. Gross, B. Bochtler, M. Stolpe, S. Hechler, W. Hembree, R. Busch, I. Gallino, The kinetic fragility of Pt-P- and Ni-P-based bulk glass forming liquids and its thermodynamic and structural signature, Acta Mater. 132 (2017) 118–127. doi:10.1016/j.actamat.2017.04.030.

[69] SchottAG, Optisches Glas 2014, Beschreibung der Eigenschaften, in: Schott Opt. Glas., 2014: p. 109.

[70] R. Busch, W. Liu, W.L. Johnson, Thermodynamics and kinetics of the $Mg_{65}Cu_{25}Y_{10}$ bulk metallic glass forming liquid, J. Appl. Phys. 83 (1998) 4134–4141.

[71] G. Adam, J.H. Gibbs, On the Temperature Dependence of Cooperative Relaxation Properties in Glass-Forming Liquids, J. Chem. Phys. 43 (1965) 139. doi:10.1063/1.1696442.

[72] K. Ito, C.T. Moynihan, C.A. Angell, Thermodynamic determination of fragility in liquids and a fragile-to-strong liquid transition in water, Lett. to Nat. 398 (1999) 492–495.

[73] S. Sastry, The relationship between fragility, configurational entropy and the potential energy landscape of glass-forming liquids, Nature. 409 (2001) 164–167. doi:10.1038/35051524.

[74] G.D. Fontana, L. Battezzati, Thermodynamic and dynamic fragility in metallic glass-formers, Acta Mater. 61 (2013) 2260–2267. doi:10.1016/j.actamat.2012.12.045.

[75] K.F. Kelton, Kinetic and structural fragility-a correlation between structures and dynamics in metallic liquids and glasses., J. Phys. Condens. Matter. 29 (2017) 023002. doi:10.1088/0953-8984/29/2/023002.

[76] L.-M. Wang, C.A. Angell, R. Richert, Fragility and thermodynamics in nonpolymeric glass-forming liquids, J. Chem. Phys. 125 (2006) 1–8. doi:10.1063/1.2244551.

[77] S. Wei, I. Gallino, R. Busch, C.A. Angell, Glass transition with decreasing correlation length during cooling of $Fe_{50}Co_{50}$ superlattice and strong liquids, Nat. Phys. 5 (2010) 1–5. doi:10.1038/nphys1823.

[78] S. Wei, Z. Evenson, I. Gallino, R. Busch, The impact of fragility on the calorimetric glass transition in bulk metallic glasses, Intermetallics. 55 (2014) 138–144. doi:10.1016/j.intermet.2014.07.018.

[79] C.A. Angell, Glass formation and glass transition in supercooled liquids, with insights from study of related phenomena in crystals, J. Non. Cryst. Solids. 354 (2008) 4703–4712. doi:10.1016/j.jnoncrysol.2008.05.054.

[80] Z. Evenson, T. Schmitt, M. Nicola, I. Gallino, R. Busch, High temperature melt viscosity and fragile to strong transition in Zr-Cu-Ni-Al-Nb(Ti) and $Cu_{47}Ti_{34}Zr_{11}Ni_8$ bulk metallic glasses, Acta Mater. 60 (2012) 4712–4719. doi:10.1016/j.actamat.2012.05.019.

[81] S. Wei, M. Stolpe, O. Gross, Z. Evenson, I. Gallino, W. Hembree, J.

Bednarcik, J.J. Kruzic, R. Busch, Linking structure to fragility in bulk metallic glass-forming liquids, Appl. Phys. Lett. 106 (2015) 181901. doi:10.1063/1.4919590.

[82] M. Stolpe, I. Jonas, S. Wei, Z. Evenson, W. Hembree, F. Yang, A. Meyer, R. Busch, Structural changes during a liquid-liquid transition in the deeply undercooled, Phys. Rev. B. 93 (2016) 014201. doi:10.1103/PhysRevB.93.014201.

[83] S. Wei, P. Lucas, C.A. Angell, Phase change alloy viscosities down to Tg using Adam-Gibbs-equation fittings to excess entropy data: A fragile-to-strong transition, J. Appl. Phys. 118 (2015) 034903. doi:10.1063/1.4926791.

[84] R.J. Speedy, Relations between a Liquid and Its Glasses, J. Phys. Chem. B. 103 (1999) 4060–4065.

[85] P. Richet, Viscosity and configurational entropy of silicate melts, Geochim. Cosmochim. Acta. 48 (1984) 471–483. doi:10.1016/0016-7037(84)90275-8.

[86] P. Richet, Y. Bottinga, Glass transitions and thermodynamic properties of amorphous SiO_2, $NaAlSi_nO_{2n+2}$ and $KAlSi_3O_8$, Geochim. Cosmochim. Acta. 48 (1984) 453–470. doi:10.1016/0016-7037(84)90274-6.

[87] H. Tanaka, Relationship among glass-forming ability, fragility, and short-range bond ordering of liquids, J. Non. Cryst. Solids. 351 (2005) 678–690. doi:10.1016/j.jnoncrysol.2005.01.070.

[88] H. Tanaka, Bond orientational order in liquids: Towards a unified description of water-like anomalies, liquid-liquid transition, glass transition, and crystallization, Eur. Phys. J. E. 35 (2012) 113. doi:10.1140/epje/i2012-12113-y.

[89] D. V. Louzguine-Luzgin, R. Belosludov, A.R. Yavari, K. Georgarakis, G. Vaughan, Y. Kawazoe, T. Egami, A. Inoue, Structural basis for supercooled liquid fragility established by synchrotron-radiation method and computer simulation, J. Appl. Phys. 110 (2011). doi:10.1063/1.3624745.

[90] J. Zhao, Z. Tang, K.F. Kelton, C.T. Liu, P.K. Liaw, A. Inoue, X. Shen, S.

Pan, M.L. Johnson, G. Chen, C. Fan, Evolution of the atomic structure of a supercooled Zr55Cu35Al10 liquid, Intermetallics. 82 (2017) 53–58. doi:10.1016/j.intermet.2016.11.010.

[91] Q. Zheng, M. Potuzak, J.C. Mauro, M.M. Smedskjaer, R.E. Youngman, Y. Yue, Composition – structure – property relationships in boroaluminosilicate glasses, J. Non. Cryst. Solids. 358 (2012) 993–1002. doi:10.1016/j.jnoncrysol.2012.01.030.

[92] N.A. Mauro, M. Blodgett, M.L. Johnson, A.J. Vogt, K.F. Kelton, A structural signature of liquid fragility, Nat. Commun. 5 (2014) 1–7. doi:10.1038/ncomms5616.

[93] N.A. Mauro, A.J. Vogt, M.L. Johnson, J.C. Bendert, K.F. Kelton, Anomalous structural evolution in $Cu_{50}Zr_{50}$ glass-forming liquids, Appl. Phys. Lett. 103 (2013). doi:10.1063/1.4813389.

[94] A.K. Gangopadhyay, C.E. Pueblo, R. Dai, M.L. Johnson, R. Ashcraft, D. Van Hoesen, M. Sellers, K.F. Kelton, Correlation of the fragility of metallic liquids with the high temperature structure, volume, and cohesive energy, J. Chem. Phys. 146 (2017). doi:10.1063/1.4981011.

[95] B. Bochtler, O. Gross, I. Gallino, R. Busch, Thermo-physical characterization of the $Fe_{67}Mo_{6}Ni_{3.5}Cr_{3.5}P_{12}C_{5.5}B_{2.5}$ bulk metallic glass forming alloy, Acta Mater. 118 (2016) 129–139. doi:10.1016/j.actamat.2016.07.031.

[96] I. Saika-Voivod, P.H. Poole, F. Sciortino, Fragile-to-strong transition and polyamorphism in the energy landscape of liquid silica., Nature. 412 (2001) 514–517. doi:10.1038/35087524.

[97] C. Way, P. Wadhwa, R. Busch, The influence of shear rate and temperature on the viscosity and fragility of the $Zr_{41.2}Ti_{13.8}Cu_{12.5}Ni_{10.0}Be_{22.5}$ metallic-glass-forming liquid, Acta Mater. 55 (2007) 2977–2983. doi:10.1016/j.actamat.2006.12.032.

[98] C. Zhang, L. Hu, Y. Yue, J.C. Mauro, Fragile-to-strong transition in metallic glass-forming liquids, J. Chem. Phys. 133 (2010) 1–7.

doi:10.1063/1.3457670.

[99] C. Zhou, L. Hu, Q. Sun, H. Zheng, C. Zhang, Y. Yue, Structural evolution during fragile-to-strong transition in CuZr(Al) glass-forming liquids, J. Chem. Phys. 142 (2015). doi:10.1063/1.4907374.

[100] P.F. McMillan, M. Wilson, D. Daisenberger, D. Machon, A density-driven phase transition between semiconducting and metallic polyamorphs of silicon., Nat. Mater. 4 (2005) 680–684. doi:10.1038/nmat1458.

[101] V. V. Vasisht, S. Saw, S. Sastry, Liquid-liquid critical point in supercooled silicon, Nat. Phys. 7 (2011) 549–553. doi:10.1038/nphys1993.

[102] A. Ferraz, N.H. March, Liquid-Phase Metal Non Metal Transition in Carbon, Phys. Chem. Liq. 8 (1979) 289–297. doi:10.1080/00319107908084761.

[103] P. Gallo, K. Amann-Winkel, C.A. Angell, M.A. Anisimov, F. Caupin, C. Chakravarty, E. Lascaris, T. Loerting, A.Z. Panagiotopoulos, J. Russo, J.A. Sellberg, H.E. Stanley, H. Tanaka, C. Vega, L. Xu, L.G.M. Pettersson, Water: A Tale of Two Liquids, Chem. Rev. 116 (2016) 7463–7500. doi:10.1021/acs.chemrev.5b00750.

[104] H. Tanaka, R. Kurita, H. Mataki, Liquid-Liquid Transition in the Molecular Liquid Triphenyl Phosphite, Phys. Rev. Lett. 92 (2004) 025701. doi:10.1103/PhysRevLett.92.025701.

[105] C. Zhou, L. Hu, Q. Sun, J. Qin, X. Bian, Y. Yue, Indication of liquid-liquid phase transition in CuZr-based melts, Appl. Phys. Lett. 103 (2013) 1–5. doi:10.1063/1.4826487.

[106] M.H. Bhat, V. Molinero, E. Soignard, V.C. Solomon, S. Sastry, J.L. Yarger, C.A. Angell, Vitrification of a monatomic metallic liquid., Nature. 448 (2007) 787–90. doi:10.1038/nature06044.

[107] G.N. Greaves, M.C. Wilding, S. Fearn, D. Langstaff, F. Kargl, S. Cox, Q.V. Van, O. Majérus, C.J. Benmore, R. Weber, C.M. Martin, L. Hennet, Detection of First-Order Liquid/Liquid Phase Transitions in Yttrium Oxide –

Aluminum Oxide Melts, Science (80-.). 322 (2008) 566–570.

[108] P. Gallo, D. Corradini, M. Rovere, Widom line and dynamical crossovers as routes to understand supercritical water., Nat. Commun. 5 (2014) 5806. doi:10.1038/ncomms6806.

[109] L. Xu, S. V. Buldyrev, C.A. Angell, H.E. Stanley, Thermodynamics and dynamics of the two-scale spherically symmetric Jagla ramp model of anomalous liquids, Phys. Rev. E - Stat. Nonlinear, Soft Matter Phys. 74 (2006) 1–10. doi:10.1103/PhysRevE.74.031108.

[110] L. Xu, P. Kumar, S. V. Buldyrev, S.-H. Chen, P.H. Poole, F. Sciortino, H.E. Stanley, Relation between the Widom line and the dynamic crossover in systems with a liquid-liquid phase transition, Proc. Natl. Acad. Sci. 102 (2005) 16558–16562. doi:10.1073/pnas.0507870102.

[111] Y. Katayama, T. Mizutani, W. Utsumi, O. Shimomura, M. Yamakata, K. Funakoshi, A first-order liquid-liquid phase transition in phosphorus, Nature. 403 (2000) 170–173. doi:10.1038/35003143.

[112] Y. Katayama, Y. Inamura, T. Mizutani, M. Yamakata, W. Utsumi, O. Shimomura, Macroscopic Separation of Dense Fluid Phase and Liquid Phase of Phosphorus, Sci. Reports. 306 (2004) 848–851. doi:10.1126/science.1102735.

[113] S. Strässler, C. Kittel, Degeneracy and the Order of the Phase Transformation in the Molecular-Field Approximation, Phys. Rev. 139 (1965) 3–5.

[114] C.A. Angell, Configurational Excitations in Condensed Matter, and the ``Bond Lattice'' Model for the Liquid-Glass Transition, J. Chem. Phys. 57 (1972) 470. doi:10.1063/1.1677987.

[115] C.A. Angell, B.E. Richards, V. Velikov, Simple glass-forming liquids : their definition , fragilities , and landscape excitation profiles, J. Phys. Condens. Matter. 11 (1999) A75–A94.

[116] D. V. Matyushov, C.A. Angell, Gaussian excitations model for glass-former

dynamics and thermodynamics, J. Chem. Phys. 126 (2007). doi:10.1063/1.2538712.

[117] A.C. Mitus, A.Z. Patashinski, B.I. Shumilo, The liquid-liquid phase transition, Phys. Lett. 113A (1985) 41–44. http://linkinghub.elsevier.com/retrieve/pii/0375960185906024.

[118] H. Tanaka, Simple Physical Explanation of the Unusual Thermodynamic Behavior of Liquid Water, Phys. Rev. Lett. 80 (1998) 5750–5753. doi:10.1103/PhysRevLett.80.5750.

[119] H. Tanaka, Two-order-parameter description of liquids: critical phenomena and phase separation of supercooled liquids, J. Phys. Condens. Matter. 11 (1999) L159–L168. doi:10.1088/0953-8984/11/15/005.

[120] H. Tanaka, Two-order-parameter description of liquids. I. A general model of glass transition covering its strong to fragile limit, J. Chem. Phys. 111 (1999) 3163. doi:10.1063/1.479596.

[121] H. Tanaka, A simple physical picture of liquid–glass transition, J. Chem. Phys. 105 (1996) 9375. doi:10.1063/1.472766.

[122] H. Tanaka, A simple physical model of liquid – glass transition : intrinsic fluctuating interactions and random fields hidden in glass-forming liquids, J. Phys. Condens. Matter. 10 (1998) L207-214.

[123] H. Tanaka, Simple physical model of liquid water, J. Chem. Phys. 112 (2000) 799. doi:10.1063/1.480609.

[124] F.H. Stillinger, Relaxation and flow mechanisms in '"fragile"' glass-forming liquids, J. Chem. Phys. 89 (1988) 6461. doi:10.1063/1.455365.

[125] F.C. Frank, J.S. Kasper, Complex alloy structures regarded as sphere packings. II. Analysis and classification of representative structures, Acta Crystallogr. 12 (1959) 483–499. doi:10.1107/S0365110X59001499.

[126] M. Hoare, Stability and Local Order in Simple Amorphous Packings, Ann. N. Y. Acad. Sci. 279 (1976) 186–207. doi:10.1111/j.1749-6632.1976.tb39707.x.

[127] S.A. Kivelson, X. Zhao, D. Kivelson, T.M. Fischer, C.M. Knobler, Frustration-limited clusters in liquids, J. Chem. Phys. 101 (1994) 2391. doi:10.1063/1.468414.

[128] D. Kivelson, S.A. Kivelson, X. Zhao, Z. Nussinov, G. Tarjus, A thermodynamic theory of supercooled liquids, Phys. A Stat. Mech. Its Appl. 219 (1995) 27–38. doi:10.1016/0378-4371(95)00140-3.

[129] L. Xu, F. Mallamace, Z. Yan, F.W. Starr, S. V. Buldyrev, H.E. Stanley, Appearance of a fractional Stokes–Einstein relation in water and a structural interpretation of its onset, Nat. Phys. 5 (2009) 565–569. doi:10.1038/nphys1328.

[130] L. Xu, S. V. Buldyrev, N. Giovambattista, C.A. Angell, H.E. Stanley, A monatomic system with a liquid-liquid critical point and two distinct glassy states, J. Chem. Phys. 130 (2009) 1–12. doi:10.1063/1.3043665.

[131] T. Morishita, Liquid-Liquid Phase Transitions of Phosphorus via Constant-Pressure First-Principles Molecular Dynamics Simulations, Phys. Rev. Lett. 87 (2001) 1–4. doi:10.1103/PhysRevLett.87.105701.

[132] L.I. Aptekar, Phase transitions in noncrystalline germanium and silicon, Sov. Phys. Dokl. 24 (1979) 993–995.

[133] F.X. Zhang, W.K. Wang, Crystal structure of germanium quenched from the melt under high pressure, Phys. Rev. B. 52 (1995) 3113–3116. doi:10.1103/PhysRevB.52.3113.

[134] D. Li, D.M. Herlach, Containerless solidification of germanium by electromagnetic levitation and in a drop-tube, J. Mater. Sci. 32 (1997) 1437–1442. doi:10.1023/A:1018593615171.

[135] G.A. Voronin, C. Pantea, T.W. Zerda, J. Zhang, L. Wang, Y. Zhao, In situ X-ray diffraction study of germanium at pressures up to 11 GPa and temperatures up to 950 K, J. Phys. Chem. Solids. 64 (2003) 2113–2119. doi:10.1016/S0022-3697(03)00278-6.

[136] Y. Tsuchiya, Thermodynamic evidence for a structural transition of liquid

Te in the supercooled region, J. Phys. Condens. Matter. 3 (1999) 3163–3172. doi:10.1088/0953-8984/3/18/010.

[137] H. Kanno, H. Yokoyama, Y. Yoshimura, A New Interpretation of Anomalous Properties of Water Based on Stillinger's Postulate, J. Phys. Chem. B. 105 (2001) 2019–2026. doi:10.1021/jp003639y.

[138] C. Bergman, C. Bichara, J.P. Gaspard, Y. Tsuchiya, Experimental investigation of the waterlike density anomaly in the liquid $Ge_{15}Te_{85}$ eutectic alloy, Phys. Rev. B. 67 (2003) 104202. doi:10.1103/PhysRevB.67.104202.

[139] Y. Tsuchiya, K. Saitoh, F. Kakinuma, Thermodynamics of structural changes in liquid Ge-Te alloys around the eutectic composition: Specific heat measurements and thermodynamic stability, Monatshefte Fur Chemie. 136 (2005) 1963–1970. doi:10.1007/s00706-005-0380-1.

[140] I. Cohen, A. Ha, X. Zhao, M. Lee, T. Fischer, M.J. Strouse, D. Kivelson, A Low-Temperature Amorphous Phase in a Fragile Glass-Forming Substance, J. Phys. Chem. 100 (1996) 8518–8526. doi:10.1021/jp953785h.

[141] R. Kurita, H. Tanaka, Critical-Like Phenomena Associated with Liquid-Liquid Transition in a Molecular Liquid, Sci. Reports. 306 (2004) 845–849.

[142] W. Xu, M.T. Sandor, Y. Yu, H.-B. Ke, H.-P. Zhang, M.-Z. Li, W.H. Wang, L. Liu, Y. Wu, Evidence of liquid-liquid transition in glass-forming $La_{50}Al_{35}Ni_{15}$ melt above liquidus temperature., Nat. Commun. 6 (2015) 7696. doi:10.1038/ncomms8696.

[143] B.A. Sun, M.X. Pan, D.Q. Zhao, W.H. Wang, X.K. Xi, M.T. Sandor, Y. Wu, Aluminum-rich bulk metallic glasses, Scr. Mater. 59 (2008) 1159–1162. doi:10.1016/j.scriptamat.2008.08.003.

[144] H.W. Kui, A.L. Greer, D. Turnbull, Formation of bulk metallic glass by fluxing, Appl. Phys. Lett. 45 (1984) 615–616. doi:10.1063/1.95330.

[145] R. Willnecker, K. Wittmann, G.P. Görler, Undercooling investigations and heat capacity measurements on Pd-Ni-P melts, J. Non. Cryst. Solids. 156–158 (1993) 450–454. doi:10.1016/0022-3093(93)90217-L.

[146] Y. He, R.B. Schwarz, J.I. Archuleta, Bulk glass formation in the Pd-Ni-P system, Appl. Phys. Lett. 69 (1996) 1861–1863. doi:10.1063/1.117458.

[147] H.S. Chen, Glass temperature, formation and stability of Fe, Co, Ni, Pd and Pt based glasses, Mater. Sci. Eng. 23 (1976) 151–154. doi:10.1016/0025-5416(76)90185-3.

[148] A.R. Yavari, S. Hamar-Thibault, H.R. Sinning, On the microstructure of amorphous $Pd_{46}Ni_{36}P_{18}$, Scr. Metall. 22 (1988) 1231–1234.

[149] A.R. Yavari, K. Osamura, H. Okuda, Y. Amenia, Small-angle x-ray scattering study of phase separation in amorphous alloys during heating with use of synchrotron radiation, Phys. Rev. B. 37 (1988).

[150] S. V. Madge, H. Rösner, G. Wilde, Transformations in supercooled Pd40.5Ni40.5P19, Scr. Mater. 53 (2005) 1147–1151. doi:10.1016/j.scriptamat.2005.07.020.

[151] S. Lan, Y. Ren, X.Y. Wei, B. Wang, E.P. Gilbert, T. Shibayama, S. Watanabe, M. Ohnuma, X.-L. Wang, Hidden amorphous phase and reentrant supercooled liquid in Pd-Ni-P metallic glasses, Nat. Commun. 8 (2017) 14679. doi:10.1038/ncomms14679.

[152] H.S. Chen, D. Turnbull, Thermal evidence of a glass transition in gold-silicon-germanium alloy, Appl. Phys. Lett. 10 (1967) 284–286. doi:10.1063/1.1754813.

[153] H.S. Chen, D. Turnbull, Evidence of a Glass–Liquid Transition in a Gold–Germanium–Silicon Alloy, J. Chem. Phys. 48 (1968) 2560–2571. doi:10.1063/1.1669483.

[154] A.J. Drehman, A.L. Greer, D. Turnbull, Bulk formation of a metallic glass: $Pd_{40}Ni_{40}P_{20}$, Appl. Phys. Lett. 41 (1982) 716–717. doi:10.1063/1.93645.

[155] G. Wilde, G.P. Görler, R. Willnecker, G. Dietz, Thermodynamic properties of $Pd_{40}Ni_{40}P_{20}$ in the glassy, liquid, and crystalline states, Appl. Phys. Lett. 65 (1994) 397–399. doi:10.1063/1.112313.

[156] N. Nishiyama, A. Inoue, Glass-Forming Ability of Bulk $Pd_{40}Ni_{10}Cu_{30}P_{20}$

Alloy, Mater. Trans. JIM. 37 (1996) 1531–1539. doi:10.2320/matertrans1989.37.1531.

[157] J. Schroers, W.L. Johnson, Highly processable bulk metallic glass-forming alloys in the Pt-Co-Ni-Cu-P system, Appl. Phys. Lett. 84 (2004) 3666–3668. doi:10.1063/1.1738945.

[158] T. Zhang, A. Inoue, T. Masumoto, Amorphous Zr-Al-TM (TM=Co, Ni, Cu) alloys with significant supercooled liquid region of over 100 K, Mater. Trans. JIM. 32 (1991) 1005–1010. doi:10.2320/matertrans1989.32.1005.

[159] A. Peker, W.L. Johnson, A highly processable metallic glass: $Zr_{41.2}Ti_{13.8}Cu_{12.5}Ni_{10.0}Be_{22.5}$, Appl. Phys. Lett. 63 (1993) 2342–2344. doi:10.1063/1.110520.

[160] G.L. Fiore, I. Ichim, L. Battezzati, Thermal analysis, fragility and viscosity of Au-based metallic glasses, J. Non. Cryst. Solids. 356 (2010) 2218–2222. doi:10.1016/j.jnoncrysol.2010.08.032.

[161] O. Gross, M. Eisenbart, L.Y. Schmitt, N. Neuber, L. Ciftci, U.E. Klotz, R. Busch, I. Gallino, Development of novel 18-karat, premium-white gold bulk metallic glasses with improved tarnishing resistance, Mater. Des. 140 (2018) 495–504. doi:10.1016/j.matdes.2017.12.007.

[162] G. Fiore, P. Rizzi, L. Battezzati, Phase constitution and glass formation in an Au-based alloy, J. Alloys Compd. 509 (2011) S166–S169. doi:10.1016/j.jallcom.2011.01.087.

[163] S. Mozgovoy, J. Heinrich, U.E. Klotz, R. Busch, Investigation of mechanical, corrosion and optical properties of an 18 carat Au-Cu-Si-Ag-Pd bulk metallic glass, Intermetallics. 18 (2010) 2289–2291. doi:10.1016/j.intermet.2010.07.021.

[164] M. Eisenbart, U.E. Klotz, R. Busch, I. Gallino, On the abnormal room temperature tarnishing of an 18 karat gold bulk metallic glass alloy, J. Alloys Compd. 615 (2014) S118–S122. doi:10.1016/j.jallcom.2013.11.167.

[165] M. Eisenbart, U.E. Klotz, R. Busch, I. Gallino, A colourimetric and

microstructural study of the tarnishing of gold-based bulk metallic glasses, Corros. Sci. 85 (2014) 258–269. doi:10.1016/j.corsci.2014.04.024.

[166] M. Eisenbart, On the Processing and the Tarnishing Mechanism of Gold-based Bulk Metallic Glasses, Universität des Saarlandes, 2016.

[167] N. Neuber, Alloy Development and Thermophysical Characterization of Amorphous 18kt White Gold Bulk Metallic Glasses with Improved Tarnishing Resistance, Universität des Saarlandes, 2017.

[168] Z. Evenson, S.E. Naleway, S. Wei, O. Gross, J.J. Kruzic, I. Gallino, W. Possart, M. Stommel, R. Busch, β relaxation and low-temperature aging in a Au-based bulk metallic glass: From elastic properties to atomic-scale structure, Phys. Rev. B. 89 (2014) 174204. doi:10.1103/PhysRevB.89.174204.

[169] Z. Evenson, T. Koschine, S. Wei, O. Gross, J. Bednarcik, I. Gallino, J.J. Kruzic, K. Rätzke, F. Faupel, R. Busch, The effect of low-temperature structural relaxation on free volume and chemical short-range ordering in a Au49Cu26.9Si16.3Ag5.5Pd2.3 bulk metallic glass, Scr. Mater. 103 (2015) 14–17. doi:10.1016/j.scriptamat.2015.02.026.

[170] D. V. Louzguine-Luzgin, I. Seki, S. V. Ketov, L. V. Louzguina-Luzgina, V.I. Polkin, N. Chen, H.-J. Fecht, A.N. Vasiliev, H. Kawaji, Glass-transition process in an Au-based metallic glass, J. Non. Cryst. Solids. 419 (2015) 12–15. doi:10.1016/j.jnoncrysol.2015.03.018.

[171] J.Q. Wang, Y. Shen, J.H. Perepezko, M.D. Ediger, Increasing the kinetic stability of bulk metallic glasses, Acta Mater. 104 (2016) 25–32. doi:10.1016/j.actamat.2015.11.048.

[172] A. Balerna, S. Mobilio, Introduction to Synchrotron Radiation, in: Synchrotron Radiat. Basics, Methods Appl., Mobilio, Settimio Boscherini, Federico Meneghini, Carlo, 2015: pp. 1–799. doi:10.1007/978-3-642-55315-8.

[173] P. Elleaume, A. Ropert, The ultimate hard X-ray storage-ring-based light source, Nucl. Instruments Methods Phys. Res. Sect. A Accel. Spectrometers,

Detect. Assoc. Equip. 500 (2003) 18–24. doi:10.1016/S0168-9002(03)00737-X.

[174] L. Cipelletti, S. Manley, R.C. Ball, D.A. Weitz, Universal Aging Features in the Restructuring of Fractal Colloidal Gels, Phys. Rev. Lett. 84 (2000) 2275–2278. doi:10.1103/physrevlett.84.2275.

[175] L. Cipelletti, L. Ramos, S. Manley, E. Pitard, D.A. Weitz, E.E. Pashkovski, M. Johansson, Universal non-diffusive slow dynamics in aging soft matter., Faraday Discuss. 123 (2003) 237–251. doi:10.1039/b204495a.

[176] J.-P. Bouchaud, E. Pitard, Anomalous dynamical light scattering in soft glassy gels, Eur. Phys. J. E. 236 (2001) 231–236.

[177] M. Sutton, S.G.J. Mochrie, T. Greytak, S.E. Nagler, L.E. Berman, G.A. Held, G.B. Stephenson, Observation of speckle by diffraction with coherent X-rays, Lett. to Nat. 352 (1991) 608–610. doi:10.1038/352608a0.

[178] M. Leitner, B. Sepiol, L.-M. Stadler, B. Pfau, G. Vogl, Atomic diffusion studied with coherent X-rays, Nat. Mater. 8 (2009) 717–720. doi:10.1038/nmat2506.

[179] B. Ruta, Y. Chushkin, L. Cipelletti, E. Pineda, P. Bruna, V.M. Giordano, Supplementary Information: Atomic-Scale Relaxation Dynamics and Aging in a Metallic Glass Probed by X-Ray Photon Correlation Spectroscopy, Phys. Rev. Lett. 109 (2012) 1–5.

[180] B. Ruta, G. Baldi, Y. Chushkin, B. Rufflé, L. Cristofolini, A. Fontana, M. Zanatta, F. Nazzani, Revealing the fast atomic motion of network glasses., Nat. Commun. 5 (2014) 3939. doi:10.1038/ncomms4939.

[181] V.M. Giordano, B. Ruta, Unveiling the structural arrangements responsible for the atomic dynamics in metallic glasses during physical aging, Nat. Commun. 7 (2015) 10344. doi:10.1038/ncomms10344.

[182] O. Bikondoa, On the use of two-time correlation functions for X-ray photon correlation spectroscopy data analysis, J. Appl. Crystallogr. 50 (2017) 357–368. doi:10.1107/S1600576717000577.

[183] E. Bartsch, V. Frenz, J. Baschnagel, W. Schärtl, H. Sillescu, The glass transition dynamics of polymer micronetwork colloids. A mode coupling analysis, J. Chem. Phys. 106 (1997) 3743–3756. doi:doi:10.1063/1.473464.

[184] B.J. Berne, R. Pecora, Dynamic Light Scattering with Applications to Chemistry, Biology, and Physics, Mineola, NY, 2000.

[185] F. van der Veen, F. Pfeiffer, Coherent x-ray scattering, J. Phys. Condens. Matter. 16 (2004) 5003–5030. doi:10.1088/0953-8984/16/28/020.

[186] B. Ruta, Science and Students Day 2014 ESRF, Atomic motion in disordered systems studied with coherent x-rays, Grenoble, 2014.

[187] A. Madsen, R.L. Leheny, H. Guo, M. Sprung, O. Czakkel, Beyond simple exponential correlation functions and equilibrium dynamics in x-ray photon correlation spectroscopy, New J. Phys. 12 (2010) 055001. doi:10.1088/1367-2630/12/5/055001.

[188] M. Sutton, A review of X-ray intensity fluctuation spectroscopy, C.R. Phys. 9 (2008) 657–667. doi:10.1007/1-4020-3337-0_9.

[189] G. Gruebel, D.L. Abernathy, Diffraction and Correlation Spectroscopy with Coherent X-rays, SPIE Proc. 3154 (1997) 103–109. doi:10.1117/12.279386.

[190] O. Konovalov, Y. Chushkin, F. Zontone, The Soft Interfaces and Coherent Scattering Beamline : A multi station beam-line for scattering from Liquid Surfaces and Soft Interfaces, for scattering with Coherent X-rays for Photon Correlation Spectroscopy applications and Diffraction Imaging, Grenoble, 2013.

[191] S. Kirsch, V. Frenz, W. Schärtl, E. Bartsch, H. Sillescu, Multispeckle autocorrelation spectroscopy and its application to the investigation of ultraslow dynamical processes, J. Chem. Phys. 104 (1996) 1758. doi:10.1063/1.470761.

[192] L. Cipelletti, D.A. Weitz, Ultralow-angle dynamic light scattering with a charge coupled device camera based multispeckle, multitau correlator, Rev. Sci. Inst. 70 (1999) 3214–3221. doi:10.1063/1.1149894.

[193] H. Conrad, F. Lehmkühler, B. Fischer, F. Westermeier, M.A. Schroer, Y. Chushkin, C. Gutt, M. Sprung, G. Grübel, Correlated heterogeneous dynamics in glass-forming polymers, Phys. Rev. E - Stat. Nonlinear, Soft Matter Phys. 91 (2015) 1–6. doi:10.1103/PhysRevE.91.042309.

[194] F. Perakis, K. Amann-Winkel, F. Lehmkühler, M. Sprung, D. Mariedahl, J.A. Sellberg, H. Pathak, A. Späh, F. Cavalca, D. Schlesinger, A. Ricci, A. Jain, B. Massani, F. Aubree, C.J. Benmore, T. Loerting, G. Grübel, L.G.M. Pettersson, A. Nilsson, Diffusive dynamics during the high-to-low density transition in amorphous ice, Proc. Natl. Acad. Sci. 114 (2017) 8193–8198. doi:10.1073/pnas.1705303114.

[195] V. Trappe, E. Pitard, L. Ramos, A. Robert, H. Bissig, L. Cipelletti, Investigation of q -dependent dynamical heterogeneity in a colloidal gel by x-ray photon correlation spectroscopy, Phys. Rev. E - Stat. Nonlinear, Soft Matter Phys. 76 (2007) 1–7. doi:10.1103/PhysRevE.76.051404.

[196] D. Orsi, B. Ruta, Y. Chushkin, A. Pucci, G. Ruggeri, G. Baldi, T. Rimoldi, L. Cristofolini, Controlling the dynamics of a bidimensional gel above and below its percolation transition, Phys. Rev. E - Stat. Nonlinear, Soft Matter Phys. 89 (2014) 1–11. doi:10.1103/PhysRevE.89.042308.

[197] E. Wandersman, Y. Chushkin, E. Dubois, V. Dupuis, A. Robert, R. Perzynski, Field induced anisotropic cooperativity in a magnetic colloidal glass, Soft Matter. 11 (2015) 7165–7170. doi:10.1039/C5SM01315A.

[198] S. Hechler, B. Ruta, M. Stolpe, D. Orsi, L. Cristofolini, Z. Evenson, R. Busch, I. Gallino, Influence of the structure and dynamical heterogeneities on the relaxation dynamics in an ultra-viscous glass-former, Phys. Rev. Lett. (n.d.).

[199] P.G. De Gennes, Liquid dynamics and inelastic scattering of neutrons, Physica. (1959) 825–839.

[200] B.N. Brockhouse, N.K. Pope, Time-dependent pair correlations in liquid lead, Phys. Rev. Lett. 3 (1959) 259–262. doi:10.1103/PhysRevLett.3.259.

[201] F. Demmel, D. Szubrin, W.-C. Pilgrim, C. Morkel, Diffusion in liquid

aluminium probed by quasielastic neutron scattering, Phys. Rev. B - Condens. Matter Mater. Phys. 84 (2011) 2–5. doi:10.1103/PhysRevB.84.014307.

[202] S.M. Bhattacharyya, B. Bagchi, P.G. Wolynes, Subquadratic wavenumber dependence of the structural relaxation of supercooled liquid in the crossover regime, J. Chem. Phys. 132 (2010). doi:10.1063/1.3330911.

[203] A. Rinaldi, F. Sciortino, P. Tartaglia, Dynamics in a supercooled molecular liquid: Theory and simulations, Phys. Rev. E - Stat. Nonlinear, Soft Matter Phys. 63 (2001) 1–10. doi:10.1103/PhysRevE.63.061210.

[204] F. Demmel, A. Diepold, H. Aschauer, C. Morkel, Temperature dependence of the de Gennes narrowing in liquid rubidium, Phys. Rev. B. 73 (2006) 1–5. doi:10.1103/PhysRevB.73.104207.

[205] F. Demmel, P. Fouquet, W. Häussler, C. Morkel, De Gennes slowing in a liquid metal revisited: A neutron spin-echo study, Phys. Rev. E - Stat. Nonlinear, Soft Matter Phys. 73 (2006) 73–75. doi:10.1103/PhysRevE.73.032202.

[206] D. Bertolini, F. Demmel, A. Tani, Temperature dependence of de Gennes narrowing and transport properties of liquid rubidium: Experimental and simulation results, Phys. Rev. B - Condens. Matter Mater. Phys. 76 (2007) 1–9. doi:10.1103/PhysRevB.76.094204.

[207] A. Tölle, J. Wuttke, H. Schober, Wavenumber dependence of structural relaxation in a molecular liquid, Eur. Phys. …. 236 (1998) 231–236. http://link.springer.com/article/10.1007/s100510050439.

[208] E. Bartsch, F. Fujara, J.F. Legrand, W. Petry, H. Sillescu, J. Wuttke, Dynamics in viscous orthoterphenyl: Results from coherent neutron scattering, Phys. Rev. E. 52 (1995) 738–745. doi:10.1103/PhysRevE.52.738.

[209] J. Wuttke, I. Chang, O. Randl, F. Fujara, W. Petry, Tagged-particle motion in viscous glycerol: Diffusion-relaxation crossover, Phys. Rev. E. 54 (1996) 5364–5369. doi:10.1103/PhysRevE.54.5364.

[210] F. Mezei, W. Knaak, B. Farago, Neutron spin echo study of dynamic correlations near the liquid-glass transition, Phys. Rev. Lett. 58 (1987) 571–574. doi:10.1103/PhysRevLett.58.571.

[211] F. Mezei, Scaling behaviour of structural relaxation near the glass transition: a critical analysis, J. Non. Cryst. Solids. 131–133 (1991) 317–326. doi:10.1016/0022-3093(91)90323-X.

[212] V.N. Novikov, K.S. Schweizer, A.P. Sokolov, Coherent neutron scattering and collective dynamics on mesoscale, J. Chem. Phys. 138 (2013). doi:10.1063/1.4802771.

[213] D. Richter, B. Frick, B. Farago, Neutron-spin-echo investigation on the dynamics of polybutadiene near the glass transition, Phys. Rev. Lett. 61 (1988) 2465–2468. doi:10.1103/PhysRevLett.61.2465.

[214] M. Tyagi, A. Arbe, F. Alvarez, J. Colmenero, M.A. González, Short-range order and collective dynamics of poly(vinyl acetate): A combined study by neutron scattering and molecular dynamics simulations, J. Chem. Phys. 129 (2008). doi:10.1063/1.3028210.

[215] R. Pérez-Aparicio, A. Arbe, F. Alvarez, J. Colmenero, L. Willner, Quasielastic neutron scattering and molecular dynamics simulation study on the structure factor of poly(ethylene-alt-propylene), Macromolecules. 42 (2009) 8271–8285. doi:10.1021/ma9016407.

[216] T. Egami, S.J.L. Billinge, UNDERNEATH THE BRAGG PEAKS Structural Analysis of Complex Materials, Pergamon Elsevier Ltd., New York, 2003.

[217] S. Pogatscher, P.J. Uggowitzer, J.F. Löffler, In-situ probing of metallic glass formation and crystallization upon heating and cooling via fast differential scanning calorimetry, Appl. Phys. Lett. 104 (2014). doi:10.1063/1.4884940.

[218] M. Frey, N. Neuber, Unpublished work, To Be Chosen. (2017).

[219] I. Gallino, D. Cangialosi, Z. Evenson, L. Schmitt, S. Hechler, M. Stolpe, B. Ruta, Hierarchical aging pathways and reversible fragile-to-strong transition

upon annealing of a metallic glass former, Acta Mater. 144 (2018) 400–410. doi:10.1016/j.actamat.2017.10.060.

[220] R. Busch, W.L. Johnson, The kinetic glass transition of the $Zr_{46.75}Ti_{8.25}Cu_{7.5}Ni_{10}Be_{27.5}$ bulk metallic glass former-supercooled liquids on a long time scale, Appl. Phys. Lett. 72 (1998) 2695–2697.

[221] I. Gallino, M.B. Shah, R. Busch, Enthalpy relaxation and its relation to the thermodynamics and crystallization of the $Zr_{58.50}Cu_{15.6}Ni_{12.8}Al_{10.3}Nb_{2.8}$ bulk metallic glass-forming alloy, Acta Mater. 55 (2007) 1367–1376. doi:10.1016/j.actamat.2006.09.040.

[222] C.T.C. Moynihan, A.A.J. Easteal, J. Wilder, J. Tucker, Dependence of the glass transition temperature on heating and cooling rate, J. Phys. Chem. 78 (1974) 2673–2677. doi:10.1021/j100619a008.

[223] C.T. Moynihan, A.J. Easteal, M.A. De Bolt, J. Tucker, Dependence of the Fictive Temperature of Glass on Cooling Rate, J. Am. Ceram. Soc. 59 (1976) 12–16. doi:10.1111/j.1151-2916.1976.tb09376.x.

[224] R. Böhmer, C.A. Angell, Correlations of the nonexponentiality and state dependence of mechanical relaxations with bond connectivity in Ge-As-Se supercooled liquids, Phys. Rev. B. 45 (1992) 10091–10094. doi:10.1103/PhysRevB.45.10091.

[225] R. Busch, E. Bakke, W.L. Johnson, Viscosity of the supercooled liquid and relaxation at the glass transition of the $Zr_{46.75}Ti_{8.25}Cu_{7.5}Ni_{10}Be_{27.5}$ bulk metallic glass forming alloy, Acta Mater. (1998) 1–8.

[226] H.E. Hagy, Experimental Evaluation of Beam-Bending Method of Determining Glass Viscosities in the Range 10(8) to 10(15) Poises.pdf, J. Am. Ceram. Soc. 46 (1963) 93–97.

[227] T.A. Waniuk, R. Busch, A. Masuhr, W.L. Johnson, Equilibrium viscosity of the $Zr_{41.2}Ti_{13.8}Cu_{12.5}Ni_{10}Be_{22.5}$ bulk metallic glass-forming liquid and viscous flow during relaxation, phase separation, and primary crystallization, Acta Mater. 46 (1998) 5229–5236. doi:10.1016/S1359-6454(98)00242-0.

[228] B. Ruta, Y. Chushkin, L. Cipelletti, E. Pineda, P. Bruna, V.M. Giordano, Atomic-Scale Relaxation Dynamics and Aging in a Metallic Glass Probed by X-Ray Photon Correlation Spectroscopy, Phys. Rev. Lett. 109 (2012) 165701. doi:10.1103/PhysRevLett.109.165701.

[229] T.G. Mezger, The rheology handbook: for users of rotational and oscillatory rheometers, 3rd ed., Vincentz Network GmbH & Co KG, 2011.

[230] O. Gross, B. Bochtler, S. Hechler, M. Stolpe, A. Kuball, S. Wei, J. Bednarcik, J.J. Kruzic, I. Gallino, R. Busch, Tuning-in the strong and fragile liquid structures through a structural liquid-liquid transition in an Au-based bulk metallic glassformer, To Be Chosen. (n.d.).

[231] I. Gallino, D. Cangialosi, Z. Evenson, L. Schmitt, S. Hechler, B. Ruta, Activation energy spectrum for relaxation and polyamorphism in an ultra-viscous metallic glass former, ArXiv. 1706 (2017) 03830.

[232] F. Faupel, W. Frank, M.P. Macht, H. Mehrer, V. Naundorf, K. Rätzke, H.R. Schober, S.K. Sharma, H. Teichler, Diffusion in metallic glasses and undercooled melts, Rev. Mod. Phys. 75 (2003) 237–280. doi:10.3139/146.018046.

[233] B. Ruta, V.M. Giordano, L. Erra, C. Liu, E. Pineda, Structural and dynamical properties of $Mg_{65}Cu_{25}Y_{10}$ metallic glasses studied by in situ high energy X-ray diffraction and time resolved X-ray photon correlation spectroscopy, J. Alloys Compd. 615 (2014) 45–50. doi:10.1016/j.jallcom.2013.12.162.

[234] S. Hechler, B. Ruta, M. Stolpe, E. Pineda, Z. Evenson, O. Gross, W. Hembree, Liquid-liquid transition revealed by quasi-static cooling of an ultra-viscous metallic liquid, ArXiv. 1704.06703 (2017) 1704.06703.

[235] B. Ruta, G. Baldi, G. Monaco, Y. Chushkin, Compressed correlation functions and fast aging dynamics in metallic glasses, J. Chem. Phys. 138 (2013) 054508. doi:10.1063/1.4790131.

[236] Z. Evenson, F. Yang, G.G. Simeoni, A. Meyer, Self-diffusion and microscopic dynamics in a gold-silicon liquid investigated with quasielastic

neutron scattering, Appl. Phys. Lett. 108 (2016). doi:10.1063/1.4944814.

[237] S. Szabó, Z. Evenson, Self-diffusion in liquid Al-Ge investigated with quasi-elastic neutron scattering, Appl. Phys. Lett. 110 (2017). doi:10.1063/1.4981804.

[238] F. Weysser, A.M. Puertas, M. Fuchs, T. Voigtmann, Structural relaxation of polydisperse hard spheres: Comparison of the mode-coupling theory to a Langevin dynamics simulation, Phys. Rev. E - Stat. Nonlinear, Soft Matter Phys. 82 (2010) 1–21. doi:10.1103/PhysRevE.82.011504.

[239] F. Sciortino, P. Gallo, P. Tartaglia, S.-H. Chen, Supercooled Water and the Kinetic Glass Transition, Phys. Rev. E. 54 (1996) 6331. papers2://publication/uuid/20D7438D-A4BA-4332-B1D1-131E7FBAF18B.

[240] J. Zhao, S.L. Simon, G.B. Mckenna, Using 20-million-year-old amber to test the super-Arrhenius behaviour of glass-forming systems, Nat. Commun. 4 (2013) 1783–1786. doi:10.1038/ncomms2809.

[241] E. Arianna, A. Pogna, C. Rodríguez-Tinoco, G. Cerullo, C. Ferrante, J. Rodríguez-Viejo, Probing equilibrium glass flow up to exapoise viscosities, PNAS. 112 (2015) 2331–2336. doi:10.1073/pnas.1423435112.

[242] T. Hecksher, A.I. Nielsen, N.B. Olsen, J.C. Dyre, Little evidence for dynamic divergences in ultraviscous molecular liquids, Nat. Phys. 4 (2008) 737–741. doi:10.1038/nphys1033.

[243] H. Winick, S. Linear, Fourth generation light sources, Conf.Proc. C970512 (1997) 37–41.

[244] A. Madsen, A. Fluerasu, B. Ruta, Structural Dynamics of Materials Probed by X-Ray Photon Correlation Spectroscopy, in: Synchrotron Light Sources Free. Lasers, Springer International Publishing, Cham, 2015: pp. 1–21. doi:10.1007/978-3-319-04507-8_29-1.

[245] A. Kuball, O. Gross, B. Bochtler, R. Busch, Sulfur-bearing metallic glasses : A new family of bulk glass-forming alloys, Scr. Mater. 146 (2018) 73–76. doi:10.1016/j.scriptamat.2017.11.011.

9 Copyright permissions

Table 9-1: Copyright permissions for reused published material.

Figure	License number
2-2	4366630849187
2-3	4366640392648
2-4	4366640561629
2-13	4366640079736
2-14	4366631112533
2-17	4366640698024
2-18	RNP/18/JUN/005143
2-19	Generally permitted
2-20	4366640881660
3-1	4366631255924
3-2	RNP/18/JUN/005144
3-3	4366631355494
3-4	4366631486064